Forschungszentrum Karlsruhe
Technik und Umwelt

Wissenschaftliche Berichte
FZKA 6370

PREMIX Tests PM12, PM13, and PM14

Documentation and Evaluation of Experimental Data

A. Kaiser, W. Schütz, H. Will

Institut für Reaktorsicherheit
Projekt Nukleare Sicherheitsforschung

November 1999

Forschungszentrum Karlsruhe

Technik und Umwelt

Wissenschaftliche Berichte

FZKA 6370

PREMIX Tests PM12, PM13, and PM14
Documentation and Evaluation of Experimental Data

A. Kaiser, W. Schütz, H. Will

Institut für Reaktorsicherheit

Projekt Nukleare Sicherheitsforschung

Forschungszentrum Karlsruhe GmbH, Karlsruhe
1999

This document has been prepared
in the frame of the
4th EU Framework Programme
on Fission Reactor Safety 1996-99,

MFCI-Project
Contract FI4S-CT96-0037
Activity 2.1, PREMIX tests P2

EU number of present document:
INV-MFCI(99)-D050

Als Manuskript gedruckt

Forschungszentrum Karlsruhe GmbH
Postfach 3640, 76021 Karlsruhe

Mitglied der Hermann von Helmholtz-Gemeinschaft
Deutscher Forschungszentren (HGF)

ISSN 0947-8620

Abstract

During melt-down of the core of a light-water reactor, as a consequence of a severe accident, hot melt may come into contact with coolant in the lower plenum. The amount of masses involved and the intensity of the interaction determine the extent of a possible steam explosion.

Such events are being investigated, among other laboratories, at the Forschungszentrum Karlsruhe in so-called PREMIX experiments. Using alumina melt instead of corium, the melt is released from above into a water pool.

To prove reproducibility of the PREMIX experiments, three tests have been performed with starting conditions identically specified. Additionally, the conditions of the tests were chosen in order to facilitate comparison of the results with those of the FARO/FAT tests performed at JRC Ispra with molten corium and water.

The general course of the three PREMIX tests turned out to be very similar. Fragmentation of the melt, premixing, and steam production occurred in such a way that the bulk of water was prevented from close contact with the melt. No indication of conditions was found under which a steam explosion was to be expected.

The most relevant data, maximum pressure and steam generation rates, differ by less than 10 %. Peculiar differences, found in the times after the first melt/water contact when a significant pressure rise started, can generally be attributed to uncertainties in controlling the melt supply. Summarizing, one can state that the results are conclusive, i.e., we conclude that the PREMIX experiments are reproducible.

This report gives a documentation of the results which provide a data base that can be used for the validation of multiphase computer programmes being presently developped.

Zusammenfassung

PREMIX-Versuche PM12, PM13 und PM14 - Dokumentation und Auswertung der Ergebnisse

Beim Niederschmelzen des Reaktorkerns, denkbar als Folge eines schweren Störfalls in einem Leichtwasserreaktor, kann heiße Schmelze mit Kühlmittel im unteren Plenum in Kontakt kommen. Der Umfang der beteiligten Massen und die Intensität der Wechselwirkung bestimmen das Ausmaß einer eventuell auftretenden Dampfexplosion.

Derartige Vorgänge werden in Forschungsstätten verschiedener Länder untersucht. Im Forschungszentrum Karlsruhe läßt man in sogenannten PREMIX-Experimenten heiße Schmelze von oben in einen mit Wasser gefüllten Behälter fließen. Anstelle von Corium wird Aluminiumoxid-Schmelze eingesetzt.

Zur Überprüfung der Reproduzierbarkeit der Versuchsergebnisse wurden drei Experimente unter gleichen anfänglichen Versuchsbedingungen durchgeführt. Darüber hinaus wurden die Bedingungen der PREMIX-Versuche so gewählt, daß der Vergleich mit Ergebnissen der FARO/FAT-Versuche erleichtert wird, die mit geschmolzenem Corium und Wasser am JRC, Ispra, durchgeführt werden.

Der generelle Ablauf der drei Versuche war sehr ähnlich. Der Fragmentierungsprozeß, die Vorvermischung und die Dampfbildung verliefen in einer Weise, daß die große Masse des Wassers von einem engen Kontakt mit der Schmelze abgehalten wurde. Bedingungen, die Voraussetzung für das Auftreten einer Dampfexplosion sind, wurden nicht beobachtet.

Die wichtigsten Meßdaten, wie maximaler Druck und Dampfproduktionsrate, unterschieden sich um weniger als 10%. Ein, wenn auch geringer, Unterschied besteht in der Zeitspanne vom ersten Schmelze/Wasser-Kontakt bis zum Beginn eines signifikanten Druckanstiegs im Versuchsbehälter. Die Unterschiede können Unsicherheiten im zeitlichen Ablauf der Schmelzefreisetzung zugewiesen werden. Insgesamt konnte gezeigt werden, daß die Ergebnisse schlüssig sind, und wir schließen daraus, daß die PREMIX-Ergebnisse reproduzierbar sind

Der Bericht dokumentiert die Ergebnisse der drei Versuche. Die gewonnenen Daten eignen sich als Datenbasis für die Validierung von in der Entwicklung befindlichen Computerprogramme.

CONTENTS

1 Introduction 1
2 Experimental set-up and test procedure 2
2.1 Test facility 2
2.2 Melt generator 3
2.3 Instrumentation 3
2.4 Experimental conditions and test procedure 6
2.4.1 Test parameters 6
2.4.2 Test procedure 6
2.5 Data acquisition 7
2.6 Data evaluation 7
2.6.1 Pressure measurements 7
2.6.2 Melt release 8
2.6.3 Level measurement 8
2.6.4 Void and temperature measurements 9
3 Results of PM13 20
3.1 General course of the experiment 20
3.2 Pressure, steam flow, and level measurements 21
3.3 Development of the interaction zone in the water 24
3.3.1 Progression of the steam/liquid interface 24
3.3.2 Volumes and average volume fractions resulting from the interaction 25
3.3.3 Local distributions of steam and water in the water pool 27
3.3.4 Jet fragmentation 27
3.4 Progression of the steam-water mixture into the annular gas space 27
3.5 Post test investigation 28
3.5.1 Water mass balance 28
3.5.2 Melt balance and sieve analysis 29
3.5.3 Chemical analysis 29
4 Results of PM14 47
4.1 General course of the experiment 47
4.2 Pressure, steam flow, and level measurements 47
4.3 Development of the interaction zone in the water 49
4.3.1 Progression of the steam/liquid interface 49
4.3.2 Volumes and average volume fractions resulting from the interaction 50
4.3.3 Local distributions of steam and water in the water pool 51
4.3.4 Jet fragmentation 51
4.4 Progression of the steam-water mixture into the annular gas space 51
4.5 Post test investigation 52
4.5.1 Water mass balance 52
4.5.2 Melt balance and sieve analysis 52
4.5.3 Chemical analysis 53
4.5.4 Gas analysis 53
5 RESULTS OF PM 12 75
5.1 General course of the experiment 75
5.2 Pressure and level measurements 75
5.3 Development of the interaction zone in the water 77
5.3.1 Progression of the steam/liquid interface 77
5.3.2 Volumes and average volume fractions resulting from the interaction 78
5.3.3 Local distributions of steam and water in the water pool 78

5.3.4 Jet fragmentation 78
5.4 Progression of the steam-water mixture into the annular gas space 79
5.5 Post test investigation 80
5.5.1 Water mass balance 80
5.5.2 Gas analysis 80
5.5.3 Melt mass balance and sieve analysis 80
5.5.4 Chemical analysis 81
6 Comparison of the results 97
6.1 Pressures 97
6.2 Steam flow 97
6.3 Rise of water level 98
6.4 Development of the interaction zone 98
6.5 Sieve analysis 98
7 Summary and conclusions 105
8 Literature 106

Appendix A A-1
..... A-2

Appendix B B-1
..... B-2
..... B-3

List of the figures

Fig. 2.1:	Test facility used for PM12, PM13 and PM14.	11
Fig. 2.2:	Schematic of the melt generator. Note that the axial coordinate of the melt generator is different from that of the test vessel (Fig. 2.1)	12
Fig. 2.3:	Locations of the pressure transducers mounted in the annular gas space and in venting line No 3.	13
Fig. 2.4:	Construction of a void lance. The major parts are (upper picture from left to right): a body carrying the sensors, threaded joint which is in the realm of the vessel wall, carrier tube, and connection box. The lower picture shows four of the eight sensors and the thermocouple at the free end.	14
Fig. 2.5a:	Void signals obtained in PM14 from the V08 measuring probes located 270 mm below the initial water level. The radial coordinate increases from top to bottom.	15
Fig. 2.5b:	Void signals obtained in PM14 at various heights close to the vessel axis.	16
Fig. 2.5c:	Signals obtained in PM14 from the V05 lance located in the annular gas space 250 mm above the initial water level.	17
Fig. 2.6:	Processing of void signal data obtained in the water pool (a) and in the gas (b). Smoothing was performed by integration using a window with of 10 ms.	18
Fig. 2.7:	Example: Distribution of steam and water in the pool at const. time. Parameter is the volume fraction; white area ≈ 100 % steam; dark = water.	19
Fig. 3.1:	Development of the interaction zone in PM13 shown by selected pictures of the video film.	31
Fig. 3.2:	Pressure data obtained inside and outside of the melt generator.	32
Fig. 3.3:	Melt release calculated on basis of the pressure difference. The calculation started at the time estimated for steel membrane break (-0.1 s). The length in crucible is related to the lower end of the nozzle.	32
Fig. 3.4:	Pressure data obtained from gauges located in the water pool.	33
Fig. 3.5:	Comparison of the PK15 absolute pressure data obtained in the water at –815 mm height with the PK10 dynamic pressure data.	33
Fig. 3.6:	Pressure data obtained from transducers located in the gas space (PK01-PK04) and at a distance of 25 mm below the initial water level (PK07).	34
Fig. 3.7:	Steam flow rates and the time-integrated steam volume.	34
Fig. 3.8:	Data of the four level measurements.	35

Fig. 3.9a:	Void signals from the V06 lange (96 mm above init. water level).	36
Fig. 3.9b:	Void signals from the V07 lange (67 mm below init. water level).	37
Fig. 3.10:	Temperatures measured in the water pool (T07-T16). The T06 data also shown (a) are obtained a short distance above the initial water level.	38
Fig. 3.11:	Progression of the interaction zone into the water with the time as a parameter.	39
Fig. 3.12:	Progression of the interaction zone in the centre of the pool. The speed is derived from the film data.	39
Fig. 3.13:	Volumes resulting from the interaction (MIAV-multiphase inter action volume; Exit = volume of the evaporated part of water; volume due to level increase) and partial volumes of the interaction zone (steam, liquid, and melt) are shown on top, average volume fractions of the three components inside the interaction zone at the bottom.	40
Fig. 3.14:	Distribution of steam and water in the water pool in PM13 at various times (white area = 100 % steam; dark = 100 % water). Distance between fraction lines: 0.125.	41
Fig. 3.15:	Temperatures measured in the freeboard volume (T06) and in the annular gas compartment.	42
Fig. 3.16:	Void signals obtained from the freeboard volume (V06) and the annular gas compartment at various heights. Smoothed signals (cf. Fig. 2.6) have been chosen to get a better time resolution. The measuring tips were close to the test vessel wall.	42
Fig. 3.17:	Penetration of water into the annular compartment versus time compared with rise of the water. The steam flow rate is also shown.	43
Fig. 3.18:	Progression of the water drop front into the annular gas compartment shown with the time as a parameter.	43
Fig. 3.19a:	PM13. Distribution of steam (gas) and water across the annular gas compartment between 207 and 407 mm height evaluated from void data. The times between the pictures is 0.01 s.	44
Fig. 3.19b:	PM13. Distribution of steam (gas) and water across the annular gas compartment between 207 and 407 mm height. (The time step between the pictures has been increased in the lowermost line).	45
Fig. 3.20:	Post-test particle size distribution of the melt fragments.	46
Fig. 4.1:	Development of the interaction zone in PM14 shown by selected pictures of the video film.	55
Fig. 4.2:	Film pictures taken by a high-speed camera show the initial time in PM14.	56
Fig. 4.3:	Pressures obtained from inside and outside of the melt generator.	57

Fig. 4.4: Melt release calculated on basis of the pressure difference. The calculation started at the time estimated for steel membrane break. The length in crucible is related to the lower end of the nozzle. 58

Fig. 4.5: Pressure data obtained from the water pool. 59

Fig. 4.6: Pressure data obtained from the freeboard volume and from the annular compartment. 60

Fig. 4.7: Comparison of pressure data obtained in the water (PK08) and in the annular gas space (PK02). 61

Fig. 4.8: Steam flow rates and steam volume integrated over time. 61

Fig. 4.9: Loss coefficients across several sub-sections of the steam flow path including venting pipe No 3. Locations of the transducers are given in the upper part. Reference pressure for the ζ_{P1} and ζ_{P2} coefficients was the ambient pressure. 62

Fig. 4.10: ζ_{PK01} loss coefficient calculated on basis of the PK01 pressure data and the steam flow rate ($P_{envir.}$ = environment pressure; F03 data faults around 1.8 s have been eliminated). 63

Fig. 4.11: Average of the four water level measurements. 63

Fig. 4.12a: Void signals from the V07 lance (67 mm below the init. water level). 64

Fig. 4.12b: Void signals from the V06 lance (97 mm above the init. water level). 65

Fig. 4.13: Temperatures measured in the water pool (T07 – T16). The T06 data also shown (a) are obtained a short distance above the initial water level. 66

Fig. 4.14: Progression of the interaction zone into the water with the time as a parameter. 67

Fig. 4.15: Progression of the interaction zone in the centre of the pool. the speed is derived from film data. 67

Fig. 4.16: Volumes resulting from the interaction (MIAV = multiphase interaction volume; Exit = volume of the evaporated part of water; volume due to level increase) and partial volumes of the interaction zone (steam; liquid, and melt) are shown on top, average volume fractions of the components inside the interaction zone below. 68

Fig. 4.17: Distribution of steam and water in the water pool in PM14 at various times (white area = 100 % steam; dark = 100 % water). Distance between fraction lines: ≈ 0.125. 69

Fig. 4.18: Temperatures measured in the freeboard volume (T06) and in the annular gas compartment (T02 – T05). 70

Fig. 4.19: Void signals obtained from the freeboard volume (V06) and the annular gas compartment at various heights. Smoothed signals (cf. Fig. 2.6) have been chosen to get a better time resolution. The measuring tips were close to the test vessel wall. 70

Fig. 4.20: Penetration of water into the annular gas compartment versus time compared with the water level rise. The steam flow rate is also shown. 71

Fig. 4.21:	Progression of the water front (drops and slugs) into the annular gas space shown with the time as a parameter.	71
Fig. 4.22:	PM14. Distribution of steam (gas) and water across the annular gas compartment between 207 and 407 mm height gained from void data. Time between the pictures is 0.01 s, in some cases 0.02 s. Void fraction lines: 1 = 100 % steam; 0 = 100 % water.	72
Fig. 4.22:	PM14 (continued). Time between the pictures is 0.01 s; it is larger in the lowermost row. Void fraction lines: 1 = 100 % steam; 0 = 100 % water.	73
Fig. 4.23:	Post-test particle size distribution of the melt fragments.	74
Fig. 5.1:	Development of the interaction zone in PM12 shown by pictures of the video film.	83
Fig. 5.2:	Pressures inside and outside of the melt generator.	84
Fig. 5.3:	Melt flow rate calculated on basis of the pressure difference.	84
Fig. 5.4:	Pressure data obtained from transducers located in the water pool.	85
Fig. 5.5:	Pressure data obtained from transducers located in the gas compartment (PK01 – PK04) and a short distance (45 mm) below the initial water level (PK07), respectively.	85
Fig. 5.6:	Water level measurement.	86
Fig. 5.7a:	Void signals of the V06 measuring lance. Smoothed signals (cf. Fig. 2.6) have been chosen to obtain a better time resolution. The measuring tips of the void probes were located 77 mm above the water surface.	87
Fig. 5.7b:	Full signals of the V07 measuring lance. The measuring tips of the void probes were located 87 mm below the water surface.	88
Fig. 5.8:	Temperatures measured in the water pool (T07 – T16). T06 signal was measured 77 mm above the initial water level.	89
Fig. 5.9:	Progression of the interaction zone into the water with the time as a parameter.	90
Fig. 5.10:	Progression of the interaction zone in the centre of the pool. The speed is derived from film data.	90
Fig. 5.11:	Volumes resulting from the interaction (MIAV = multiphase interaction volume; Exit = volume of the evaporated part of water; volume due to level increase) and partial volumes of the interaction zone (steam, liquid, and melt) are shown on top, average volume fractions of the three components inside the interaction zone at the bottom.	91
Fig. 5.12:	Distribution of steam and water in the pool in PM12 at various times (white area = 100 % steam; dark = 100 % water) Distance between fraction lines: 0.125.	92

Fig. 5.13: Temperatures measured in the freeboard volume (T06) and in the annular gas compartment. 93

Fig. 5.14: Void signals from the freeboard volume (V06) and the annular gas compartment at various heights. The measuring tips were close to the test vessel wall. The signals were treated like those shown in Fig. 2.6. 93

Fig. 5.15: Penetration of water into the annular gas compartment versus time compared with the water level rise. 94

Fig. 5.16: Progression of the water front (drops and slugs) into the annular gas space shown with the time as a parameter. 94

Fig. 5.17a: Distribution of steam and water across the annular gas compartment between 207 and 407 mm height. General time step between pictures: 0.01 s. For the missing times, e.g. 0.480 s, no water was measured. 95

Fig. 5.17b: Distribution of steam and water across the annular gas compartment between 207 and 407 mm height (continued). General time step between pictures: 0.5 s. 96

Fig. 6.1: Pressures determining the melt release: GP12 (melt gen.), PK11 (water pool at –1065 mm), and the pressure difference across the nozzle tube. 99

Fig. 6.2: Speeds calculated for the melt flow in the nozzle pipe. 99

Fig. 6.3: Pressure data obtained in the gas space at 515 mm height. 100

Fig. 6.4: Pressure data obtained in the water at –1065 mm height. 100

Fig. 6.5: Steam flow rates and the time integrated steam volume. 101

Fig. 6.6: Water level measurements; the data have been shifted so that the curves start at the respective initial water levels. 101

Fig. 6.7: Progression of the interaction zone into the water with the time as a parameter. 102

Fig. 6.8: Volumes resulting from the interaction and average volume fractions inside the interaction zone. 103

Fig. 6.9: Post-test particle size distribution of the melt fragments. 104

1 INTRODUCTION

Release of a hot melt into water may occur during a severe core-melt accident in a nuclear light-water reactor. In the course of the accident, the melt may drain down into the lower head of the reactor vessel which is filled with water at that time. Such an event implies the possibility of a steam explosion, whose energetics mainly depend on the extent and characteristics of mixing. Research work in the field of molten fuel/coolant interaction is done within the frame of an EU contract /1/ as well as at other laboratories world-wide.

At Forschungszentrum Karlsruhe, an experimental programme named PREMIX is performed in which the mixing of a hot melt discharged into water is investigated on a medium scale. Strong safety directions as well as similarity considerations led us to choose alumina from a thermite reaction as a simulating material instead of corium. To date, 18 experiments, PM1 to PM18, have been performed under various starting conditions.

The results are firstly used to identify the phenomena that dominantly control the premixing. The information helps in improving multi-phase computer codes presently under development, such as MC3D at CEA Grenoble and at FZK, MATTINA at FZK, IVA5 at SIEMENS and COMETA at JRC Ispra. Secondly, the quantitative results are used to validate the codes.

During PM11, a steam explosion occurred which destroyed the test facility. So far, no explosion occurred in all the other tests. To continue the programme, the facility has been reconstructed with some modifications.

Beginning with PM12, the PREMIX experiments are embedded in the MFCI project of the Fourth EU Framework Programme on fission reactor safety (1996 – 1999). A main task of this project is to compare experiments with simulant melt to experiments which are carried out with realistic corium melts in the FARO/FAT facility at JRC Ispra. For that purpose, the PREMIX facility has been modified to match the FARO conditions as close as possible. For example, the height of the test vessel has been enlarged from 3 to 4 meters. Of course, some differences remain, such as steam venting conditions and expansion volumes.

Results from the first series of PREMIX experiments, PM01-PM11, have already been published /2-4/. The main purpose of the first three experiments in the reconstructed facility (PM12 – PM14) was to study the reproducibility of the results under

nominally identical starting conditions. These experiments were performed on June 26, 1997, October 13, 1997, and February 18, 1998. They cover the P2 classification of the EU-MFCI project.

The main purpose of the follow-on experiments was to study the influence of elevated system pressure, larger melt masses, and strong water subcooling, respectively, covering P1, P3 and P4 of the project.

The present report is a detailed documentation of conditions and results from PM12, PM13, and PM14. Although nominally identical test conditions were aspired, some inevitable differences occurred which gave rise to some deviations in the results, in addition to statistics. Special attention is paid to these items throughout the report. Nevertheless, an important conclusion will be that the results are very well reproduced.

The presentation and discussion of the results that constitute the body of this report are started with PM13 and PM14 whose conditions proved to be rather similar. PM12 is presented in the third place, since unintendedly a larger mass of melt has been released and – due to an error in the flow meter system – no data on steam flow through the venting pipes were gained. Being aware of these disadvantages, we decided to perform, after test PM13, PM14 additionally.

The evaluation of experiments PM15 and upward is almost completed. Results are being presented in separate reports. A comprehensive report on all tests, PM12 to PM18, will follow. At last, the reader's attention is drawn to the fact, that *figures* in this report are placed at the *end* of each chapter.

2 EXPERIMENTAL SET-UP AND TEST PROCEDURE

2.1 Test facility

The main component of the reconstructed test facility (see Fig. 2.1) is a cylindrical vessel having 700 mm in diameter and 4 m in height. The height was increased by introducing a one-meter middle part to achieve a water depth comparable to that of the FARO test facility. The vessel has flat glass windows at the front and the rear to allow illumination as well as high-speed photography and video filming.

Two other components are the melt generator located in the upper part of the vessel and the water pool. The gas volume (also called gas space or gas compartment) comprises the freeboard volume between water surface and the bottom of the melt

generator and the annular gap between the melt generator and the vessel wall. The melt is collected at a dish-like circular fragment catcher (also called catcher pan in this report) mounted in the bottom part of the water pool.

The vessel is completely closed except for the four venting tubes. Water separators mounted in each tube are to separate water droplets carried with the outgoing steam.

2.2 Melt generator

The melt was generated by a thermite reaction in a crucible (Fig. 2.2) according to the equation:

$8\ Al + 3\ Fe_3O_4 \Rightarrow 4\ Al_2O_3 + 9\ Fe + 3732\ J/g.$

The reaction products, alumina and iron, separated during the reaction due to their different densities. Using this effect, the melt generator was constructed to provide mainly the oxidic part of the melt.

The upper part of the crucible was composed of two sections, a cylindrical section and a funnel section. The latter was internally structured: the conical area was broken up by four vertical slots having 60 millimetres in width through which the iron was led to an annular cavity located underneath. The cavity, initially closed by a steel membrane (first steel membrane), was due to retain the iron. The thermite powder extended down to another steel membrane (second steel membrane) located in the nozzle, 90 mm below the crucible bottom. This membrane separated the thermite filling from the steam/gas atmosphere below.

The melt release, which was supported by a small overpressure, occurred through the circular opening in the bottom which was in one the upper end of the nozzle tube (for more details of the procedure see Section 2.4.2).

2.3 Instrumentation

The instrumentation comprised various types of measuring devices.

Pressure transducers were mounted in the water, the freeboard volume, the venting tubes, and the melt generator (for locations of the transducers see Figs. 2.1 to 2.3). Mainly three types of pressure transducers (Table 2.1) were used: piezo-electric transducers, strain gauges, and piezo-resistive transducers. The advantage of the piezo-electric type is its short response time which is important in case of a steam explosion. The strain gauge type is better suited in case of longer lasting pressure

events, piezo-resistive transducers give absolute pressure data. This combination was chosen to get reliable data for various kinds of pressure events even for the steam explosion case. The output signals were redundantly recorded: (1) by fast transient recorders with less resolution, (2) by medium fast transient recorders with high resolution, (3) by tape recorders suited for long-term pressure evolution, and (4) by digital data logger.

The *steam outflow* was recorded by vortex flow meters. It had become apparent after the first few tests that water separators had to be inserted in the venting lines to keep

Table 2.1 Characterization of the pressure transducers. See also Figs. 2.1 and 2.2 for more details

Designation	Location z (mm), etc.	Type/setting	Measuring range, MPa	Remarks
PK01	1200	strain gauge	0.35	
PK02	515	strain gauge	1.7	
PK03	515	piezo/long	5.0	
PK04	315	strain gauge	0.35	
PK05	115	strain gauge	1.7	
PK06	-65	piezo/long	5.0	
PK07	-65	strain gauge	0.35	
PK08	-465	strain gauge	1.7	
PK09	-465	piezo/long	5.0	
PK10	-865	strain gauge	0.35	
PK11	-1065	strain gauge	1.7	
PK12	-1265	strain gauge	1.7	
PK13	-1265	piezo/medium	5.0	
PK14	-815	piezo/long	1.0	only in PM14
PK15	-815	piezo-resistive	0.2 (abs.)	only in PM13
PK16	-1415	piezo-resistive	0.5 (abs.)	only in PM13
PC01	Venting pipe #1	capacitive	0.25	
PC02	Venting pipe #2	dito	0.25	
PC03	Venting pipe #3	dito	0.25	see also Fig. 2.4
PC04	Venting pipe #4	dito	0.25 abs.	
PC05	Venting pipe #3	dito	0.25	see also Fig. 2.4
PC06	Venting pipe #3	dito	0.25	see also Fig. 2.4
GP11	Gas supply line	piezo-resistive	0.5 (rel.)	
GP12	Melt generator	piezo-resistive	0.5 (rel.)	

errors in the flow measurement low. Measurement disturbances arise from water drops and slugs entrained with the steam flow. Unfortunately, the steam flow meters failed in PM12 because of a missing plug-in connection.

Several measuring *lances* were mounted at various axial levels and azimuthal positions in the water pool as well as in the freeboard volume. For the axial location of the lances see Fig. 2.1. The lances were equipped with eight (in the annular gap space with three) *void sensors* distributed at equal distances and a *thermocouple* at their ends (Fig. 2.4). Void and thermocouple data were used to evaluate the evolution of the interaction zone, void data were used to show local distributions of steam and water in the pool for a given time.

The *void sensors* indicated whether or not there was water at their measuring tips; these are in principle coaxial wires whose open ends form a cross wire or an open circuit, respectively. Note that the tips were located at a vertical distance of 8 mm from the lance axis, upside or downside, depending on whether the lance was mounted in the water or in the gas space. In total, 114 void probes were available.

Thermocouples (sometimes abbreviated t/c in this report) located in the plain vessel were at a distance of 25 mm from the axis, those in the annulus at a distance of 5 mm from the melt generator housing. Thermocouples indicated the change of phase from (colder) water to steam which was at higher temperature. They also indicated the instants when melt contacted their measuring tips.

Under the presumption of an axis-symmetrical melt penetration, the thermocouples in the water were the first to be seized by the steam/liquid interface of the interaction zone. Hence, the probability of damage by a compact melt stream was high.

High-speed cameras taking 2000 frames/s (time of exposure: 1/4000 s) and video cameras (50 frames/s) were used to record the phenomena of the experiment.

Since the actual *melt flow rate* could not be measured, it was calculated on basis of pressure measurements.

Six *steel bottles* were used to take *gas samples* prior to and during the interaction. The bottles were evacuated prior to the test and connected to the freeboard volume via solenoid valves. The gas samples provided information about the composition of the steam/gas atmosphere, especially about a possible generation of hydrogen. It was in PM12 when steel bottles were used for the first time. The valves were actuated by a programmer which also controlled the ignition of the thermite. The first

valve opened about 1.5 s prior to the time of melt release; the others followed with time increments of 0.2 s, starting 0.5 s after the onset of melt release. The opening time of a valve was 0.2 s.

2.4 Experimental conditions and test procedure

2.4.1 Test parameters

The experimental conditions of PM12 - PM14 are summarized in Table 2.2. The conditions comprised both preset and measured data. Preset data were: the composition and mass of the thermite powder mixture, the driving pressure inside the melt generator, the water temperature, and the falling height of the melt. An overfilling of the crucible with thermite powder occurred unintendedly during the preparation of PM12 test, causing an excess of melt released. Variations in the height of the initial water level were due to the heat-up procedure prior to the test.

2.4.2 Test procedure

The experiment was started by igniting the thermite mixture at the top (Fig. 2.2). Gas and smoke produced during the chemical reaction escaped through a separate venting line. When the reaction front reached the bottom of the crucible, the annular cavity mentioned above was opened by melting of the first steel membrane. The heavier iron drained into this compartment and was thus prevented from being released.

Table 2.2: Experimental parameters of tests PM12 - PM14

		PM12	PM13	PM14
Melt				
Mass released	kg	29.0	23.8	23.2
Temperature	K	2600		
Composition (by mass)		>90% oxides, <10% iron		
Melt release				
Initial nozzle diameter	mm	60		
Initial driving pressure	MPa	0.046	0.052	0.066
Falling height	mm	193	213	213
Water				
Depth	mm	1360	1340	1340
Temperature	K	372	372	373
Subcooling	K	1	1	0
System pressure	MPa	0.1		

The reaction front proceeded into the nozzle tube, thereby contacting a sensor located at a distance of 20 mm above the second membrane. The contact triggered both the closure of the venting valve and the temporary opening of a gas storage. The latter induced a defined pressure rise in the crucible gas atmosphere. On its way down the nozzle tube, the melt front melted the steel membrane. It is concluded from film pictures, showing the initial melt release, that this melt-through did not always occur exactly in the same way. Accordingly, the initial melt release occurred as droplets or as a thin jet. The full size of the jet, i.e. the size that corresponds to the internal diameter of the nozzle, was generally observed some tens of milliseconds after the appearance of the first droplets.

2.5 Data acquisition

The data are recorded by

- transient recorders,
- data logger, and
- digital tapes.

The ranges of the measuring devices are preset. The signals were amplified and normalized, typically amounting up to 10 Volt after amplification. All registration units including the high-speed cameras were synchronized by means of a real-time online clock.

To reduce the probability of data losses, the important signals were picked up twice, once with a "normal" recording frequency, a second time with a much larger recording frequency. This precaution also served to get information even in the case of an unexpected steam explosion. Of course, with respect to the pressure data, a higher time resolution, which is desirable in case of very fast changes, results in less accuracy in the amplitude (8 bit registration).

2.6 Data evaluation

This section is to explain how the data were evaluated and to help in judging the results presented below. Note that the time when a substantial melt mass first contacted the water surface is defined as the origin of the time axis (t = 0) in all tests.

2.6.1 Pressure measurements

Because the voltages of the piezo-electric pressure transducers use to drift away from zero level and since also the zero level of the strain gauge transducers is not

well defined, the data were calibrated considering actual environment conditions at zero time (0.1 MPa). By this, absolute pressure data were obtained. The geodetic height of the water was not considered in the calibration in those measurements that were obtained from sites below the initial water level.

The same calibration procedure had been applied in all former experiments. To meet the suspicion of falsification of the data, possibly resulting from this procedure, and to check the accuracy of the data obtained from piezo-electric transducers, new piezo-resistive pressure gauges giving absolute pressure data were used in tests PM13 and PM14.

2.6.2 Melt release

Knowledge about the time history of melt release is essential for an appropriate numerical simulation of the PREMIX experiments by a computer code.

Since the melt release rate could not be measured, it was calculated on a simple numerical model using pressure time histories measured inside and outside of the melt generator, GP12 and PK11, respectively. The model is based on a momentum equation describing the flow of melt in a pipe. For more details see Appendix A. The results were used in the evaluation of average volumetric fractions of the components inside the interaction zone.

2.6.3 Level measurement

The change of the water level was measured by use of four capacitive probes that were housed in steel tubes plunged into the water. The lower ends of the tubes were open, i.e. the water level within the tubes was measured. The probes were calibrated at room temperature a few hours prior to each test. The calibration coefficients were then applied to the measurements. The curves shown in the respective figures of this report have been shifted to account for the actual water level noted at the start of the test. The shift gives the effect of different temperature conditions (373 K) predominant during the test. Very fast changes of the water level can not be reproduced. It should also be noted that only the liquid water phase contributes to the signal voltage. Steam bubbles, that had been transported to the outer regions of the water pool where the level probes were situated, caused the actual water surface to be higher than the measured one. This condition was more pronounced at later times during the test.

2.6.4 Void and temperature measurements

For illustration, three sets of void signals are shown in Figs. 2.5 (a) to (c). Figures (a) and (b) give signals obtained from the water pool in the radial and axial directions, respectively. Figure 2.5 (c) gives signals obtained in the gas space. The void measurements provided two kinds of information:

(1) The first changes in the signal voltage (Figs. 2.5 a and b) indicate the instants at which first local changes of the phase occurred from liquid to gas. The ascending times of the first signal rises illustrate, at a first glance, the expansion process. These data enable us to construct the extension of the interaction zone in the water pool with the time as a parameter.

    The first signal changes from gas to liquid (Fig. 2.5 c) indicate the progression of water moving as droplets or slugs into the gas space.

(2) The frequent changes in a signal following the first change give information about local "densities" of steam and water if projected to narrow time windows.

The thermocouple signals (see e.g. Fig. 3.10) give, as mentioned, good information about the melt penetration rate along the vessel axis. A marked ramp appears in the signal when the steam/liquid interface passes the thermocouple tip, a very steep increase indicates destruction.

Progression of the interaction zone (above item #1). The instants of first switches from liquid to steam in the signals of all void sensors located in the water, combined with the respective r-z coordinates, were taken as an input to a small numerical programme. The programme which uses an interpolation algorithm gives the boundary of the interaction zone with the time as a parameter (see e.g. Fig. 3.11). It should be noted that, because of the limited number of measuring lances, the data of all sensors were used in the programme regardless of the azimuthal positions of the lances.

In those cases, where the contour in a film picture (Fig. 3.1) showed a larger extension (in the radial and/or axial directions) of the interaction zone than it was determined by the above numerical programme, the extension was evaluated from the film picture. The procedure was such that the width of the contour of the interaction zone was taken from the picture as a function of the height. Half of the width was taken as a radius and entered in the diagram. Obviously, the delay in the void data (compared to the film data) was caused by the way in which the expansion of the interaction zone

took place. Sometimes, it occurred in a slightly non-symmetrical way as can easily be observed in the films.

Film pictures were mostly used to determine the lowermost boundary of melt penetration. On the other hand side, the sensor data were especially used when the boundary of the interaction zone could no more be observed through the glass windows. These circumstances have to be considered in assessing the results.

Distribution of steam and water (above item #2). The first step of evaluation is illustrated in Fig. 2.6 where two different void signals are presented for example. The upper graphs give the normalized signals. As mentioned, the frequent signal changes between zero and unity following the first change express local variations between "steam" and "water". Smoothing of the normalized signals was required to obtain a new set of data that is better suited for graphical presentation. This goal was achieved by applying a filter routine with a time window to the signals. By this, the data were averaged over a short period of time, i.e. 0.01 s in the actual case. The result is shown in the two lower plots.

In the second step, the amplitudes of the smoothed data at a given time and the respective coordinates are taken as an input to a commercial software programme which provides a plot showing the distribution of steam and water with the volume fraction as a parameter (Fig. 2.7). The fixed numbers at the abszissa of this figure and the labels, V07 to V16, running across the axial height, represent the radial and axial coordinates of the measuring tips, respectively. It should be noted that the measuring tips are located at a distance of 8 mm from the axis of the lances.

The data of sensors located in the gas space were used to show the distribution of steam and water in the annular gas space (see e.g. Fig. 3.20)

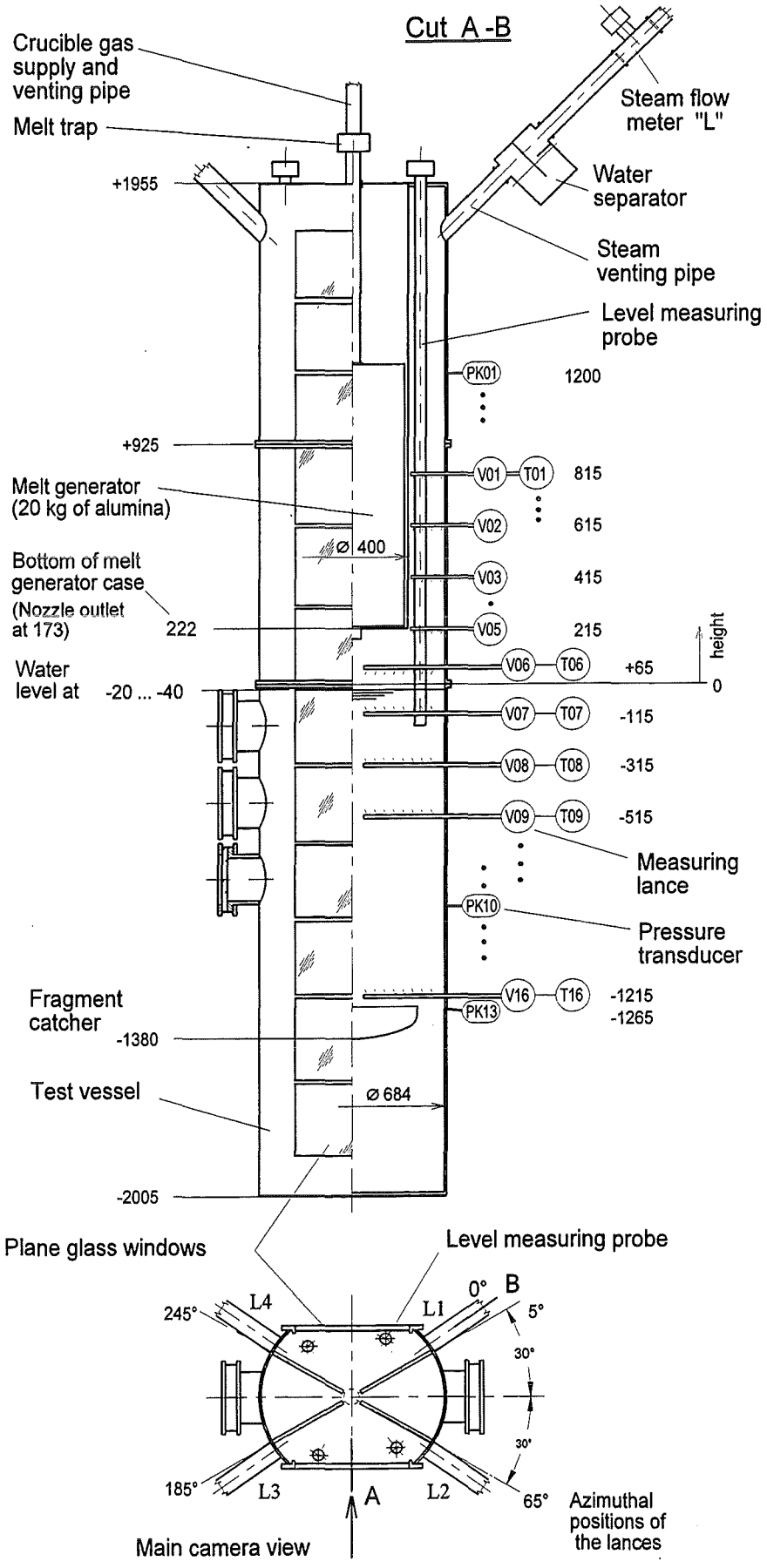

Fig. 2.1 Test facility used for PM12, PM13 and PM14

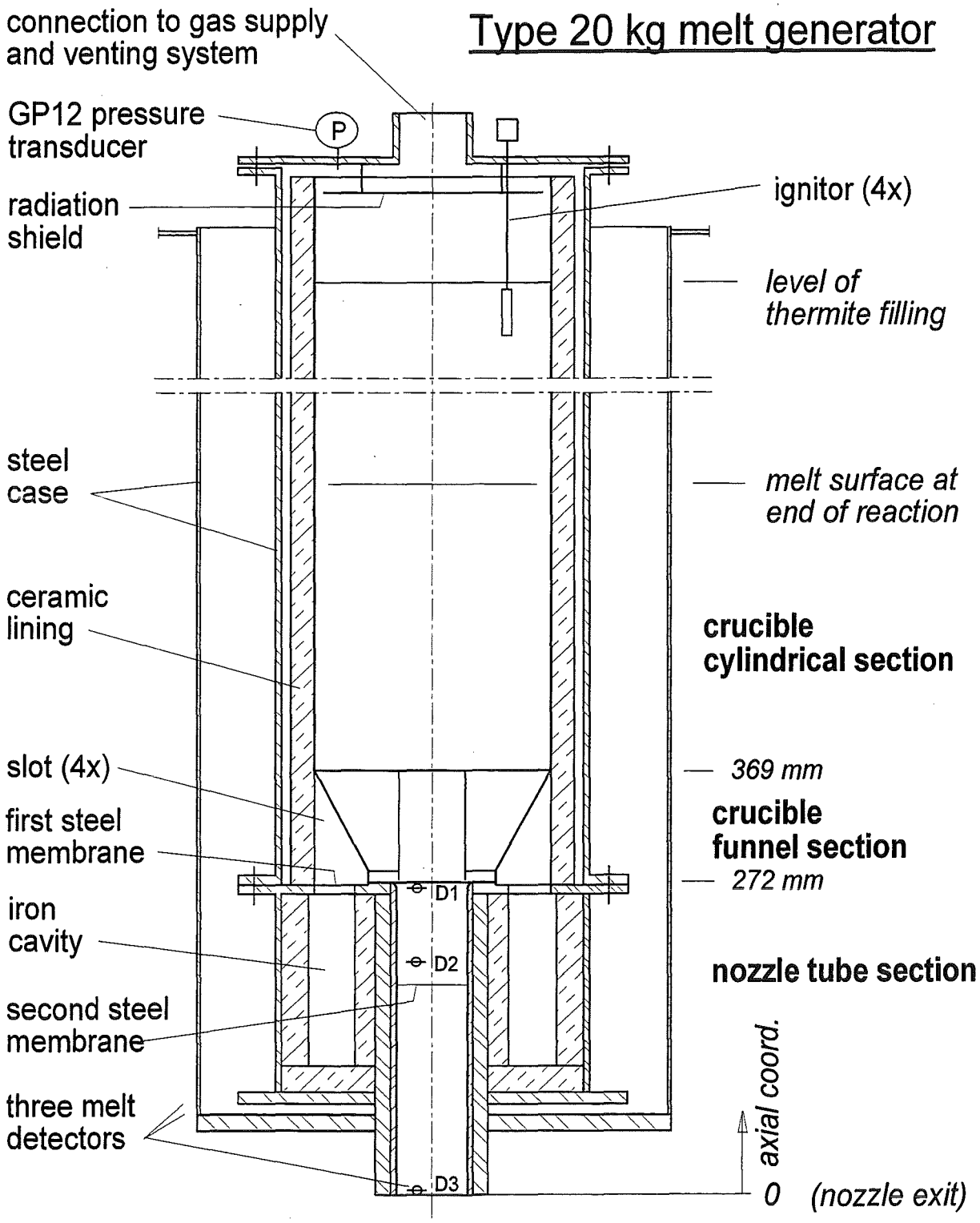

Fig. 2.2 Schematic of the melt generator. Note that the axial coordinate of the melt generator is different from that of the test vessel (Fig. 2.1).

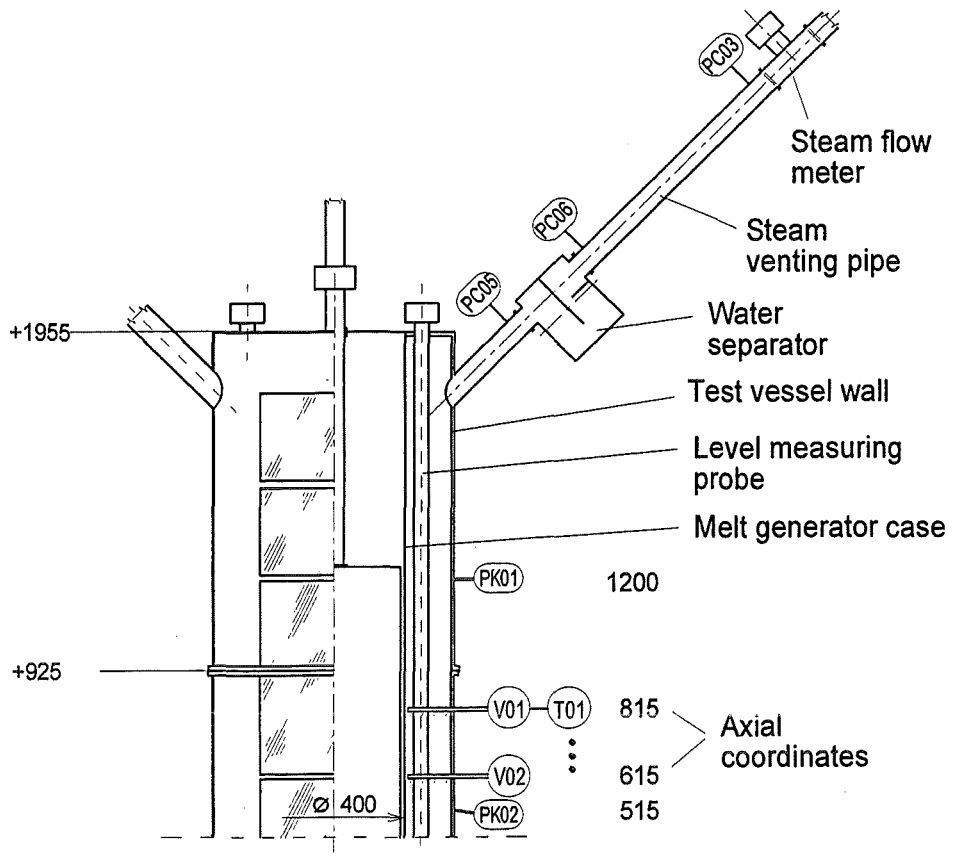

Fig. 2.3 Locations of the pressure transducers mounted in the annular gas space and in venting line No 3.

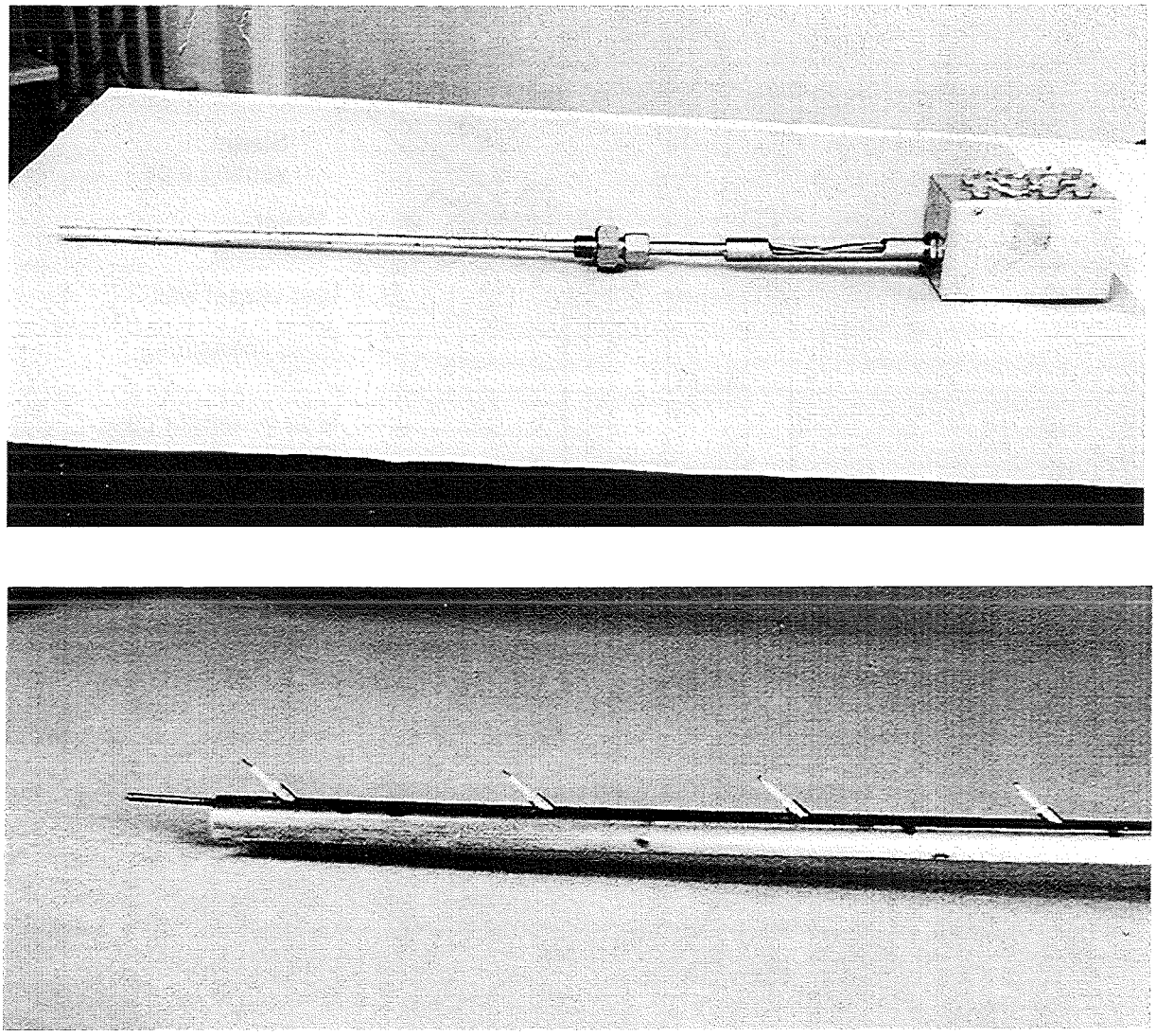

Fig. 2.4 Construction of a void lance. The major parts are (upper picture from left to right): a body carrying the sensors, threaded joint which is in the realm of the vessel wall, carrier tube, and connection box. The lower picture shows four of the eight sensors and the thermocouple at the free end.

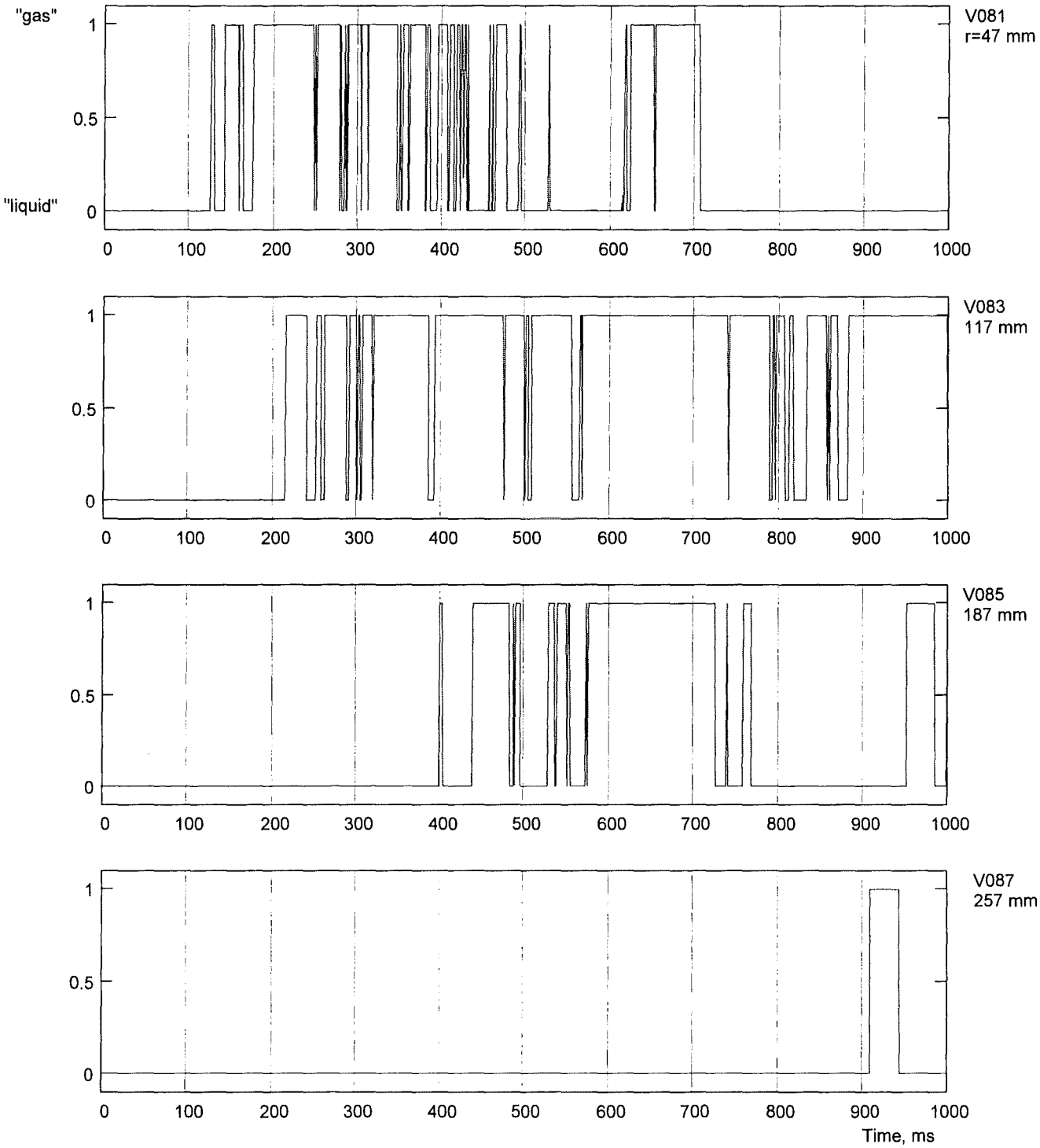

Fig. 2.5 a Void signals obtained in PM14 from the V08 measuring probes located 270 mm below the initial water level. The radial coordinate increases from top to bottom.

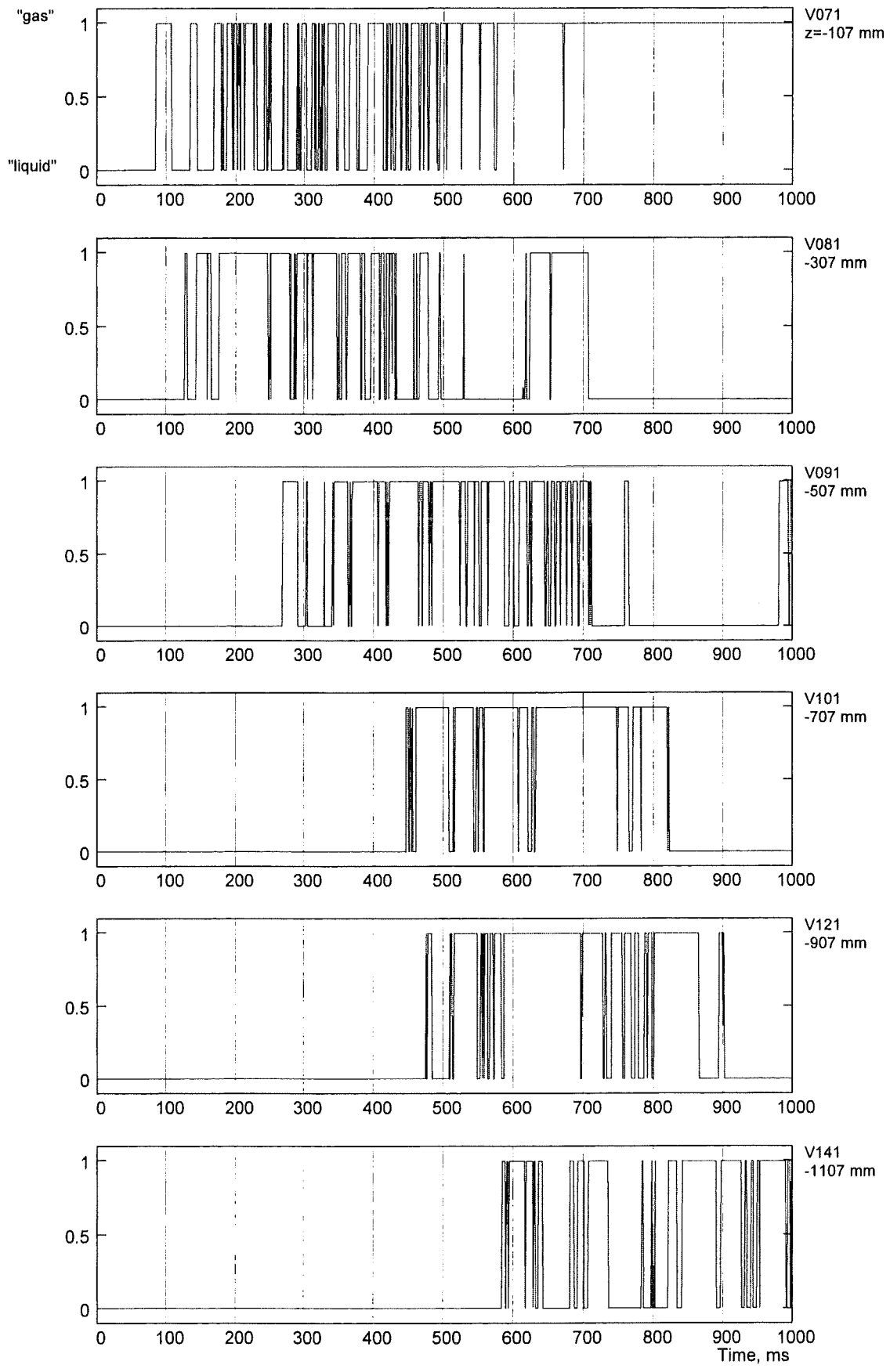

Fig. 2.5 b Void signals obtained in PM14 at various heights close to the vessel axis.

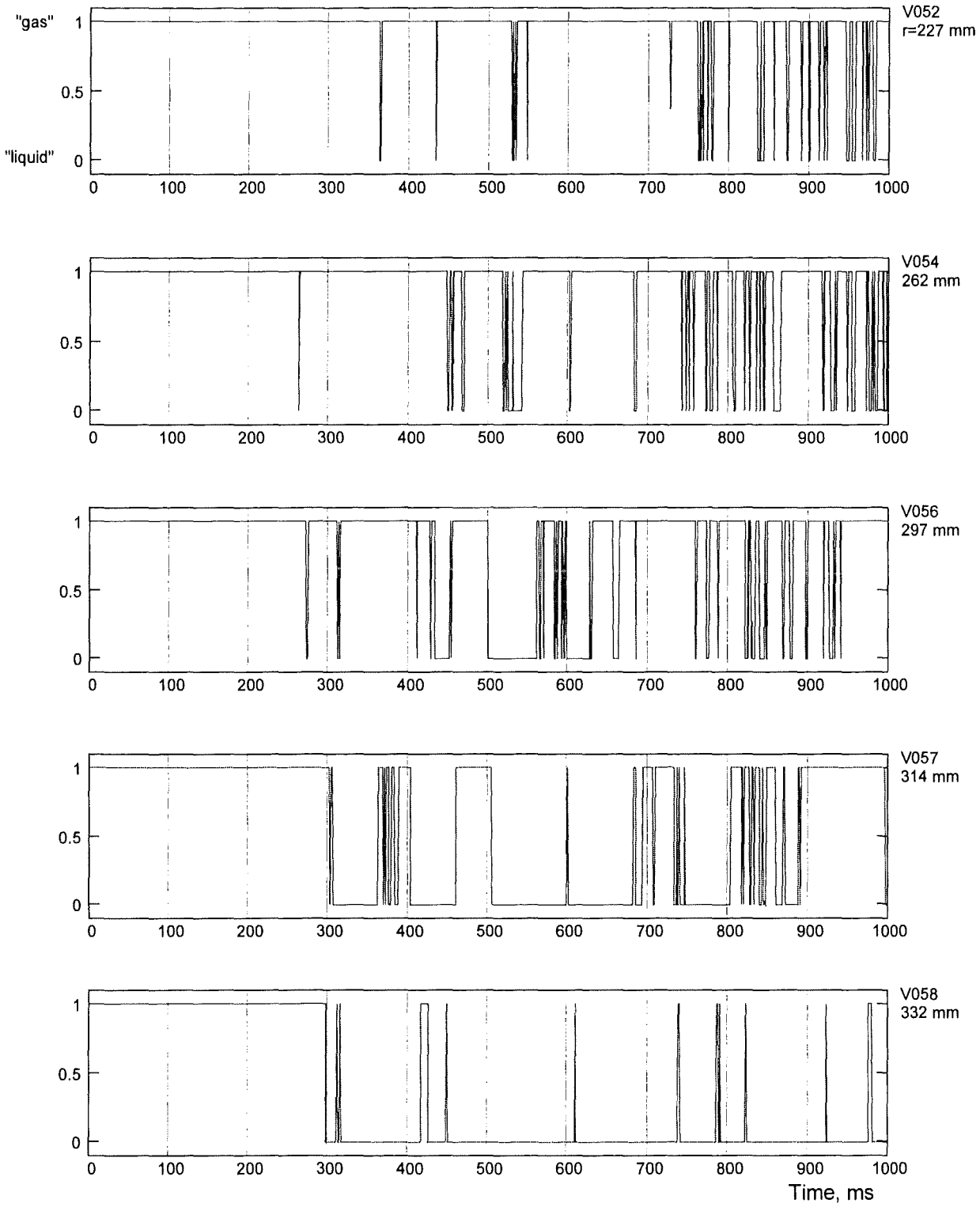

Fig. 2.5 c Signals obtained in PM14 from the V05 lance located in the annular gas space 250 mm above the initial water level.

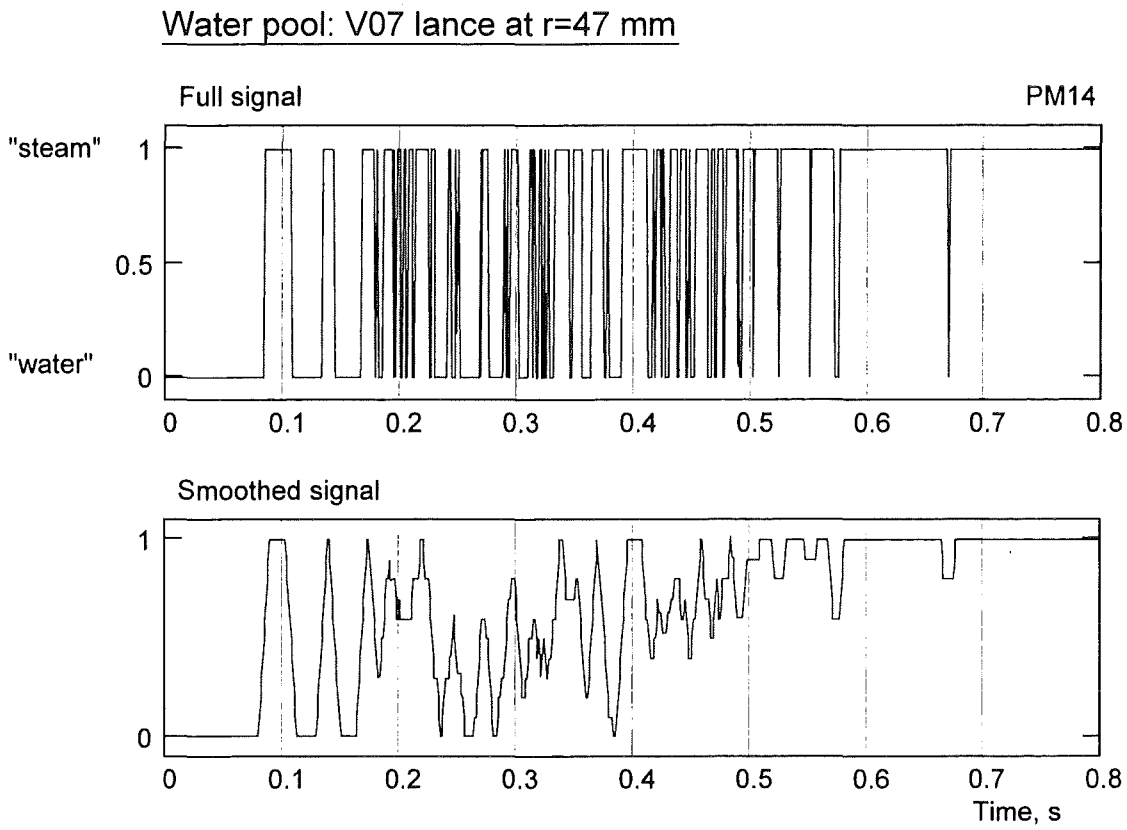

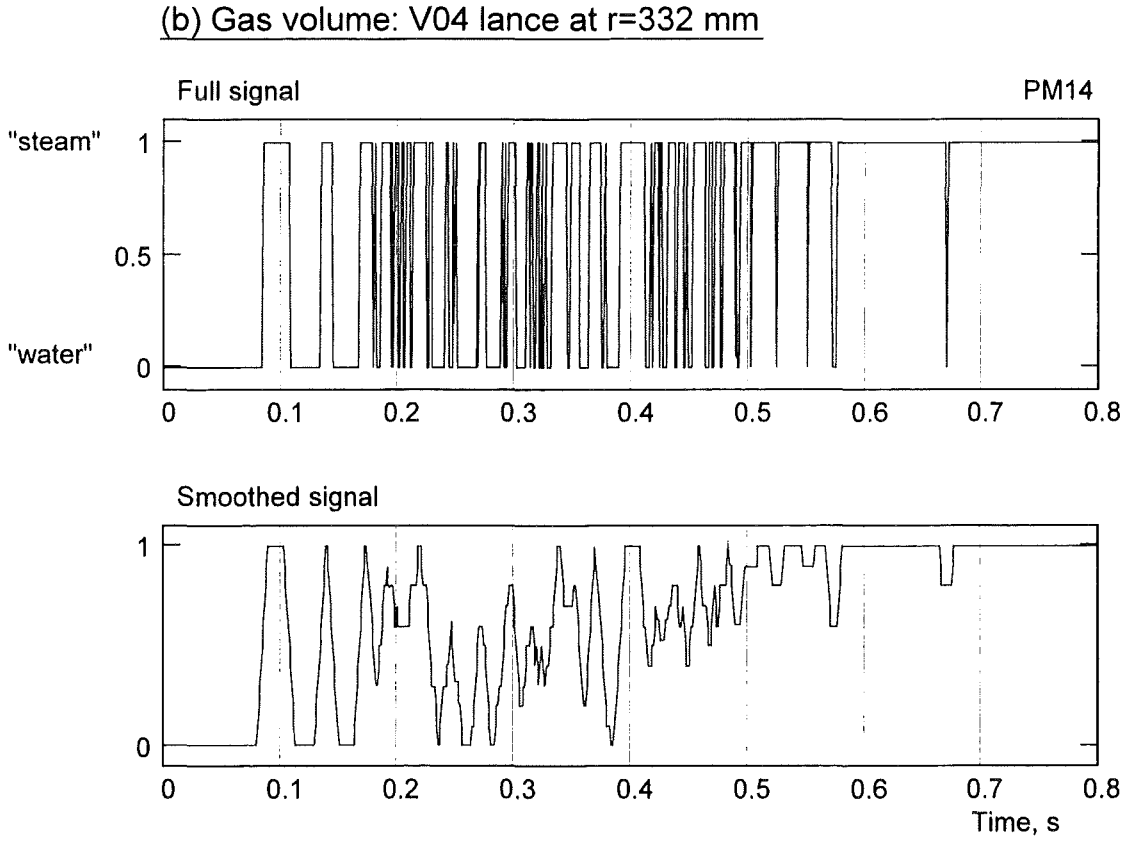

Fig. 2.6: Processing of void signal data obtained in the water (a) and in the gas (b). Smoothing was performed by integration using a window width of 10 ms.

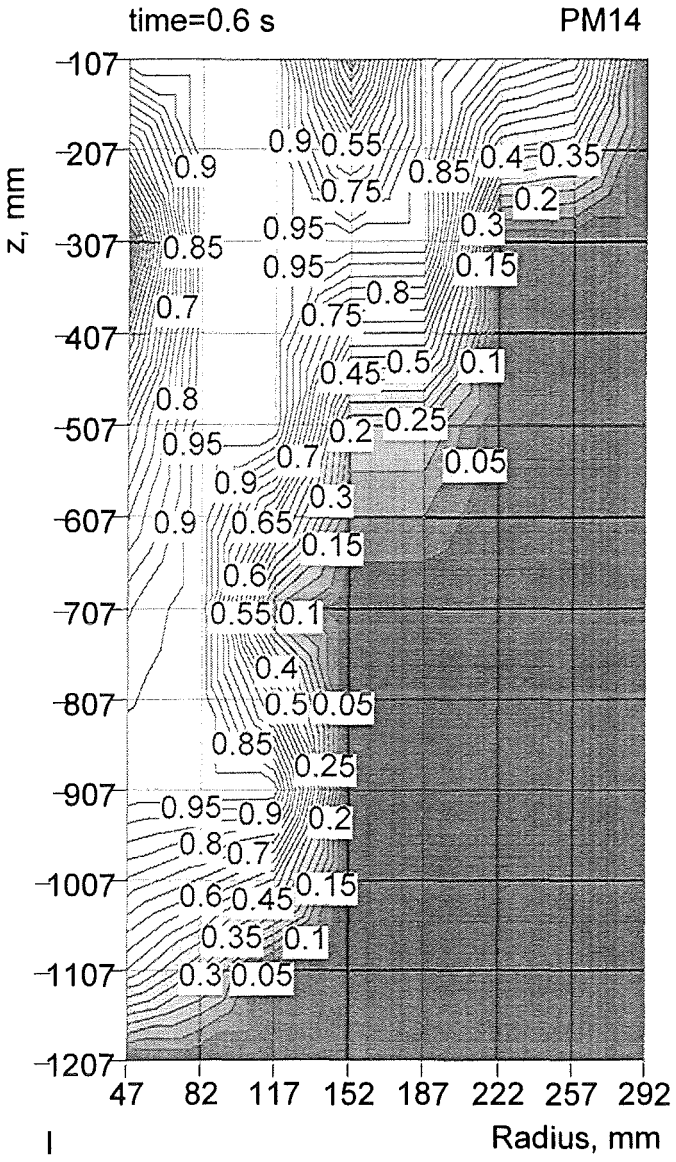

Fig. 2.7: Example: Distribution of steam and water in the pool at const. time. Parameter is the volume fraction; white area ≈ 100% steam; dark = water.

3 RESULTS OF PM13

3.1 General course of the experiment

A short description of the characteristic events is given in this subsection. It is mainly based on video (Fig. 3.1) and high-speed films which give good information about the start of melt penetration as well as about the growth of the interaction zone in the axial and radial directions. It should be noted that in all tests the camera view slightly deviated (by 7.5°) from the normal to the glass windows. As soon as gross boiling had established in the pool, information from the films is merely available about the processes that take place closely behind the glass windows. The evaluation of the void signals which give a more localized information provides us, on the other hand, a tool to "look into" the interaction zone.

The melt release started as a shower of droplets. The first melt droplet appeared at the nozzle end at -0.074 s; this time was stated in the high-speed films. It should be noted that, due to the discrete filming at 50 frames/s, the times ascribed to the video pictures (e.g. in Fig. 3.1) agree within a margin of accuracy of less than ±0.010 s with the established time coordinate. The average speed of the droplets, 2.9 m/s, was calculated with the falling height of 213 mm and the travel time between nozzle end and water surface, 0.074 s. The contour of the succeeding melt flow was conical with diameters of about 60 mm at the nozzle outlet and 100 mm at the water surface. The contour became more cylindrical with time. The aperture angle of the contour (related to the vessel axis) decreased from about 5° at the beginning to 2.7° at the time 0.080 s. From 0.180 s on, the contour was rather cylindrical.

As the melt stream appeared to be neither compact nor a spray, we presume that it consisted of melt and gas in equal shares. On leaving the nozzle end the melt stream rolled somewhat around the vertical line. This behaviour might have been the result of fluctuating mass velocities inside the nozzle tube due to varying gas contents. The melt speed was reduced on contact with the water (see Sections 3.2 and 3.31).

At time 0.320 s, when the melt had penetrated about 440 mm into the water, the intensity of interaction and with it the steam generation were strongly enhanced. The interaction zone expanded faster than before in axial and radial directions. As a consequence of the enhanced steam generation, the melt stream was no more visible, i.e. the character of melt release could no longer be identified.

The speed of the leading melt front in the water, which could well be followed especially in the high-speed films, slowed down due to interaction. The lower rate remained almost constant over a penetration length of 1070 mm. Afterwards, the penetration rate slowed down again until the bottom of the fragment catcher was reached at 1.020 s.

3.2 Pressure, steam flow, and level measurements

The pressure measured in the water as well as in the gas space gives immediate information about the intensity of thermal interactions. In addition, the pressure difference between melt generator and the interaction zone allows to draw conclusions on the duration and rate of melt release.

Estimation of the melt release function from pressure data Firstly, the pressures measured inside (GP12) and outside (PK10) of the melt generator (Fig. 3.2) are discussed. The GP12 pressure was increased as intended in one step between times -1.4 and -1.2 s. The subsequent increase that occurred at a smaller rate till about time zero was due to heat transfer from the melt to the overlying gas. The loss of melt volume diminished the pressure increase in the crucible until, from time 0.2 s on, the pressure remained approximately constant for a short period of time. As mentioned, the first melt droplet appeared at the nozzle end 0.074 s prior to the first melt/water contact. The instant when melt melted through the steel membrane (–0.10 s), has been derived from the path-time function of the very first melt droplet taking also into account the very first rises of pressures recorded at short distances below and above the initial water level.

The pressure outside of the melt generator is illustrated by the PK10 pressure trace which shows different periods of increase: the slow increase starting at time -0.06 s is followed by a very steep increase, an intermediate slower rate, and, at last, a steeper rate up to the first maximum.

The PK10 pressure seems to have influenced that within the melt generator: The steep PK10 rise between 0.3 and 0.6 s prevented the GP12 pressure from a marked decrease due to the loss of melt volume. When the PK10 rate became smaller, from about 0.6 s on, the GP12 pressure even showed a small increase. During the last increase, from about one second on, the pressure outside of the melt generator be-

came larger than that inside. This event is taken as an indication of the end of continuous melt release.

Figure 3.3 gives, besides pressure data, results of the calculation on the numerical model mentioned. These are the melt speed, integrated mass flow rate, and height of the melt surface in the crucible as functions of time. Some explanations are given in the following, for more details see Appendix A. As mentioned, melt-through of the nozzle steel membrane occurred at -0.1 s. This time was taken as the start of calculation. The melt mass made available for release agrees with the mass of the fragments collected after the test; it determines the initial height of the melt surface in the crucible (see Fig. 2.2). The melt is accelerated from the state of rest. Its front proceeds from the location of the membrane to the lower end of the nozzle tube. Accordingly, the speed of melt is related to the nozzle cross section.

The calculated speed of melt (Fig. 3.3) increases rapidly. The average speed, calculated for the period of time between 0.074 s and zero, amounts to 2.55 m/s. This value compares well with the initial speed of melt droplets (2.9 m/s) mentioned above (speeds of melt penetrating into the water are given in Section 3.3.1). The calculation was stopped when the melt surface reached the lower end of the nozzle tube (1.08 s). The integrated mass flow rate reached the given mass, 23.8 kg, a little earlier, i.e. when the melt surface arrived at the height of the membrane (0.182 m). The time (1.08 s) agrees with the instant at which the measurements showed pressure equilibrium for the first time. This condition was probably caused by gas break-through. A residual quantity of melt could have been released afterwards due to inertia and gravity forces. We assume that no more melt was released from time 2.2 s on when permanent pressure equalization was indicated (Fig. 3.2).

The calculated function of integrated mass flow rate (Fig. 3.3) is regarded as a good approximation of the real melt release function. Hence, it was used in the estimation of average volume fractions inside the interaction zone (see Section 3.3.2 below).

Pressures below the initial water level Figure 3.4 shows the data obtained from several strain-gauge pressure transducers generally used in the PREMIX experiments. The pressure rises occurred stepwise giving evidence of a non-uniform expansion of the interaction zone with time. As mentioned, it was in this test when two piezo-resistive pressure transducers were used for the first time. These give absolute pressure data which were used to check the accuracy of the dynamic pressure data

obtained with the strain-gauge transducers. Comparison is made in Fig. 3.5, where the PK15 (absolute pressure) and the PK10 (dynamic pressure) traces are shown. Since the PK15 curve (as measured) includes the respective geodetic height of water, the curve has been shifted and redrawn to meet the initial ambient conditions (0.1 MPa). In fact, the shifted curve masks the reading of PK10.

Pressures in the gas space are shown in Fig. 3.6. The curves started to rise about 0.3 s after the first melt/water contact. Further increases occurred stepwise until a maximum of 0.17 MPa was reached. The signal of the PK01 transducer located uppermost (+1200 mm) started to deviate from the other curves from 0.7 s on, the reason for which is unknown. The signals of the PK03 and PK06 pressure transducers have been omitted in the figure; they are suited to give good measurements in case of a steam explosion.

Steam flow rate The four individual steam flow rates (F01-F04), the total rate, and the integrated steam volume are given in Fig. 3.7. Comparison with Fig. 3.6 shows that the initial increase in pressure is delayed by about 0.2 s compared to that in steam flow rate. This means that the steam flow pressure losses were very low, initially.

From time 0.6 s on, after the first maximum, the steam flow rate remained approximately constant for another 0.7 s, whereas the pressure in the pool (Fig. 3.6) continued to rise, yet at a reduced rate. This finding can be interpreted by an increase in the loss coefficients due to increasing drag of water droplets in the steam flow. In fact, evaluation of the void signals obtained in the annular gas space (see Section 3.4 below) shows that a noticeable amount of water droplets reached the elevation of venting pipe branch-off at about the time (0.7 s) when the steam flow rate became constant.

Two of the four flow meters (Fig. 3.7) show intermediate signal break-downs, the first one after 1.3 s. Such disturbances in the flow meters used to occur when a marked amount of water was dragged as droplets with the steam. The integrated steam volume amounts to about 6.5 m^3 after 2 s. This value, which is only 10 % of the maximum steam volume that could have been produced by the melt, reflects the limited heat exchange due to incomplete intermixing.

Change of the water level Data of the four level measurements are given in Fig. 3.8. Three of the signal traces show uniform level rises, while one trace (L03) deviates considerably towards larger values. We do not know the reason for this.

3.3 Development of the interaction zone in the water

Data base: void and temperature measurements The results presented in this section are based, besides on film pictures, on void and temperature measurements. In support of the dicussion, two selected sets of void signals are presented in Figs. 3.9 (a) and (b). Readings of thermocouples are drawn in Fig. 3.10. The data are briefly discussed in the following.

The V06 and V07 void signals give information about the varying phase conditions in the zones above and below the initial water surface, respectively. Especially the progression of the interaction zone in the radial direction is visible in the sequence of first changes from "liquid" to "gas" level in the V07 signals.

First rises in temperature signals (Fig. 3.10) indicate the passing of the steam/liquid interface of the expanding interaction zone. The rises caused by elevated local steam temperatures always occurred with a short delay which was determined by the response time of the thermocouple. An extraordinarily steep rise, sometimes occurring later on, indicated destruction of the thermocouple by melt.

3.3.1 Progression of the steam/liquid interface

Figure 3.11 illustrates the progression of the interaction zone in axial and radial directions into the water. The result was derived from void data as well as from film pictures (compare Section 2.6.4).

The shapes of the boundary lines show that the melt produced a relatively narrow channel composed of melt, steam, and water (particles). The upper rim of the fragment catcher (-1260 mm) is reached at about 0.8 s. The varying density of the lines allows to draw conclusions on local speeds of expansion. For example, the progression of melt along the vessel axis can easily be shown by evaluating thermocouple signals and film pictures. The result is shown in Fig. 3.12. The advance of the film data compared to the t/c data, which is 120 mm or 0.1 s on an average, is due to the acutely conical shape of melt penetration which sometimes occurs as a small cluster of melt fragment (see Fig. 3.1) along with the fact that the t/c tips were at a distance of 25 mm to the vessel axis. Speeds of penetration (Fig. 3.12) are 2.7 m/s in the very

beginning (at 0.05 s) and around 1.5 m/s afterwards. The slow-down of the speed at 0.7 s coincides with the conclusion that can be drawn from film observation, namely that the melt stream was largely fragmented from that time on.

Melt penetration and formation of steam caused the water level to rise. It is anticipated that the initial rise of the water went along with surface waves expanding concentrically caused by the plunge of the melt into the water. This can be seen in the V061 – V064 void signals obtained at a distance of 96 mm above the initial water level (Fig. 3.9a). One can conclude from the V06 signals that steam was the dominating phase in the region close to the pool centre (V061), whereas larger liquid fractions over time appear in the zone close to the vessel wall (V067 – V068). This result, together with the measurements obtained from the annular gas space (see below) indicates that it was the zone close to the wall where the water preferrably moved up.

3.3.2 Volumes and average volume fractions resulting from the interaction

Figure 3.13 shows volumes generated as a consequence of the interaction and average volume fractions of the three components within the interaction zone. The volume of the multiphase interaction zone (MIAV) was calculated from the lines drawn in Fig. 3.11 assuming rotational symmetry, the other lines are the result of the calculation described in detail in Appendix B. It should be noted that reasonable results can be obtained only between about 0.05 s and 0.5 - 0.6 s. The reason is that the measurements are absolutely very small initially which results in relatively large errors, and later, after about 0.5 s, errors become large in determining the steam/liquid interface in the water pool as well as the upper limit of the interaction zone.

The most significant volume, i.e. the volume of the multiphase interaction zone, in creased steeply from the beginning; it doubled in size every 0.1 s from about 0.1 s on. Next to this volume, as regards the size, are the volumes of liquid, steam, and melt, respectively, which are present within the interaction zone. The volume of the level rise is an intermediate function used in the mass and volume balance (see Appendix B). The time histories of the average volume fractions (lower diagram) give key informations about the distribution of steam, liquid (water), and melt in the interaction zone. To facilitate the discussion of the results two essential equations of the calculation are given here:

$$\text{Volume of vapour} \approx \text{volume of level rise - volume of melt,}$$

$$\text{volume of liquid} \approx \text{volume of interaction - volume of vapour - volume of melt.}$$

Note that the summands on the right hand side of equation one and the volume of interaction in equation two are all obtained from measurements.

One striking result is that the liquid fraction was very large during the initial period of time. The reason is that the melt release started as a shower of droplets producing a bowl-shaped interaction zone which included a relatively large amount of water between the droplets. In fact, the diameter of this zone at the actual height of the water surface was more than three times the nozzle diameter at time 0.1 s (Fig. 3.1).

The steam and melt fractions started from low levels. The steam fraction increased steadily, while the melt fraction decreased again, from about 0.15 s on, due to the fast increase of the interaction volume. The volume fractions of steam and liquid came closer together with time and take on values around 50% after 0.4 s.

The steep increase of the steam fraction starting at 0.27 s was obviously the result of a change in the boiling behaviour which suddenly became more violent. Evidence of this change is provided by the film pictures (compare the picture for 0.2 s with those of 0.3 s, 0.4 s, etc.), as well as by exponential increases in the pressure (Fig. 3.4), steam flow rate (Fig. 3.7), and water level (Fig. 3.8).

Since the radial extension of the interaction zone was essentially determined by the extent of jet fragmentation, one can conclude from the relative large liquid fraction which only gradually decreased, that a broad scatter of melt fragments existed at the periphery of the melt stream moving downwards. Melt fragments were temporarily seen to be carried upwards by the steam, thus contributing to an additional radial expansion in upper parts of the interaction zone.

As for the steam fraction, two conditions may have contributed to small initial values: 1. Steam produced during the initial time easily escaped from the pool, without contributing much to the water level rise. 2. The size of melt drops and fragments at the periphery were still large thus keeping steam production low. In fact, the film pictures (Fig. 3.1) taken after 0.1 s show the radial extension of the interaction zone took on values larger than the jet diameter by a factor of about five to six.

After about 0.5 s, as mentioned, average values are no longer representative of real distributions of the fractions. This is especially valid in the vicinity of the melt fragments. More information about the distribution of steam and liquid in the water pool can be gained from results given in the following section.

3.3.3 Local distributions of steam and water in the water pool

The series of graphs given in Fig. 3.14 illustrate the distribution of steam and water in the water pool for various times. The times have been chosen to present major stages in the progression of interaction. Note that the coordinates of the void sensors determine the grid; i.e., zero radius is not shown.

Steam is detected in test PM13 very early (0.02 s). The following expansion of the interaction zone in radial and axial directions as well as the variations of the steam and liquid fractions inside this zone can well be observed. Pictures No. five to nine (times 0.40 to 0.90 s) show coherent areas of large steam fractions. This result coincides with that of Fig. 3.13.

The approach to and arrival at the fragment catcher of the interaction zone correspond to the pictures at 0.80 to 1.10 s. After 1.1 s, the distribution of steam and water in the interaction zone varies in a wide range.

The advantage of the information given in Fig. 3.14 (compared to that of the family of curves shown in Fig. 3.11) is that light is shed on the phase conditions dominating locally and temporarily *inside* the boundary of the interaction zone. The information is valuable, although the conditions in a narrow section of the pool are concerned in Fig. 3.14.

3.3.4 Jet fragmentation

The probability that a thermocouple is hit and destroyed by the melt is large if a rather compact melt stream develops. It is low in case of melt stream fragmentation. Then, the drops may bypass the thermocouple because of the geometric and hydraulic conditions in the vicinity of the lances.

In PM13, the upper thermocouples were destroyed one after the other, down to the height of -1115 mm, while the ones located further down were not affected. This suggests that the jet break-up length was $1075 < L < 1275$ mm (L being the distance in water starting from the initial surface).

3.4 Progression of the steam-water mixture into the annular gas space

This section begins with the presentation and discussion of temperature and void measurements obtained from the gas space.

Temperatures measured at various heights are shown in Fig. 3.15. The T06 thermocouple located in the free-board volume at a distance of 25 mm from the vessel axis

was destroyed by melt at the time 0.55 s. The thermocouples mounted at larger heights in the annular gap were not affected.

The *void data* shown in Fig. 3.16 illustrate the conditions encountered in the gas space near the vessel wall. Signals of all void data have been used to evaluate the axial progression of the liquid in the annular compartment (Figs. 3.17 and 3.18).

The instants at which the very first "droplet" (typical duration: 0.001 – 0.002 s) and the first "slug" (duration ≥ 0.010 s), respectively, appeared in the signals were determined for each measuring level. The two data files thus obtained have been entered in Fig. 3.17 together with the average water level data. The difference in time of the "first drop" line and the water level line gives the quantity of lead of water droplets relative to the overall rise of the water level. Extrapolation of the "drop" and "slug" lines may give an approximate time at which a marked number of water drops could have entered the steam venting pipes for the first time.

First changes from steam to liquid in all void signals have been used to construct the lines drawn in Fig. 3.18. The curves show that the advance versus height of the water drops occurred rather evenly.

The distribution of steam and water in the annular compartment is given in Figs. 3.19a and 3.19b for various times. The pictures show that, after the passage of the first drops, water was concentrated mostly in the zone close to the vessel wall.

3.5 Post test investigation

3.5.1 Water mass balance

The water level decreased by 605 mm during the test. This length corresponds to a volume of 220 litres. A volume of 80 litres of water was found in the water separators, a maximum of 40 litres could have been evaporated by 23.8 kg of alumina melt (estimation, considering normal conditions for the water and the melt enthalpy above 372 K). The difference, 100 litres, must have been transported as droplets with the steam through the venting lines. In fact, the film of the video camera, that was directed to the end of one of the venting lines, shows water draining out of the tube exit. Unfortunately, no quantitative result can be given. Stochastic scatter in two of the flow meter signals (Fig. 3.7) indicate that the steam was temporarily interspearsed with water slugs.

3.5.2 Melt balance and sieve analysis

Results of the sieve analysis are given in Table 3.1. It is remarkable that more fragments were found at the bottom of the test vessel than inside the fragment catcher. The films show that violent boiling in the region above the fragment catcher caused sweep-out of fragments from it. Evidence of this process, which presumably took place late in the course of the test, is given by the radial profile of fragment agglomeration found at the bottom of the vessel.

The total mass of melt collected after the test was somewhat larger than intended. The post-test particle size distribution of the melt fragments is shown in Fig. 3.20.

3.5.3 Chemical analysis

Table 3.2 shows the results of the chemical analysis. The numbers for the materials are mass-weighted averages for magnetic and nonmagnetic material, respectively, for the various locations where material was found after the test.

Table 3.1 PM13, sieve analysis of fragments broken down in the sites of recovery

Location	Quantity		Magnetic fraction	Non-magnetic fraction	Total
Water separators	Mass	g	2077	1973	4050
	Mass mean diam.	mm	-	-	3.05
	Sauter mean diam.	mm	1.43	1.20	-
	Total surface	m^2	2.35	3.40	5.75
Fragment catcher	Mass	g	1978	3062	5040
	Mass mean diam.	mm	-	-	12.26
	Sauter mean diam.	mm	5.60	10.14	-
	Total surface	m^2	0.42	0.62	1.04
Basis of test vessel	Mass	g	7025	7668	14693
	Mass mean diam.	mm	-	-	11.17
	Sauter mean diam.	mm	6.15	7.22	-
	Total surface	m^2	1.86	2.19	4.05
Total	Mass	g	11080	12703	23783
	Mass mean diam.	mm	-	-	9.91
	Sauter mean diam.	mm	5.17	6.99	-
	Total surface	m^2	4.63	6.21	10.84

Tab. 3.2 PM13. Chemical analysis of melt fragments

Location	Material collected g	Material analysed g	Metal (iron) %	Oxide (total) %	Al_2O_3 %	Fe_2O_3 %	MgO %	Other Oxides %
Water separator	4050	762.4	5.55	94.45	88.2	8.4	0.41	3.00
Fragm. catcher	5040	1024.4	11.05	88.95	89.2	8.1	<0.1	2.60
Bottom of facility	14693	4314.8	11.95	88.05	90.0	7.62	<0.1	2.20
total/ average	23783	6101.6	10.67	89.33	89.6	7.9	0.1	2.4

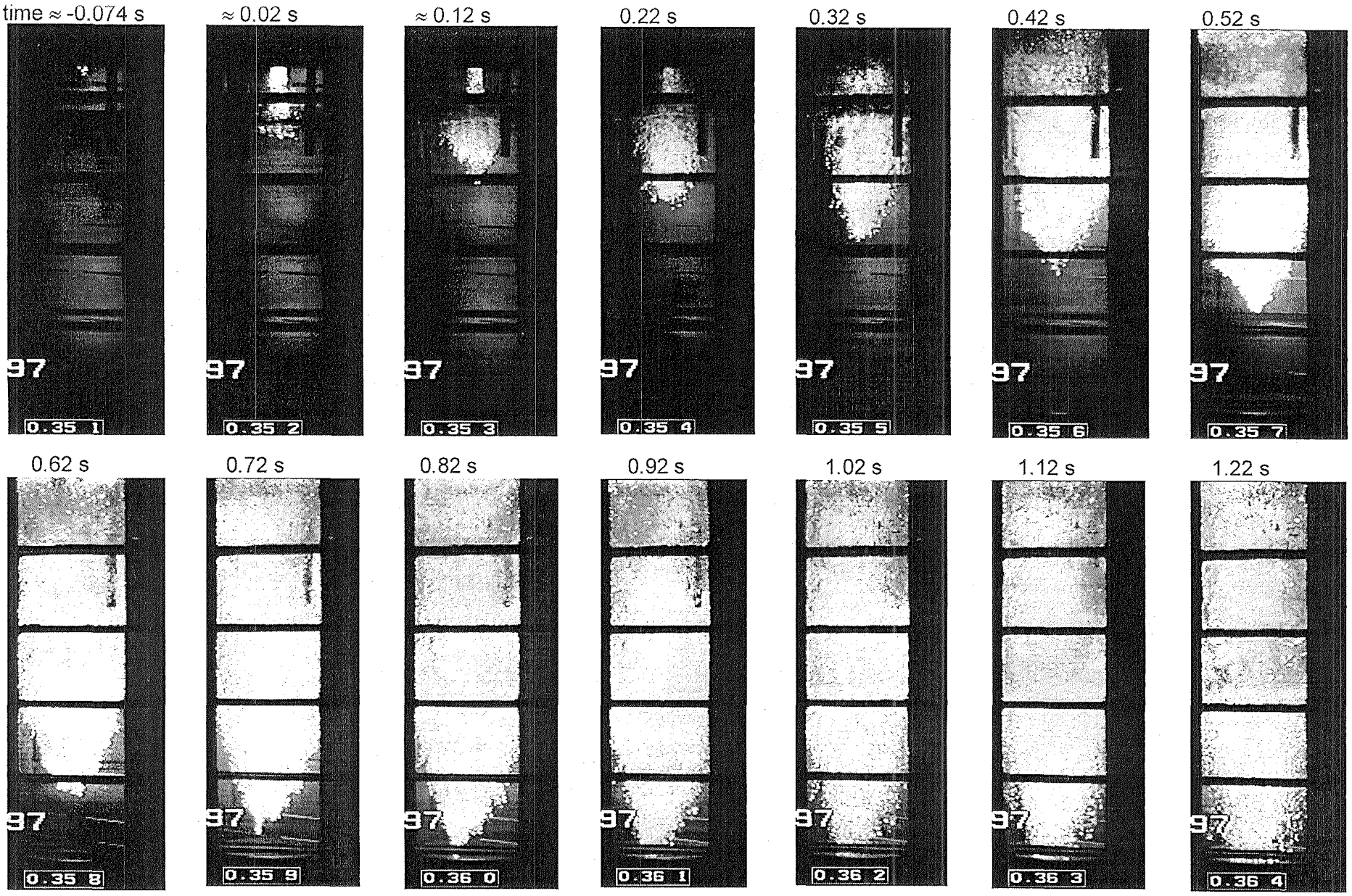

Fig. 3.1 Development of the interaction zone in PM13 shown by selected pictures of the video film.

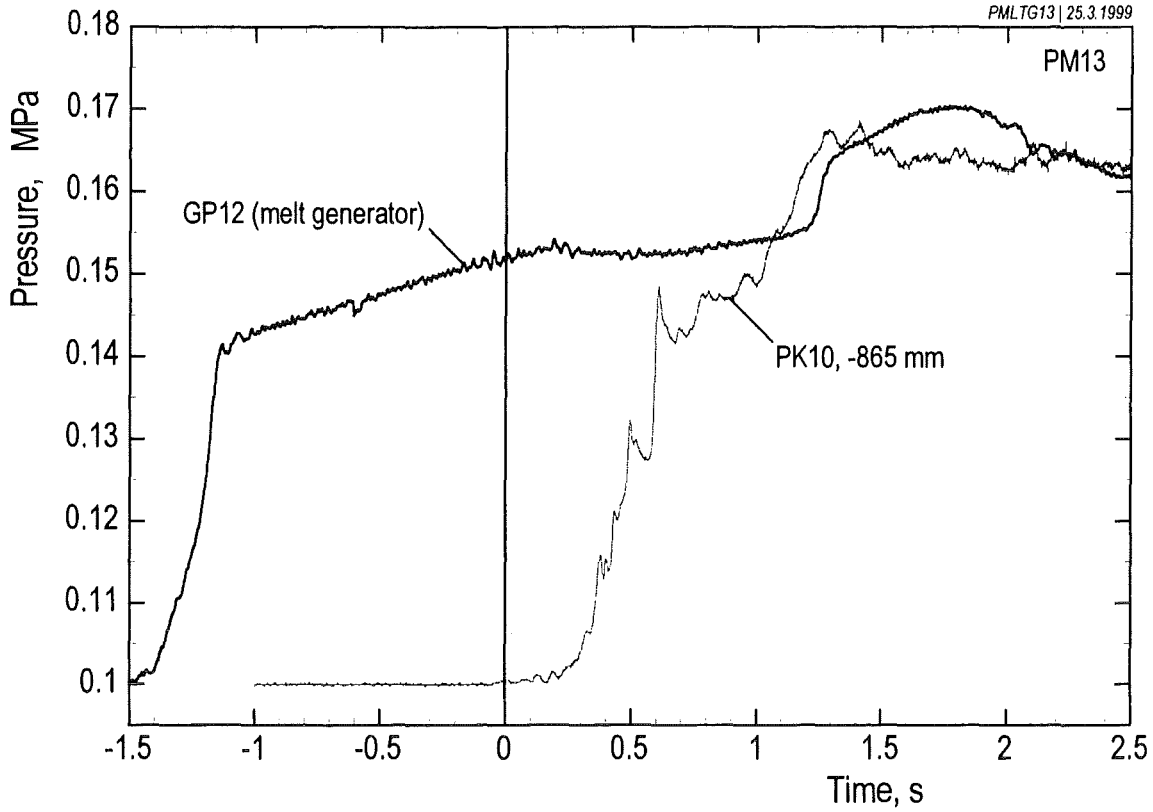

Fig. 3.2 Pressure data obtained inside and outside of the melt generator.

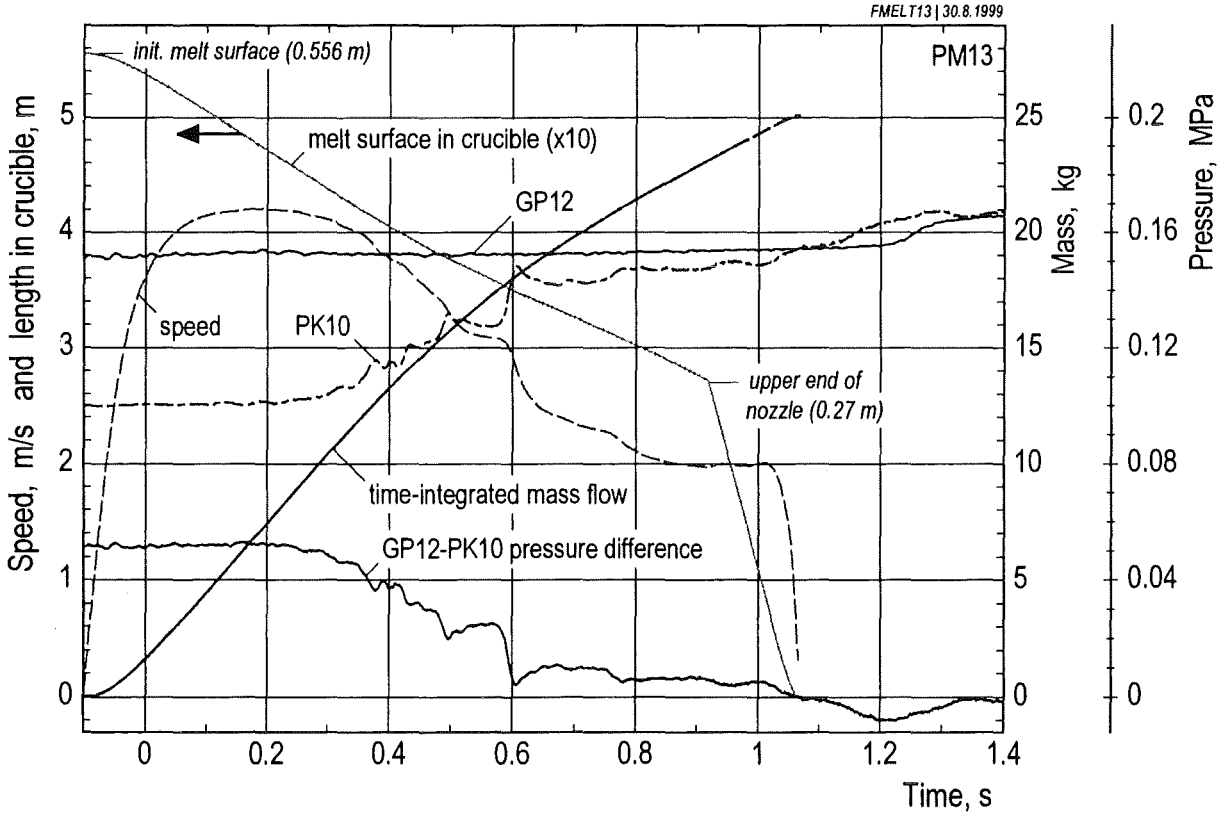

Fig. 3.3 Melt release calculated on basis of the pressure difference. The calculation started at the time estimated for steel membrane break (-0.1 s). The length in crucible is related to the lower end of the nozzle.

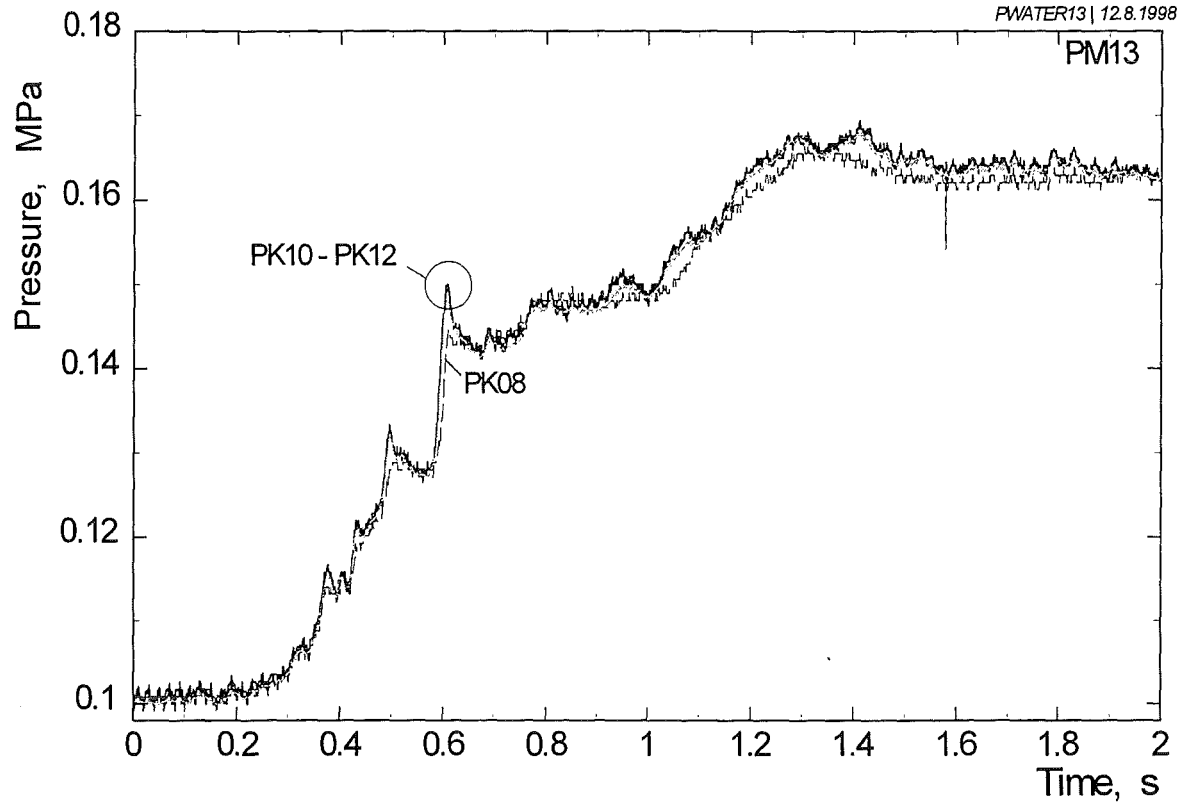

Fig. 3.4 Pressure data obtained from gauges located in the water pool.

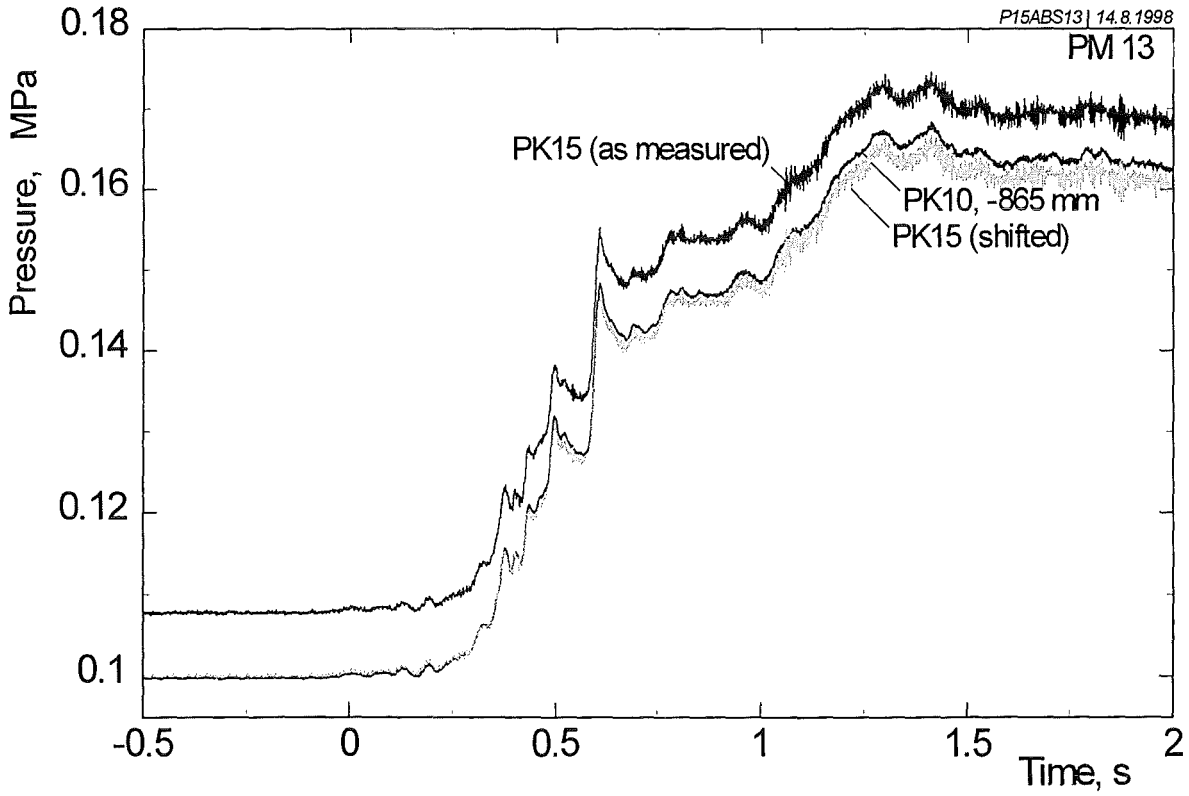

Fig. 3.5 Comparison of the PK15 absolute pressure data obtained in the water at –815 mm height with the PK10 dynamic pressure data.

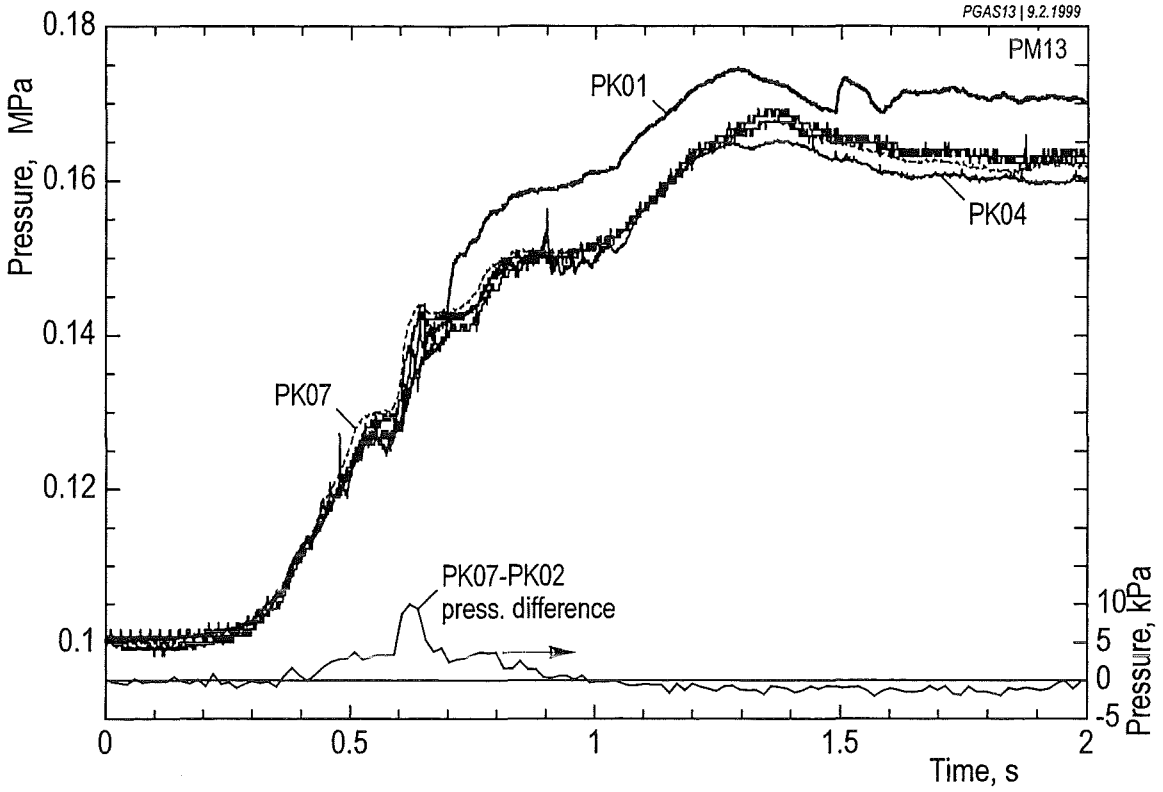

Fig. 3.6 Pressure data obtained from transducers located in the gas space (PK01-PK04) and at a distance of 25 mm below the initial water level (PK07).

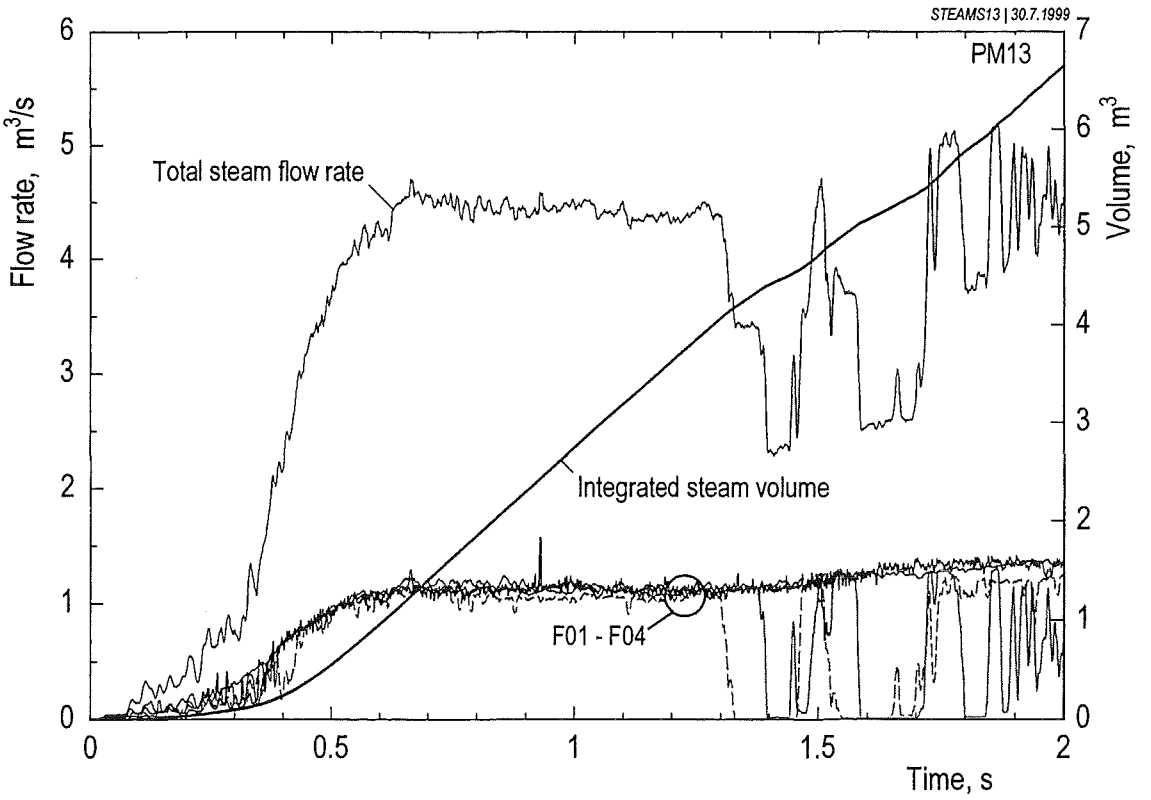

Fig. 3.7 Steam flow rates and the time-integrated steam volume.

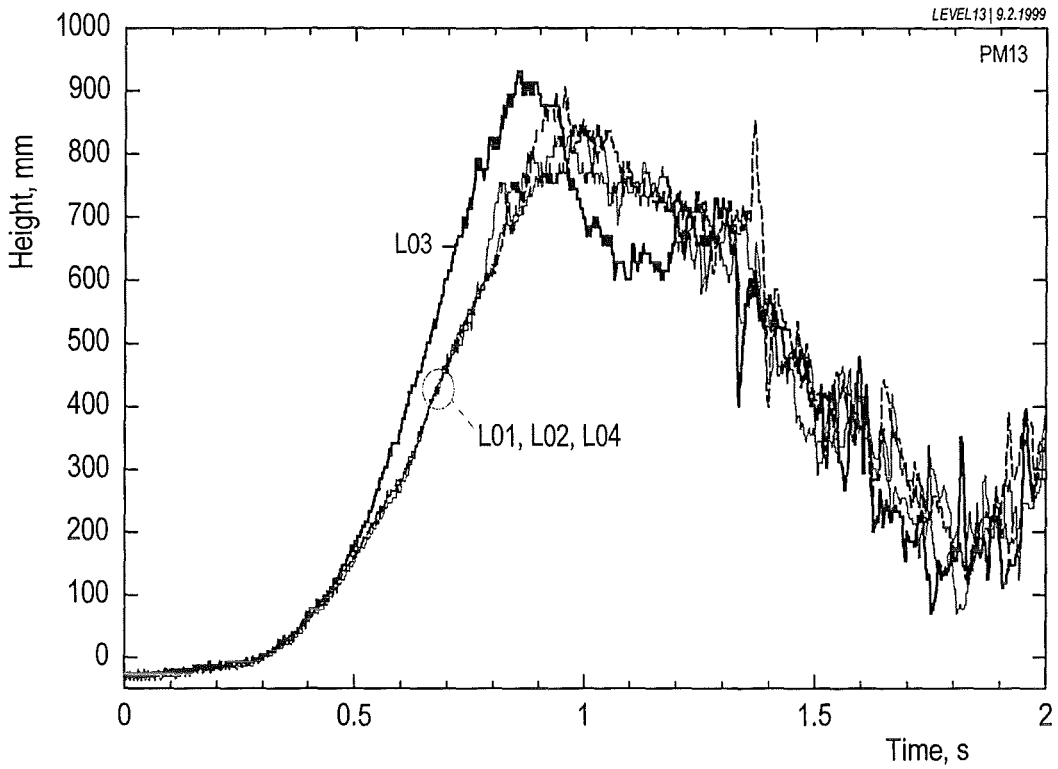

Fig. 3.8 Data of the four level measurements

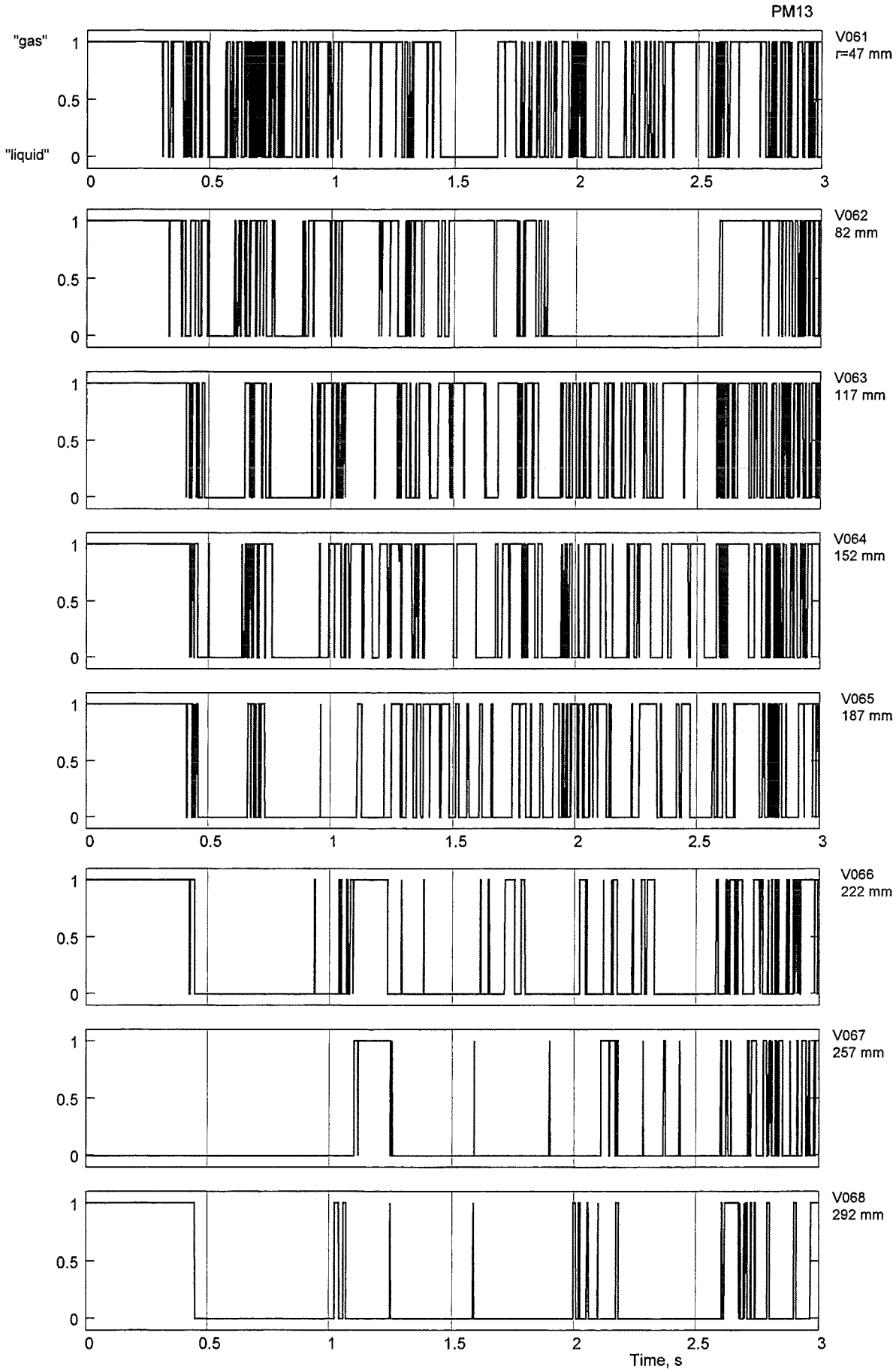

Fig. 3.9 (a) Void signals from the V06 lance (96 mm above init. water level).

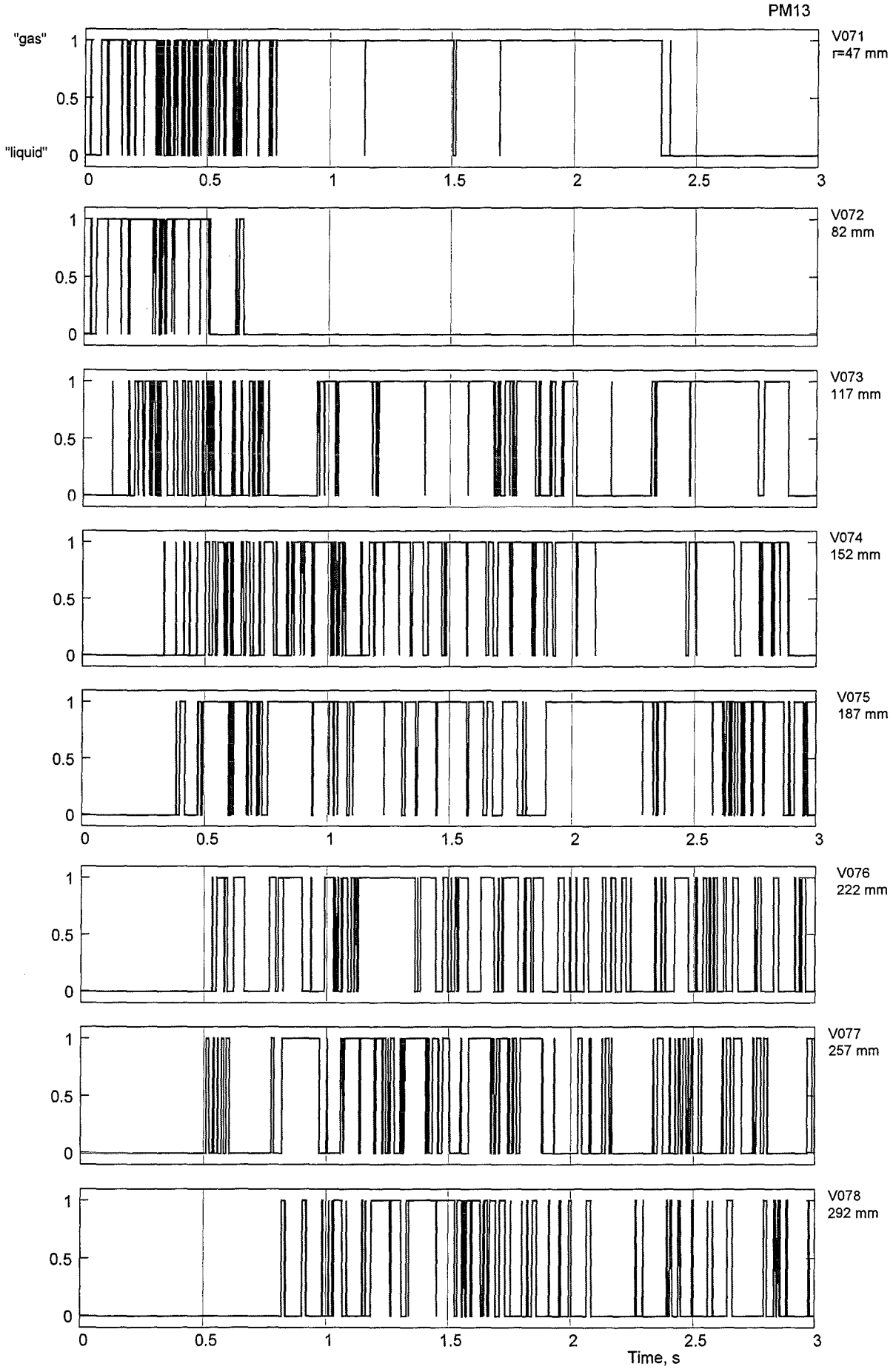

Fig. 3.9 (b) Void signals from the V07 lance (67 mm below init. water level).

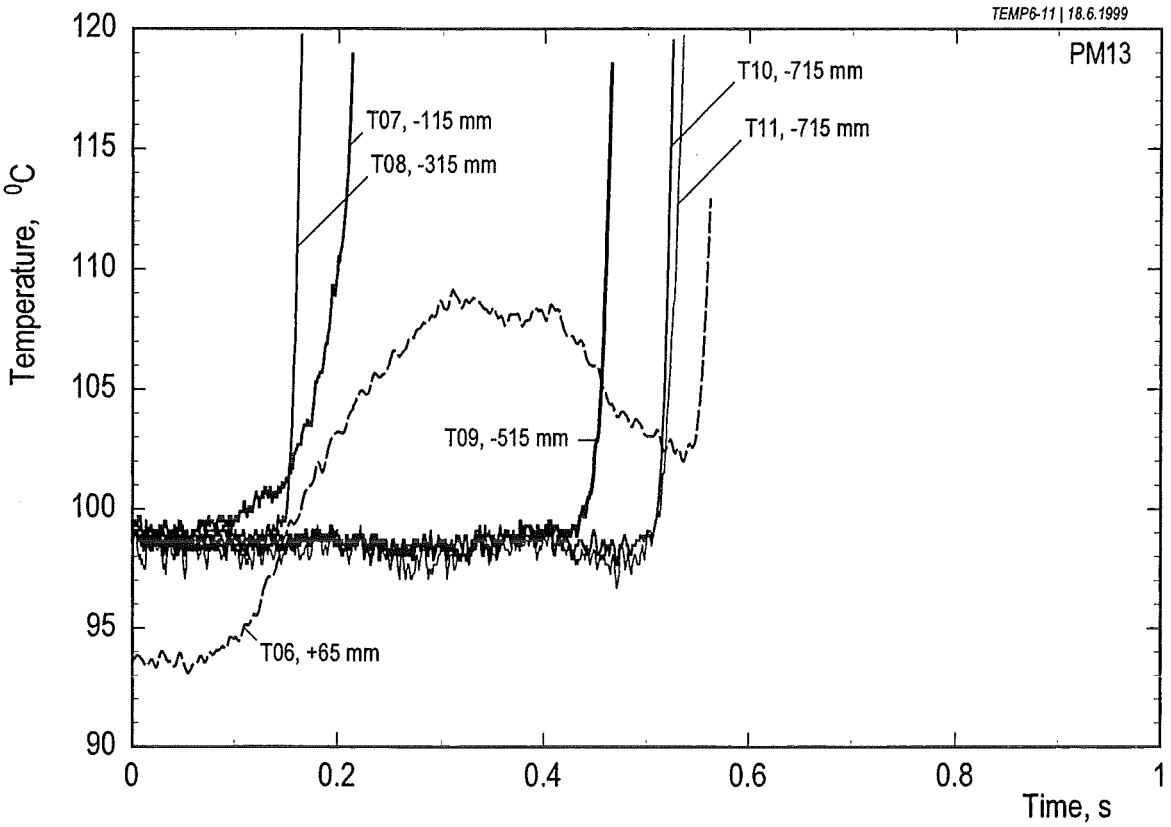

(a) upper part of the water pool

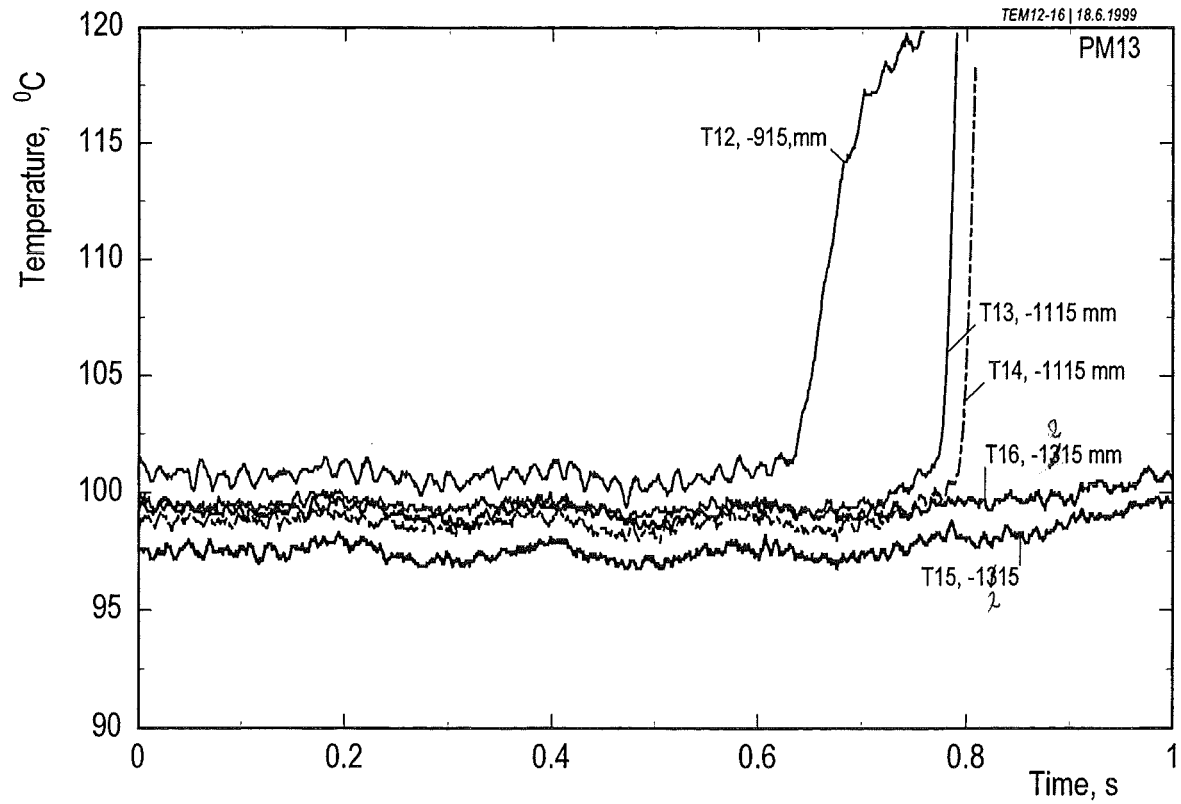

(b) lower part of the water pool

Fig. 3.10 Temperatures measured in the water pool (T07-T16) The T06 data also shown (a) are obtained a short distance above the initial water level.

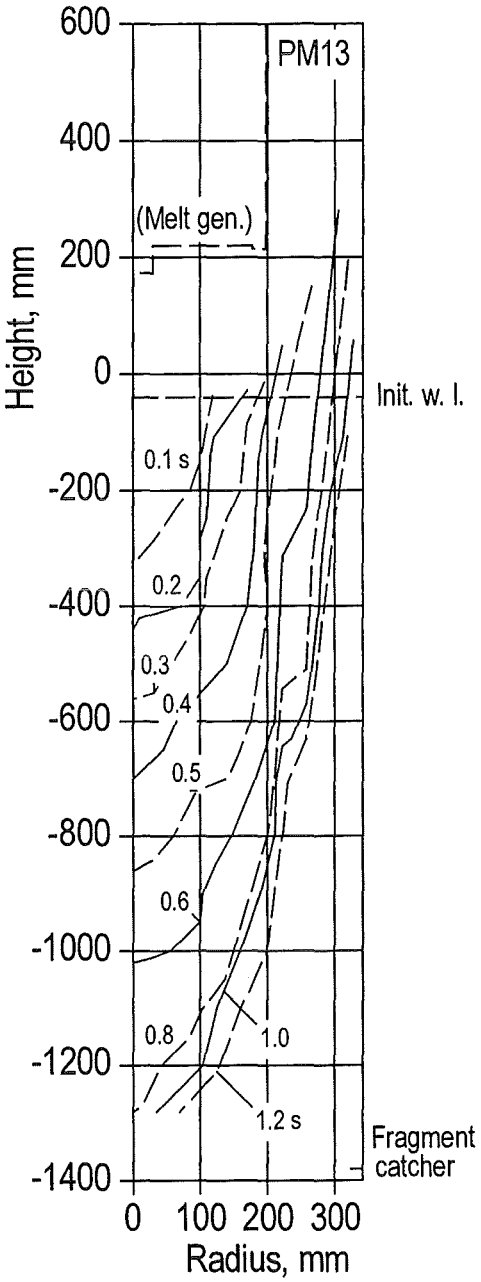

Fig. 3.11 Progression of the interaction zone into the water with the time as a parameter

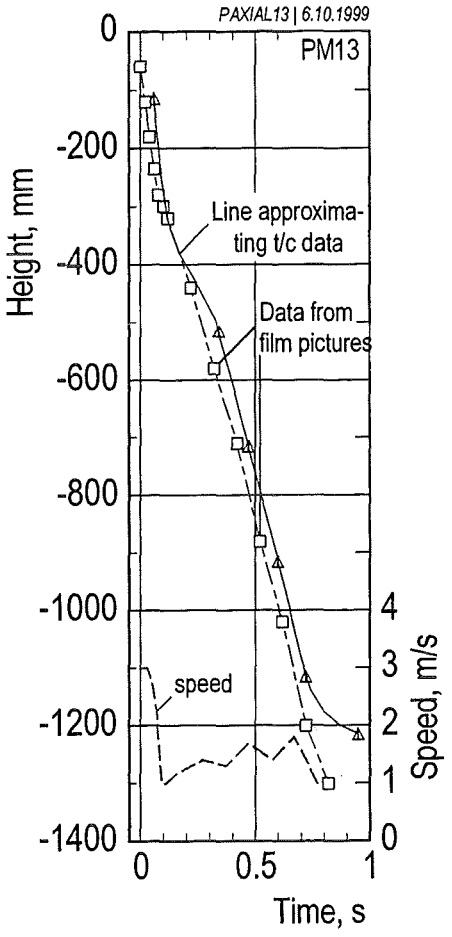

Fig. 3.12 Progression of the interaction zone in the centre of the pool. The speed is derived from the film data.

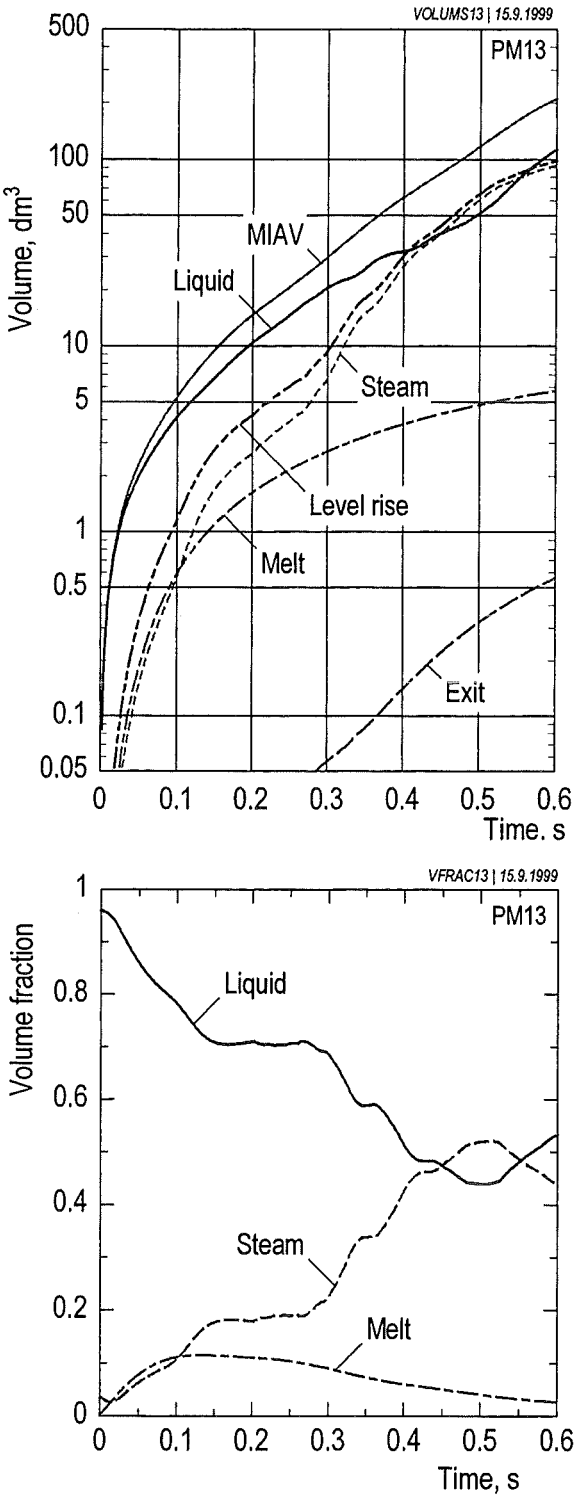

Fig. 3.13 Volumes resulting from the interaction (MIAV=multiphase interaction volume; Exit= volume of the evaporated part of water; volume due to level increase) and partial volumes of the interaction zone (steam, liquid, and melt) are shown on top, average volume fractions of the three components inside the interaction zone at the bottom.

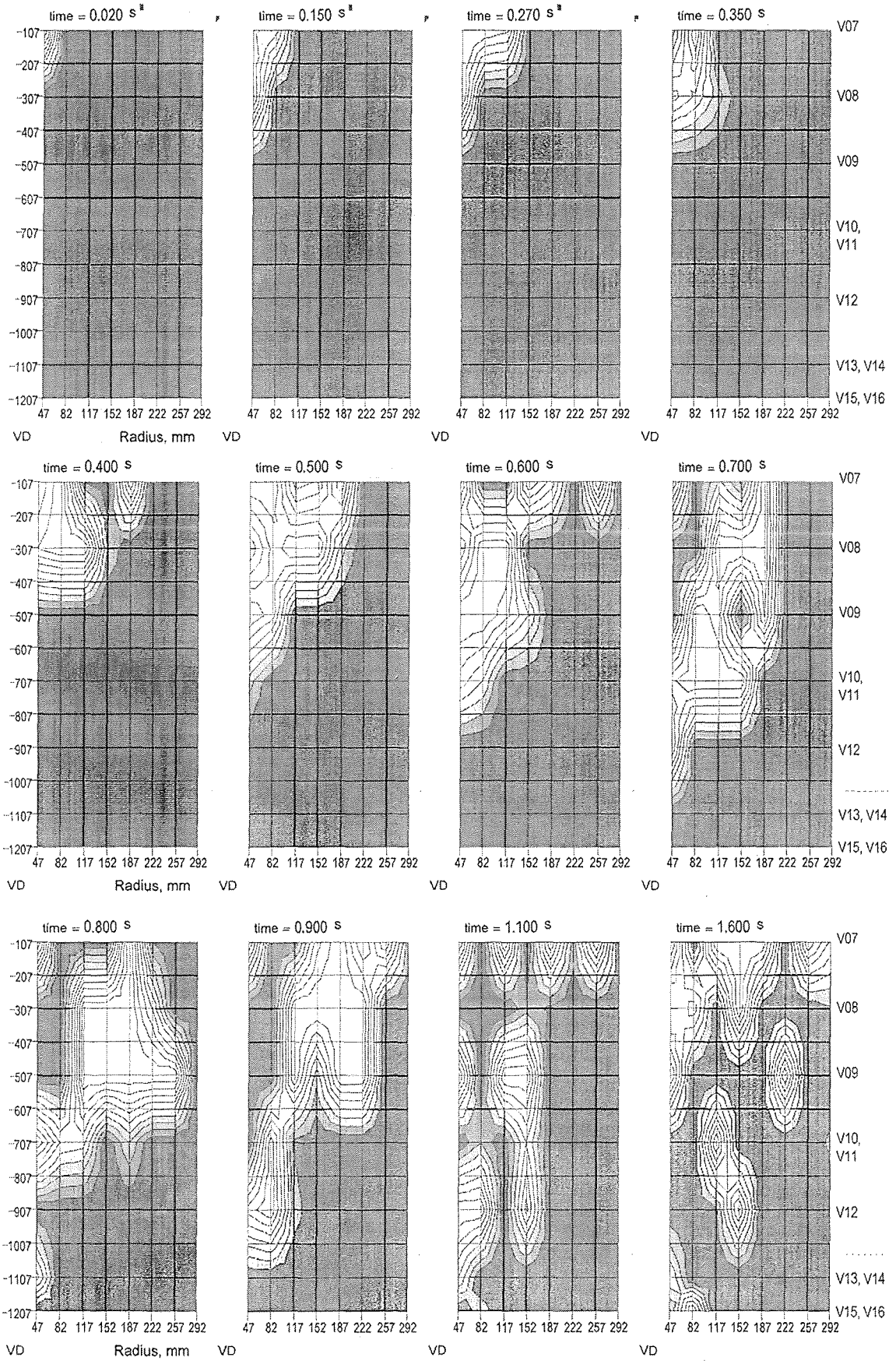

Fig. 3.14 Distribution of steam and water in the water pool in PM13 at various times (white area=100% steam; dark =100% water). Distance between fraction lines: 0.125

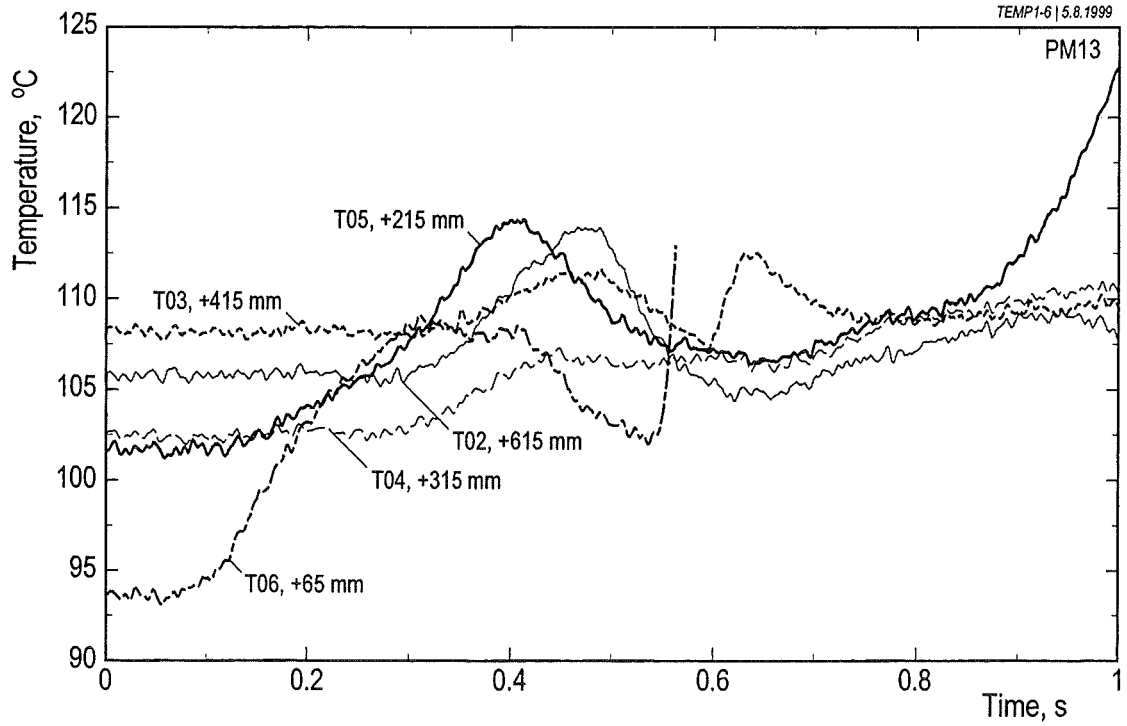

Fig. 3.15 Temperatures measured in the freeboard volume (T06) and in the annular gas compartment.

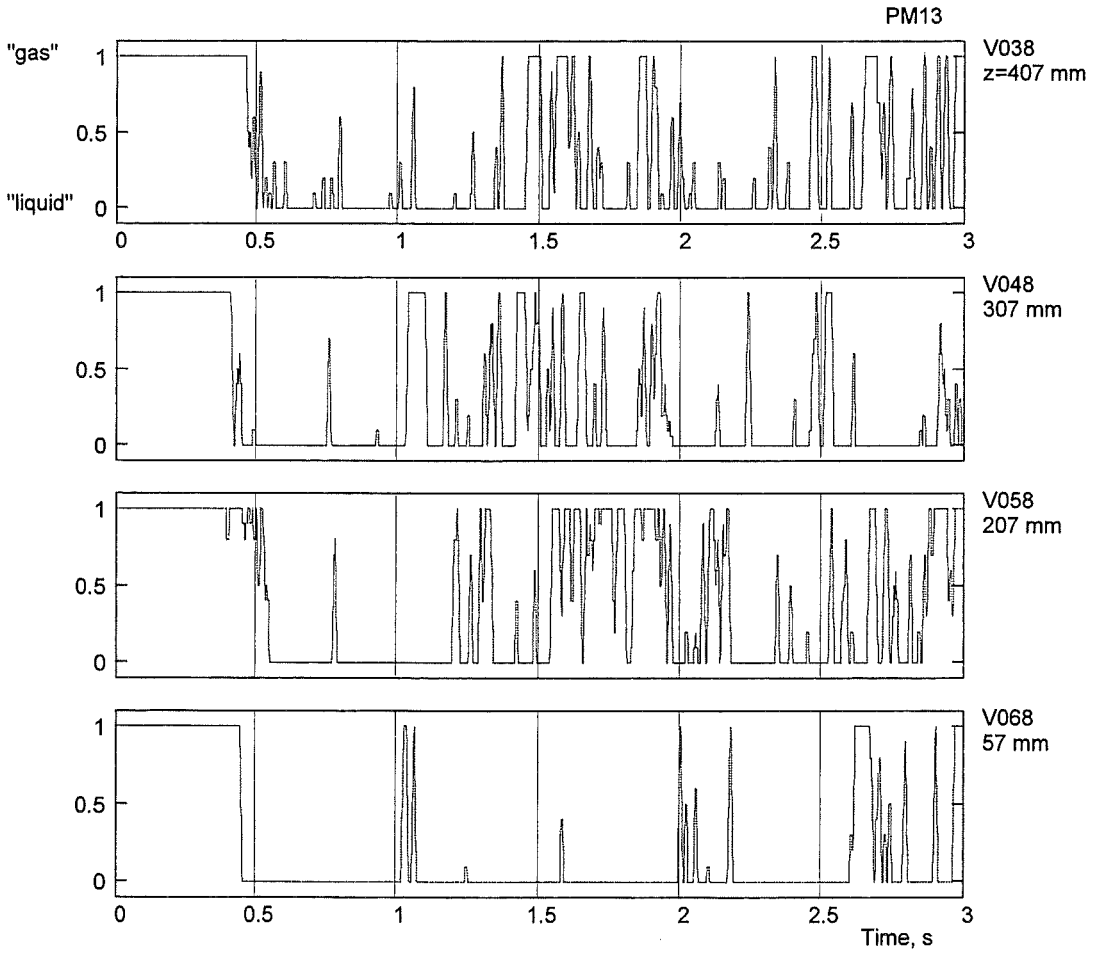

Fig. 3.16 Void signals obtained from the freeboard volume (V06) and the annular gas compartment at various heights. Smoothed signals (cf. Fig. 2.6) have been chosen to get a better time resolution. The measuring tips were close to the test vessel wall.

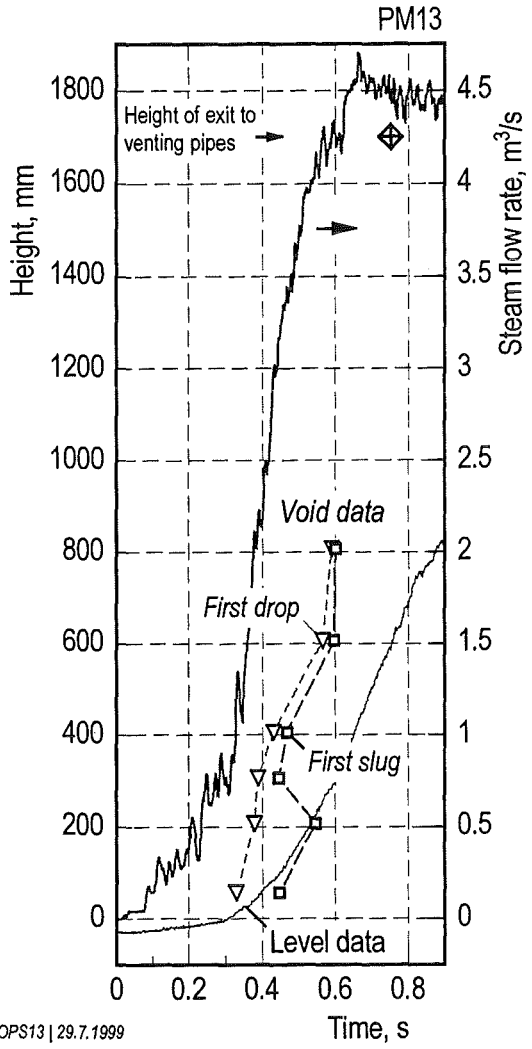

Fig. 3.17 Penetration of water into the annular compartment versus time compared with rise of the water. The steam flow rate is also shown.

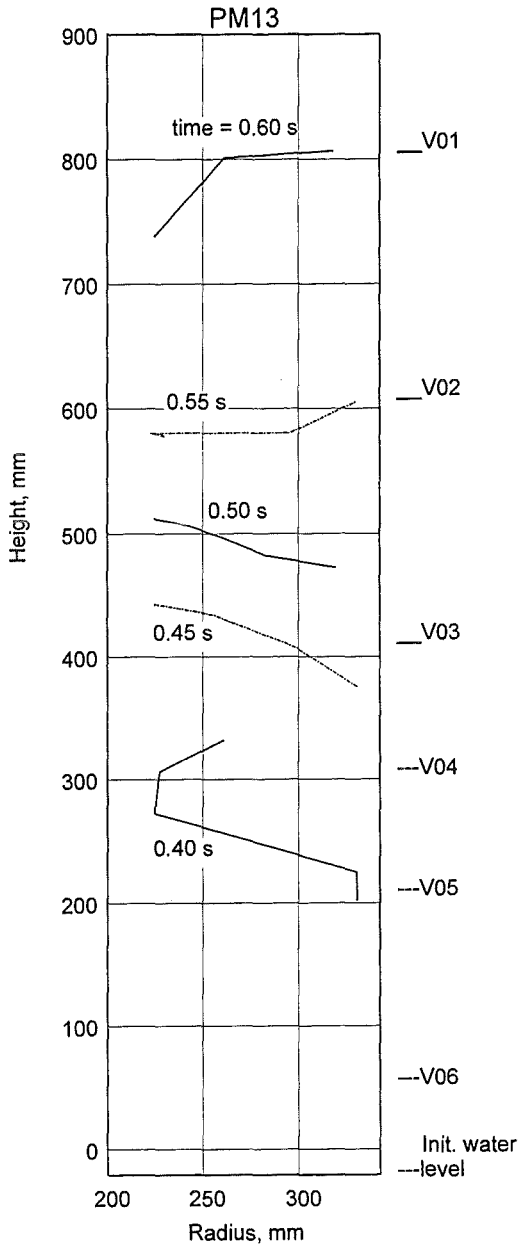

Fig. 3.18: Progression of the water drop front into the annular gas compartment shown with the time as a parameter.

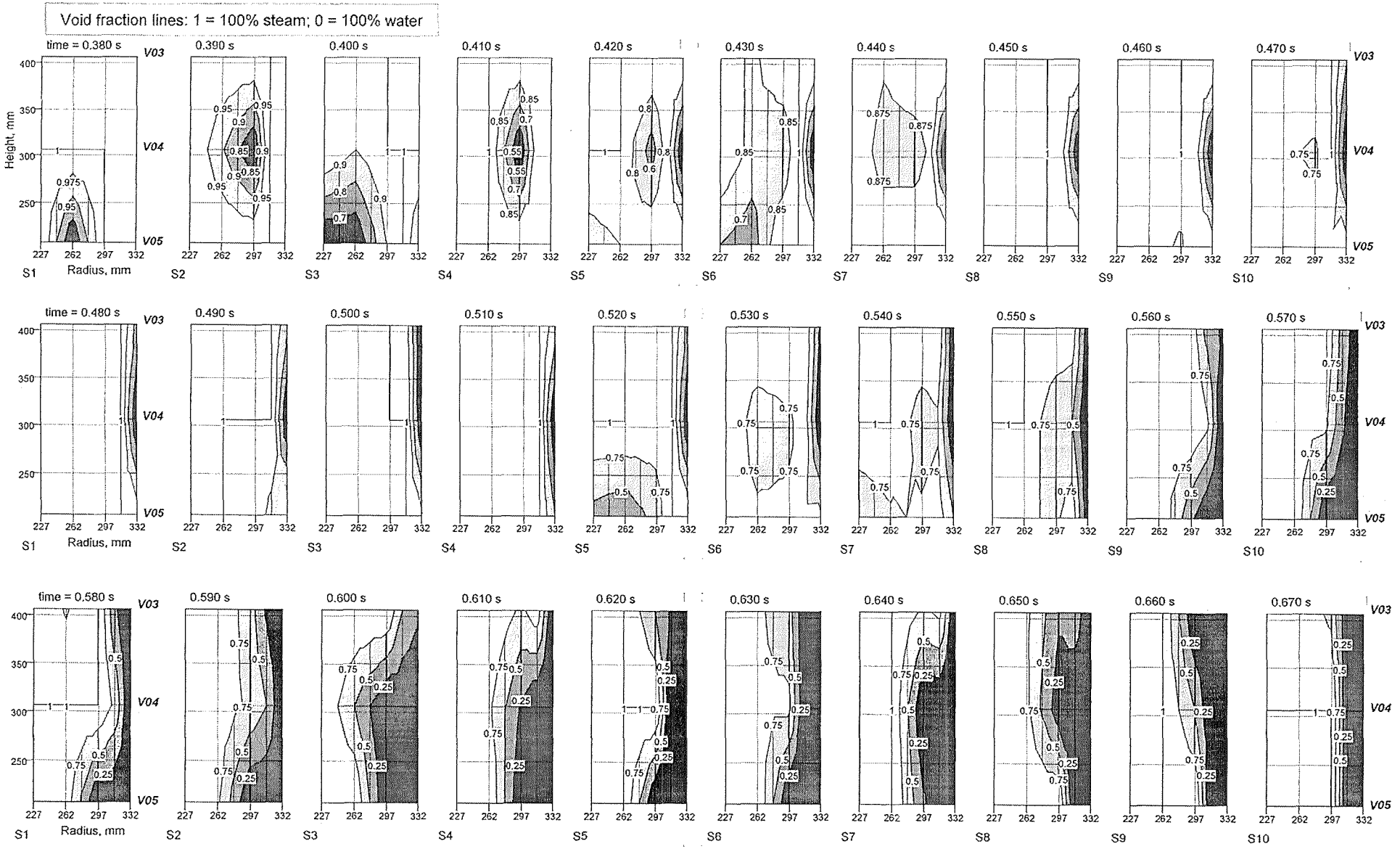

Fig. 3.19 (a) PM13. Distribution of steam (gas) and water across the annular gas compartment between 207 and 407 mm height evaluated from void data. The times between the pictures is 0.01 s.

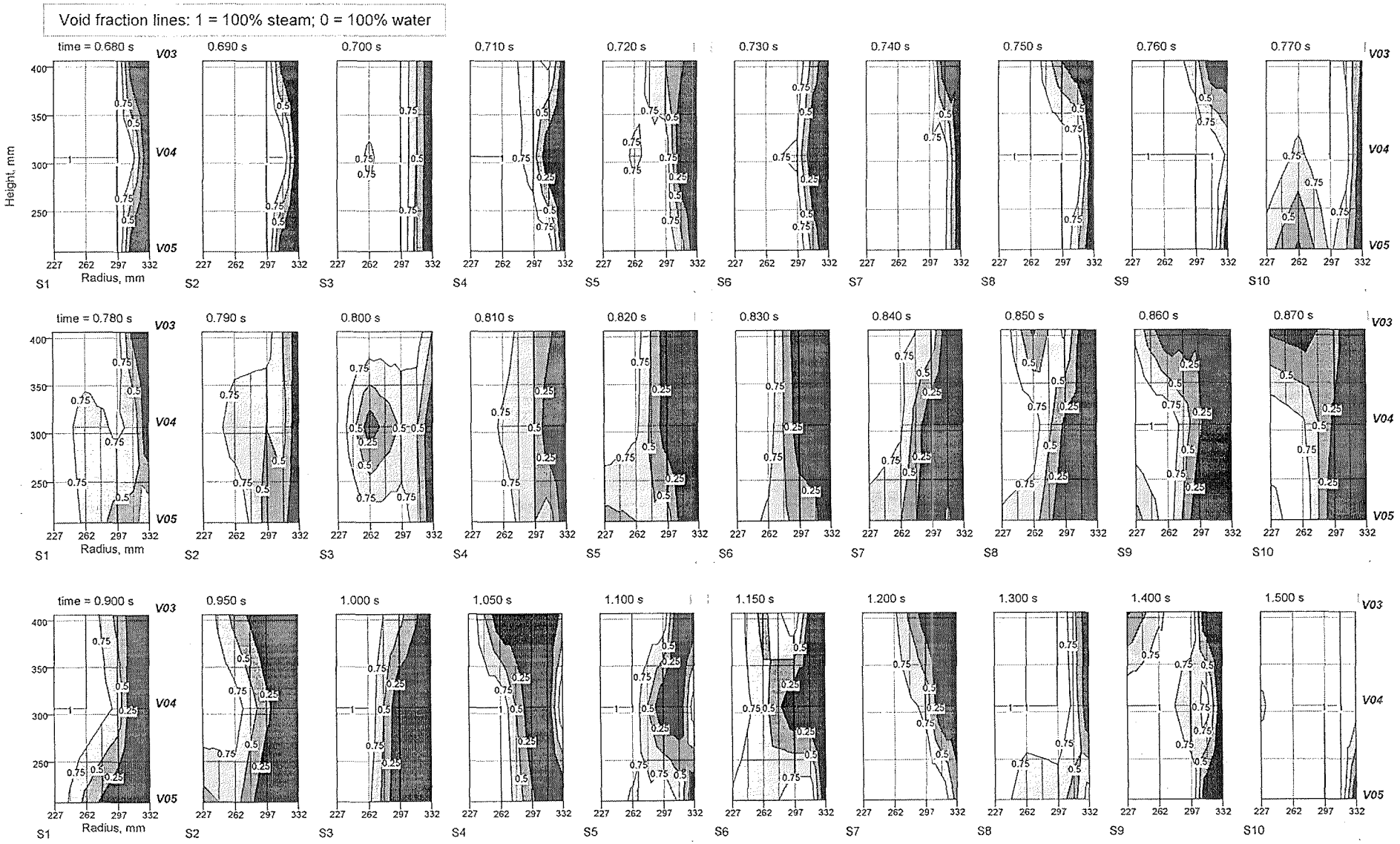

Fig. 3.19 (b) PM13. Distribution of steam (gas) and water across the annular gas compartment between 207 and 407 mm height. (The time step between the pictures has been increased in the lowermost line).

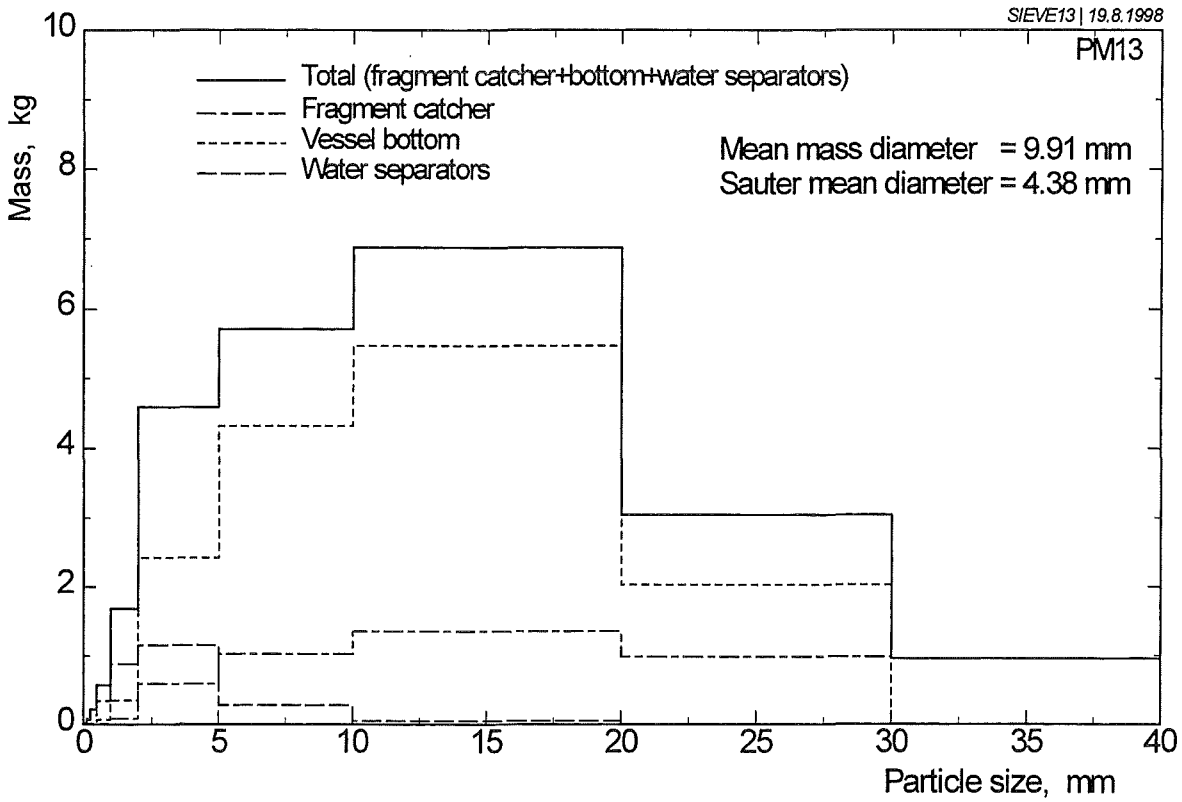

Fig. 3.20 Post-test particle size distribution of the melt fragments

4 RESULTS OF PM14

4.1 General course of the experiment

Figures 4.1 and 4.2 give sequences of pictures obtained from a video film and from a high-speed film, respectively. The very first melt release occurred as droplets, while the first melt droplet appeared at the nozzle end at time -0.049 s. The droplets moved at an average speed of 4.0 m/s. The following melt release was more coherent and the contour of the jet was almost cylindrical. The average speed of melt between nozzle end and water surface, evaluated from the films, was 3.5 m/s. As in PM13, on leaving the nozzle, the jet rolled somewhat around the vertical line and the melt stream seemed to consist of melt and gas in equal shares.

Initially, the leading edge of the melt proceeded fast into the water. The speed slowed down continuously until, at time 0.270 s, the height of -700 mm was reached. After that time, the penetration speed increased again (for further details see Section 4.3.1). This acceleration was driven by an upstream portion of melt that moved faster in the centre of the interaction zone and finally overtook the leading front. The fragment catcher was reached by the melt at about 0.720 s.

4.2 Pressure, steam flow, and level measurements

Estimation of the melt release function from pressure data The evolution of pressure measured inside and outside of the melt generator is shown in Fig. 4.3. (The scatter recorded at times less than -2 s is attributed to a reaction of the melt with a small amount of adhesive used in the construction of the crucible which did not much influence the test results).

The test procedure and course of events were similar to those in PM13: The GP12 pressure in the melt generator was increased as intended in one step starting at time -1.8 s. The increase starting at -1.5 s was due to heating of the crucible gas atmosphere by the melt. As soon as melt release started (around time zero), the pressure in the melt generator decreased a little. A shallow relative minimum followed which turned into a steep rise at 1.05 s. Equilibrium between the GP12 pressure and the pressure in the interaction zone (at time 0.84 s) and the steep rise in the GP12 pressure mentioned, indicate that the crucible and nozzle tube became empty during that time.

The results of the calculation, performed in a similar way as described in test PM13, are shown in Fig. 4.4: the melt speed, integrated melt flow, and the movement of the

melt surface. The calculation was started at -0.1 s (estimated break of the membrane) and stopped at 0.9 s, which is about the time when the pressure difference became zero. The integrated melt flow rate reached the given mass, 23.2 kg, a little earlier, i.e. when the melt surface arrived at the height of the membrane (0.182 m). It should be noted that the pressure difference, which was larger than in PM13 from the beginning, resulted in a larger speed in the initial period.

Pressures below the initial water level are shown in Fig. 4.5. The first significant pressure rise occurred 0.130 s after the first melt-water contact. At that time, the leading front of the interaction zone had already penetrated a distance of 320 mm into the water. Like in PM13, the pressure rise occurred oscillatory.

Pressures in the gas space are given in Fig. 4.6. Comparison with one of the pressures obtained in the water pool is made in Fig. 4.7. The first significant pressure rise in the gas space (Fig. 4.6) occurred at time 0.150 s. Further increases occurred oscillatory, as mentioned. The pressure traces show, with one exception (PK01), almost uniform behaviour until the maximum (0.183 MPa) was reached at 1.2 s.

It appears from Fig. 4.7 that the oscillations in PK02 were increasingly delayed relative to PK08. The increased delay and the resulting pressure differences are regarded as an indication of a change in the steam flow pattern with time: An increase in the liquid fraction would lead to a decrease in the propagation speed as well as to an increase in the friction losses as shown in the next but one paragraph (*Pressure drop across ...*).

Steam flow rate Figure 4.8 shows the F01 - F04 steam flow measurements, the sum of the steam volume rates, and the integrated volume. A marked rise in the steam flow rate occurred around 0.1 s, the first maximum was reached at 0.6 s. Comparison with pressure traces (Fig. 4.5) shows that from that time on the pressure continued to increase, while the steam flow rate did not. Fluctuations in the F01 and F04 signals (between 1.1 and 2.1 s) caused a corresponding scatter of the total steam flow rate. Later on, more frequent signal drops led to a gradual reduction in the total steam flow rate.

An estimate helps to get an idea of the efficiency of evaporation: The integrated steam rate amounted to a volume of 19.3 m^3 after eight seconds. This volume corresponds to a water mass of 11.6 kg, that is only 26% of the mass that could have been evaporated by the melt enthalpy.

Pressure drop across the steam venting pipes The characteristics of the steam flow path (including steam venting pipe no 3) have been obtained by calculating pressure loss coefficients. The calculation was based on histories of pressure differences and on the F03 flow rate, respectively. Before discussing the results (Figs. 4.9 and 4.10) a few definitions are given:

- The ζ_{P1} and ζ_{P2} coefficients were calculated using the difference in pressure of the PK01 and PK02 data relative to the environment.
- The P5-6 coefficient represents the loss across the water separator.
- The P6-3 coefficient represents the loss in the tube between water separator and flow meter.

Figure 4.9 shows that the largest loss occurred at the inlet to the venting pipes. The signal spikes around time 0.2 s are due to random steam flow variations while the pressure is still low. Figure 4.10 gives the PK01 coefficient together with the steam flow rate and the pressure drop in a larger time scale. It is shown that the first increase in the loss coefficient was due to the steep increase in the flow rate. After short term halts, both the pressure and the loss coefficient further increased whereas the flow rate slowed down. We conclude that this result is due to a change in the steam flow pattern, i.e. an increasing fraction of water droplets.

Change of the water level The first substantial increase took place at the time 0.150 s (Fig. 4.11). A characteristic of the level time history, until the first maximum at 0.75 s, are two periods with different rates of increase. Details are discussed below.

4.3 Development of the interaction zone in the water

Data base: void and temperature measurements Two selected sets of void signals are presented in Figs. 4.12 (a) and (b). The temperature signals are given in Fig. 4.13. The remarks made at the beginning of Section 3.3, dedicated to PM13, should also be considered here. The behaviour of some of the thermocouples is discussed in the next paragraph.

4.3.1 Progression of the steam/liquid interface

Figure 4.14 illustrates the progression of the interaction zone into the water obtained on basis of void data and film picture evaluation. The procedure was the same as for PM13 (Section 3.3.1) and the result is rather similar: The melt penetration produced a relatively narrow channel composed of melt, steam, and water particles.

Figure 4.15 gives the speed of axial progression derived from thermocouple data as well as from film pictures. The advance of the film data is due to the conical shape of melt penetration (see Fig. 4.1) along with the offset of the t/c tip from the vessel axis. The maximum in the speed of penetration, about 3.9 m/s, occurred in the very beginning. Afterwards, the speed was very much reduced until, around 0.5 s, penetration is accelerated again a little. Comparing Fig. 4.15 with Fig. 3.12, one finds the speed of axial penetration was larger in PM14 than in PM13.

In this context, it is interesting to point to a specific agreement between findings made in the films and in measurements: The obvious finding from the film picture taken at 0.6 s (Fig. 4.1), that the leading edge of the melt stream locally and temporarily deviated somewhat from the vessel centreline is confirmed by the non-symmetrical behaviour of two pairs of thermocouples (Fig. 4.13, T13 - T16).

The T13 and T14 thermocouples located at -1115 mm height indicated the passage of the vapour/liquid interface with a time difference of 0.2 s shortly after 0.6 s. After showing steam temperatures for another 0.25 s, both thermocouples were destroyed. On the other hand, 100 mm further down, the T16 thermocouple, located below T14 at the same azimuthal position, suffered from almost immediate destruction (the local axial speed of interface is calculated to be 4.6 m/s), while the T15 thermocouple was destroyed 0.13 s after T16.

4.3.2 Volumes and average volume fractions resulting from the interaction

The volumes formed as a consequence of the interaction are shown in the upper part of Fig. 4.16, average volume fractions of the three components within the interaction zone are drawn in the bottom part. The large penetration rate already stated is mirrored in the fast increase in interaction volume.

As in PM13, the steam and melt fractions started from low values and the liquid fraction was large initially. The steam and liquid fractions came together earlier than in PM13, while the steam fraction took on markedly larger values than the liquid fraction after 0.2 s. The very steep increase of the steam fraction at 0.2 s was, like in PM13, the result of a marked increase in boiling intensity. The increase is accompanied by just such ones in the pressure (Fig. 4.5), steam flow rate (Fig. 4.8), and water level (Fig. 4.11).

4.3.3 Local distributions of steam and water in the water pool

The sequence of graphs given in Fig. 4.17 shows the distribution of steam and water in the interaction zone for various times. The times have been chosen, as in PM13 (see Fig. 3.14), to present major stages in the progression of the interaction zone. Pictures No. five to eight (times 0.23 to 0.6 s) show coherent areas of large steam fractions. This result coincides with that of Fig. 4.16. After 0.8 seconds, the distribution of steam and water in the zone observed varies in a wide range.

4.3.4 Jet fragmentation

In PM14, the thermocouples in the pool were destroyed down to the height of –1215 mm, which is 45 mm above the rim of the fragment catcher (–1260 mm). This suggests that the jet break-up length exceeded the initial water depth.

4.4 Progression of the steam-water mixture into the annular gas space

The section starts with the presentation and discussion of temperature and void data obtained from this area.

Figure 4.18 shows time histories of *temperatures*. The T06 thermocouple located in the free-board volume at a distance of 25 mm from the centre, was soon destroyed by melt after 0.03 s. The other thermocouples mounted in the annulus at larger heights were not affected. A couple of *void data* (Fig. 4.19) illustrate the conditions encountered in a zone near the vessel wall.

The axial progression of water is drawn in Figs. 4.20 and 4.21. The lead of the water droplets relative to the rise of the water level was larger than in PM13 which was due to faster increase of the steam flow rate. Approximate extrapolation of the "first drop" and "slug" lines gives a time between 0.6 and 0.8 s at which a marked number of water drops could have entered the steam venting pipes for the first time.

The advance of the water drop front with the height (Fig. 4.21) was different from that in PM13 (Fig. 3.18). In PM14, it occurred at a larger speed in the zone close to the vessel wall (larger radius) than in the zone close to the melt generator case. This result can be explained by the larger increase of the steam production rate in PM14 during the time 0.1 to 0.4 s (see Section 6.2 below).

The distribution of steam and water in the annular gap given in Fig. 4.22 for various times also shows that water was concentrated mostly in the zone close to the wall where it preferrably moved upward.

4.5 Post test investigation

4.5.1 Water mass balance

The water level decreased by 600 mm during test PM14. This difference corresponds to a water depletion of 210 litres. A volume of 76 litres was found in the water separators, a volume of 39 litres of water could have been evaporated by 23.2 kg of melt. We conclude that the missing volume, 95 litres, was carried by the steam flow out of the vessel as droplets.

4.5.2 Melt balance and sieve analysis

Results are given in Table 4.1 and Fig. 4.23.

The total mass of fragments found after the test was nearly the same as in PM13. The mass which was transported into the water separators as well as the mass which was found at the bottom of the facility was smaller than the corresponding masses in PM13. This finding might be an indication that the interaction process was less violent. On the other hand, the pressures recorded during PM14 were the largest ones in all three experiments.

Table 4.1 PM14; sieve analysis of fragments broken down in the sites of recovery.

Location	Quantity		Magnetic fraction	Non- magnetic fraction	Total
Water separators	Mass	g	1959.0	1372.2	3331.2
	Mass mean diam.	mm	-	-	2.63
	Sauter mean diam.	mm	1.44	1.14	-
	Total surface	m^2	2.211	2.406	4.617
Fragment catcher	Mass	g	3366.4	6088.8	9455.0
	Mass mean diam.	mm	-	-	12.57
	Sauter mean diam.	mm	8.15	14.70	-
	Total surface	m^2	0.673	0.854	1.527
Basis of test vessel	Mass	g	5885.2	4522.1	10407.3
	Mass mean diam.	mm	-	-	9.49
	Sauter mean diam.	mm	5.92	5.28	-
	Total surface	m^2	1.620	1.765	3.385
Total	Mass	g	11210.6	11982.5	23193.3
	Mass mean diam.	mm	-	-	9.47
	Sauter mean diam.	mm	5.92	5.28	-
	Total surface	m^2	4.504	5.025	9.529

The mass mean diameter was evaluated to be 9.47 mm. The smallest diameter was measured in the material found in the water separators, the largest one in the material collected from the melt fragment catcher.

The Sauter mean diameter is given for magnetic and nonmagnetic material separately assuming a density of 3860 kg/m^3 and 3000 kg/m^3, respectively.

4.5.3 Chemical analysis

The chemical analysis was skipped because the sieve analysis showed no significant difference to the results of PM13 and no substantial differences in the chemical composition were expected.

4.5.4 Gas analysis

Gas probes were sampled prior to and during the interaction in order to verify whether or not hydrogen is produced due to dissociation of steam. The existence of hydrogen or of any other non-condensable gas is known to influence steam condensation at colder water or structure.

Six steel bottles were connected to the test facility via magnetically operated valves. The valve positions and opening times are listed below:

Valve	Position, mm	Opened at time, s	Duration of opening, s
A1	1400	-5.0	1.0
A2	1600	1.260	0.2
A3	1200	1.060	0.2
A4	865	0.860	0.2
A5	465	0.660	0.2
A6	65	0.460	0.2

The bottles were evacuated a short time prior to the test. Valve A1 was to collect the representative steam/gas condition immediately before the test. The valves A6 to A2 were opened in time steps of 0.2 s, one after the other, to reach an overall sampling time of 1 s.

The gas analysis was performed using a mass spectrometer. Because the steam within the bottles had been condensed at the time of analysis, additional gas filling (argon) was necessary to induce a gas flow towards the spectrometer. Four calibration procedures were performed (labelled T1 to T4 in Table 4.2) using gas mixtures

that were typical of those originating in thermite reactions. The results of the analysis can be summarized as follows:

1. Hydrogen was produced during the interaction. This is evidenced by the fact that the sample taken prior to test showed no hydrogen at all.

2. The steam/gas atmosphere still contained residual fractions of air, although our efforts were directed to replace the air by steam by maintaining boiling conditions for more than half an hour.

3. No variation in the concentration could be detected, neither related to the axial position nor to time.

Table 4.2 Gas analysis in PM14; the numbers give volume fractions in %.

No	Measurement	C_{H2}	C_{Ar}	C_{N2}	C_{02}	C_{H2} (norm.)
T1	Ar/5% H_2	6	94	0	0	
T2	Ar	0	100	0	0	
T3	air	0	1	79	20	
T4	Ar/50% H_2	55	45	0	0	
F1	A1	0	19	64	16	0
F2	A2	2.0	24	58	14	2.3
F3	A3	0.3	24	60	16	0.4
F4	A4	0.4	29	57	14	0.15
F5	A5	1.6	22	61	16	1.9
F6	A6	3.2	19	64	13	3.7

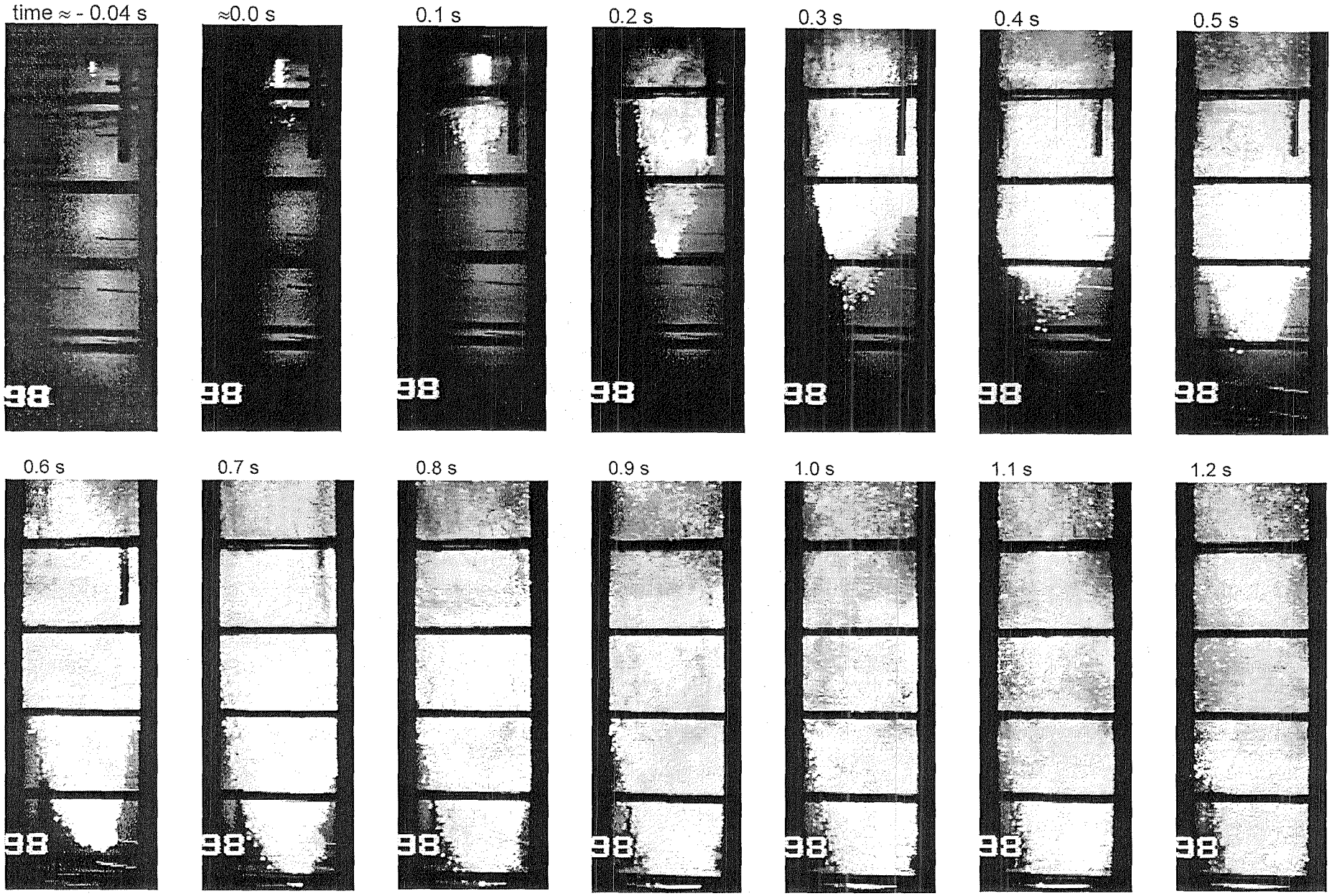

Fig. 4.1 Development of the interaction zone in PM14 shown by selected pictures of the video film.

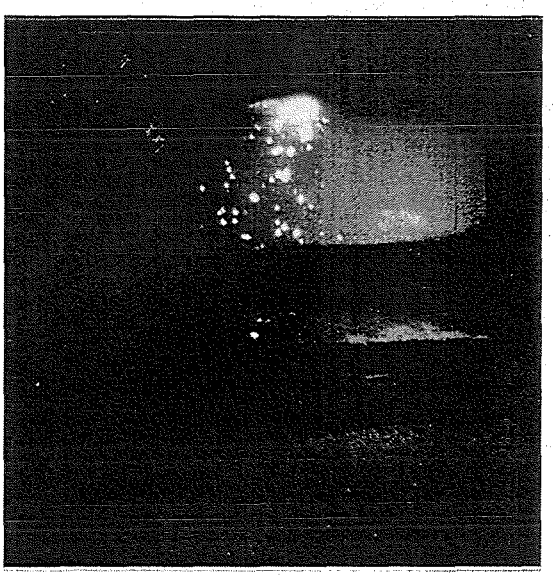

time ≈ -0.035 s

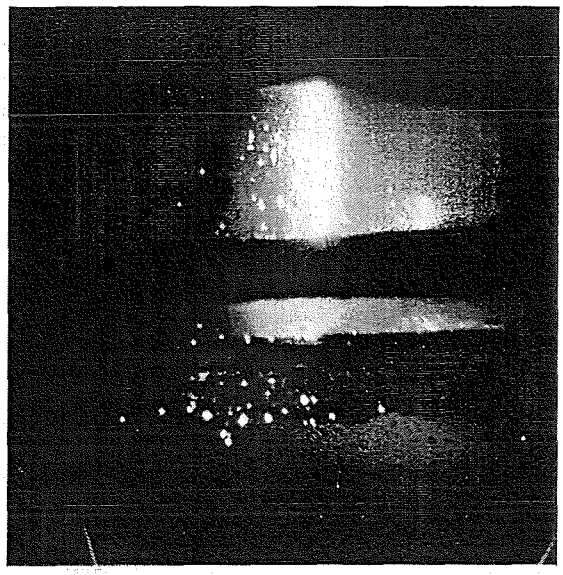

time ≈ 0 s

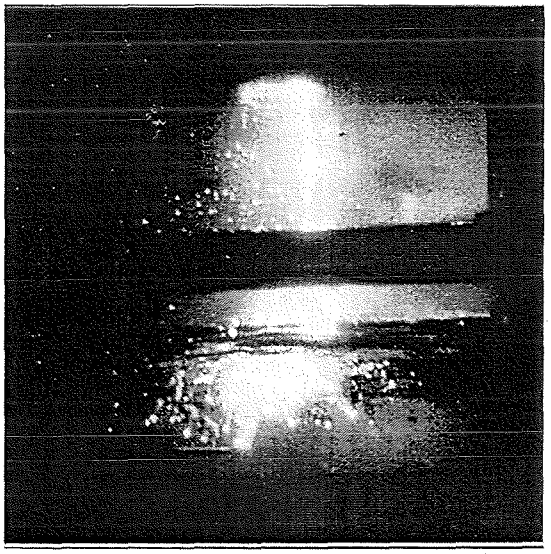

time ≈ 0.028 s

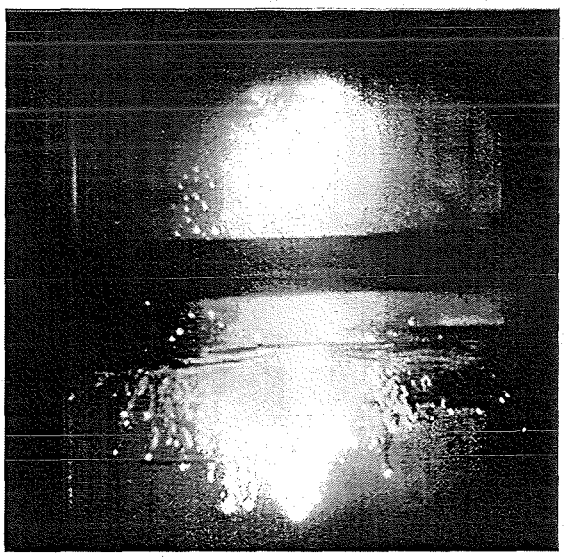

time ≈ 0.054 s

time ≈ 0.075 s

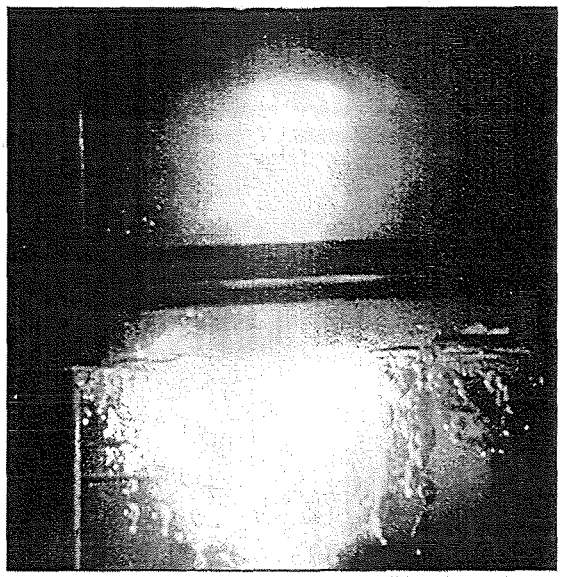

time ≈ 0.116 s

Fig. 4.2 Film pictures taken by a high-speed camera show the initial time in PM14.

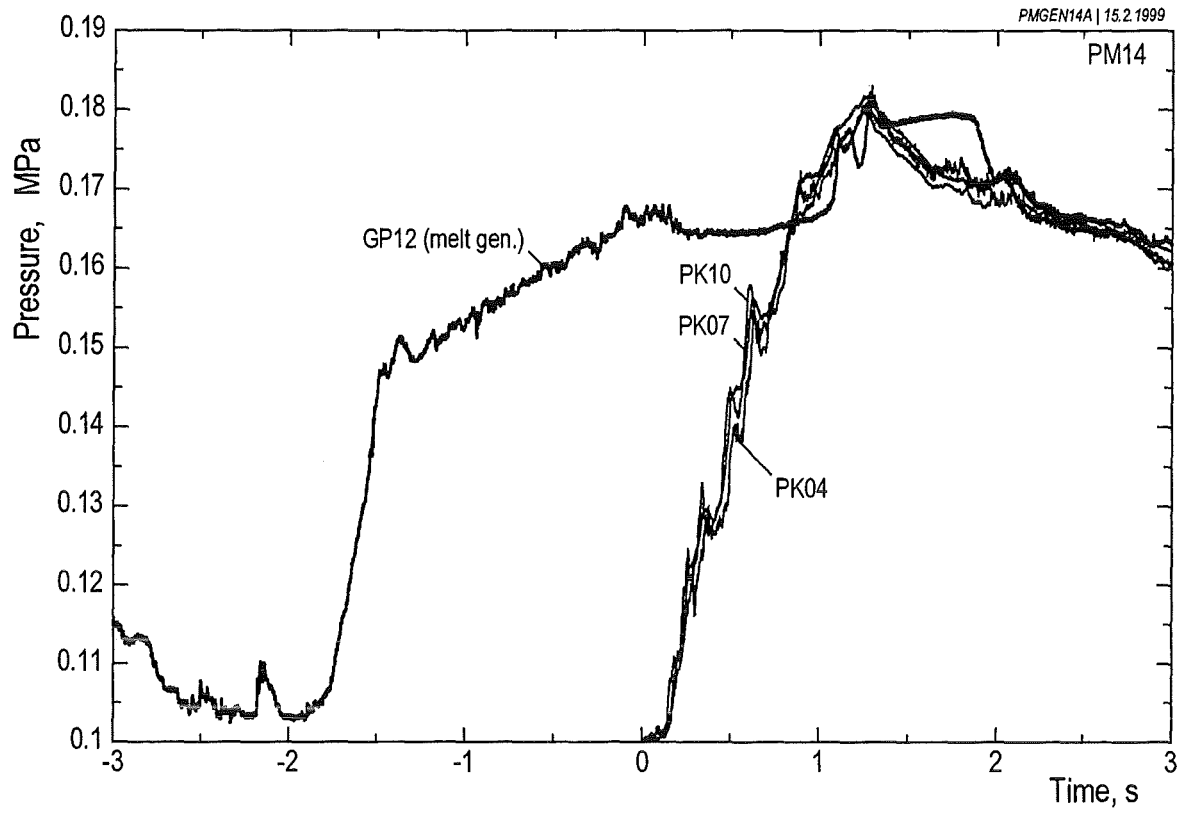

(a) Survey.

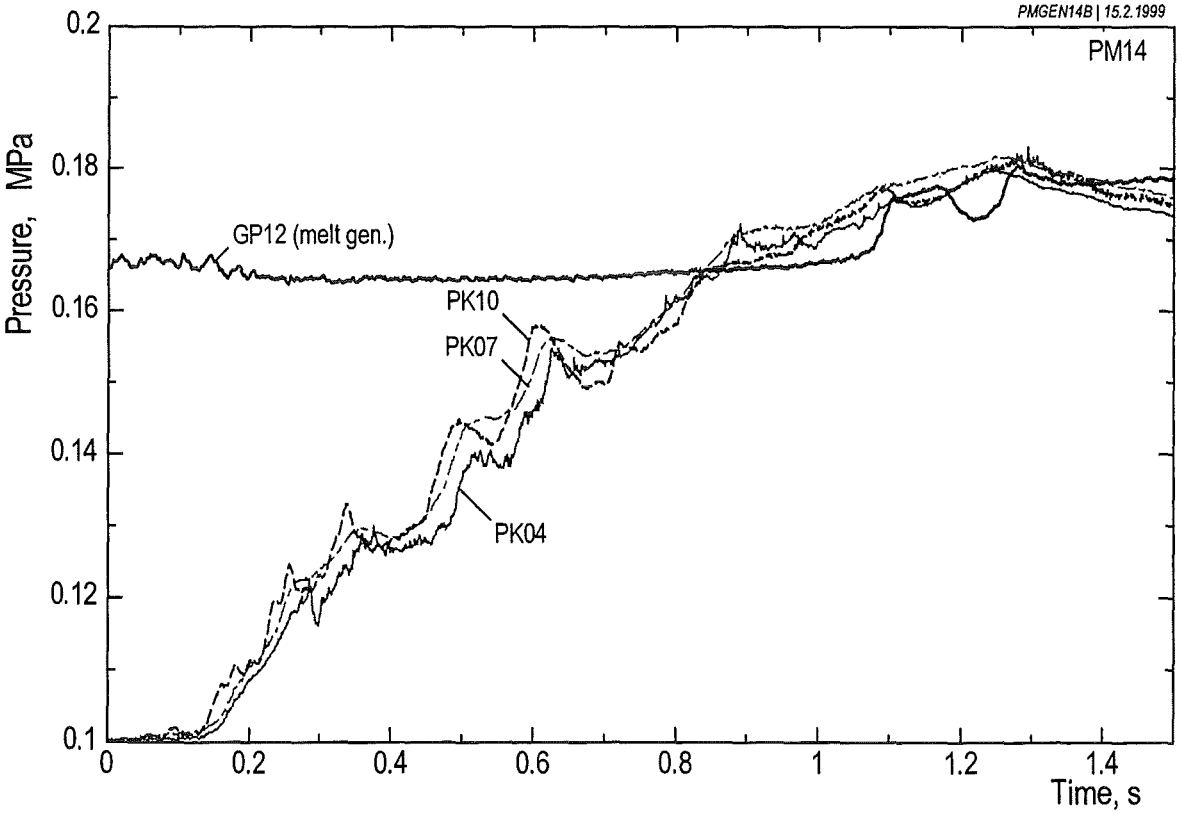

(b) Larger time scale.

Fig. 4.3 Pressures obtained from inside and outside of the melt generator

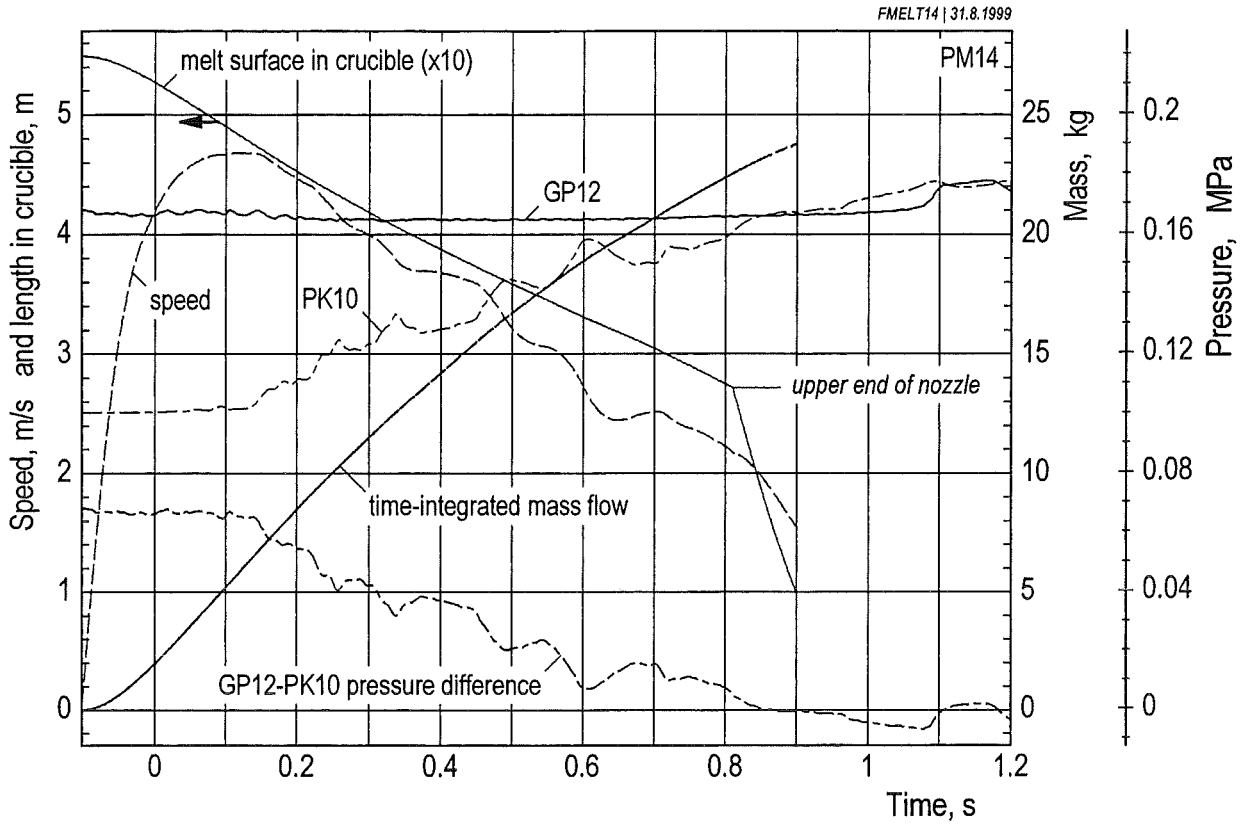

Fig. 4.4: Melt release calculated on basis of the pressure difference. The calculation started at the time estimated for steel membrane break. The length in crucible is related to the lower end of the nozzle.

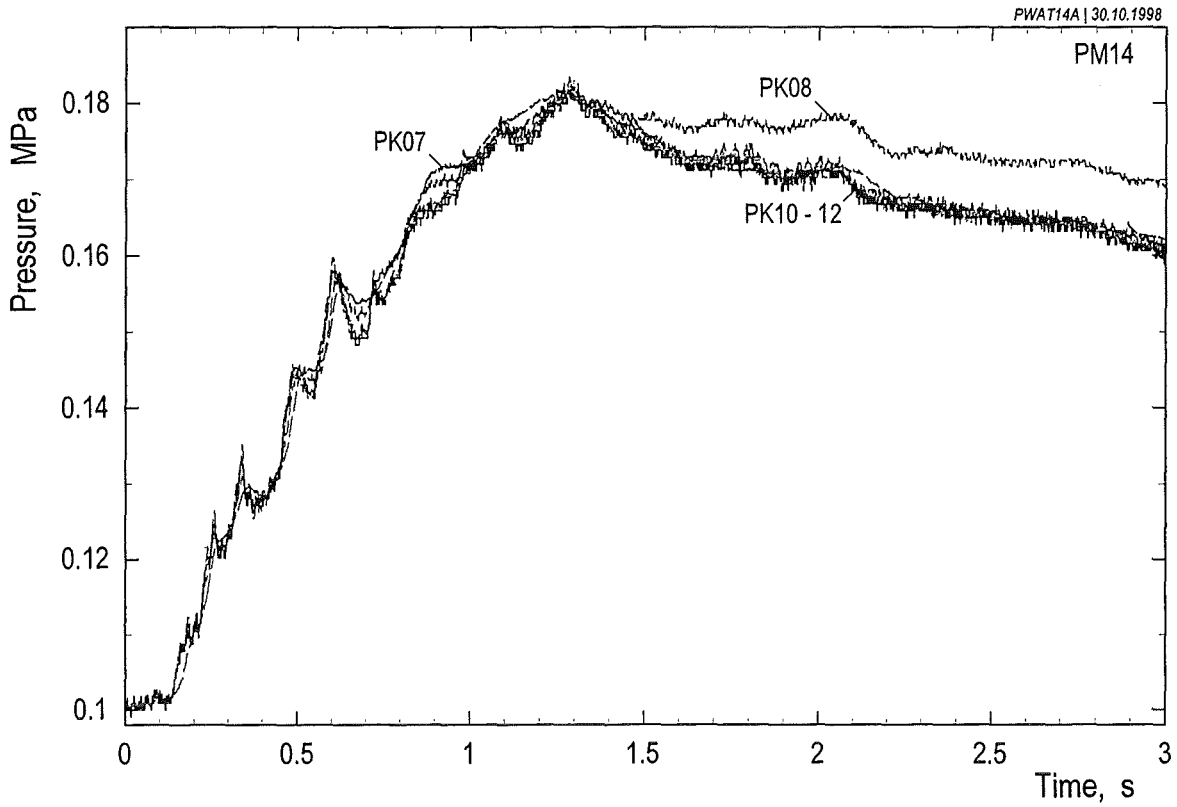

(a) Time = 0 ... 3 s

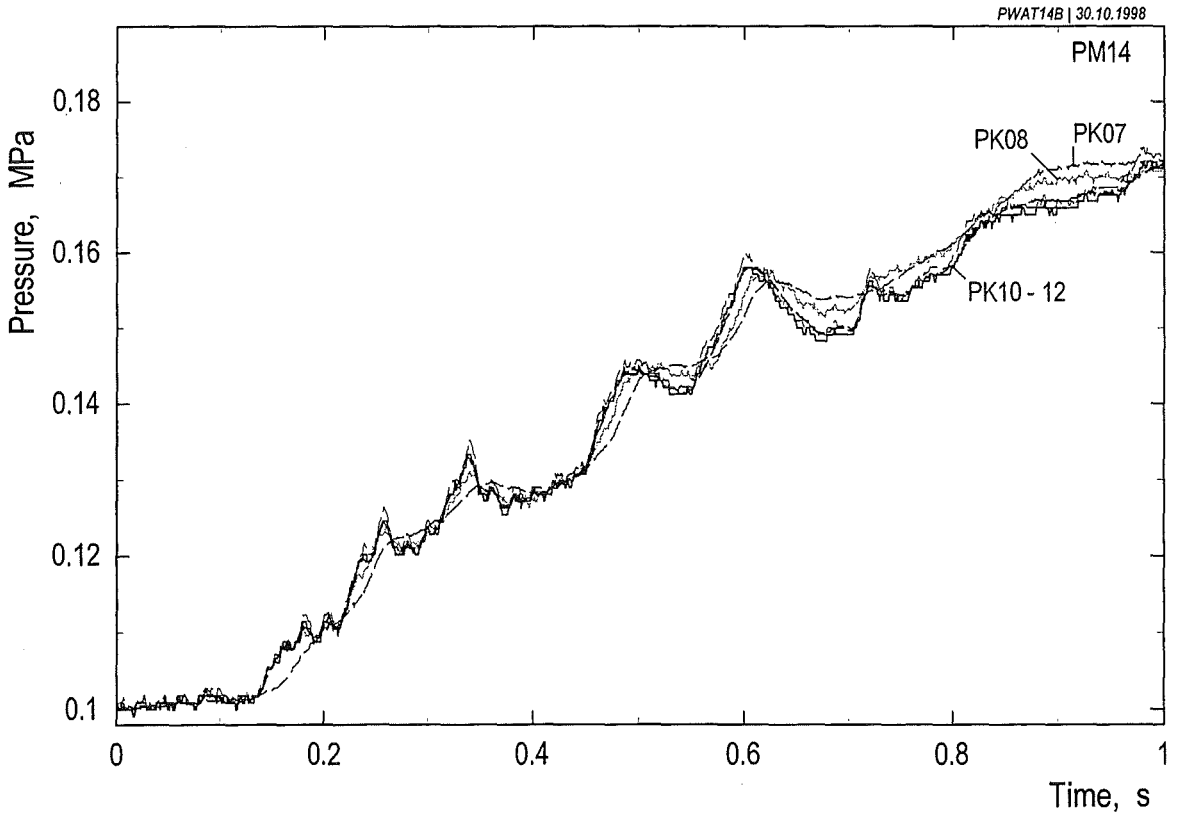

(b) Larger time scale

Fig. 4.5 Pressure data obtained from the water pool.

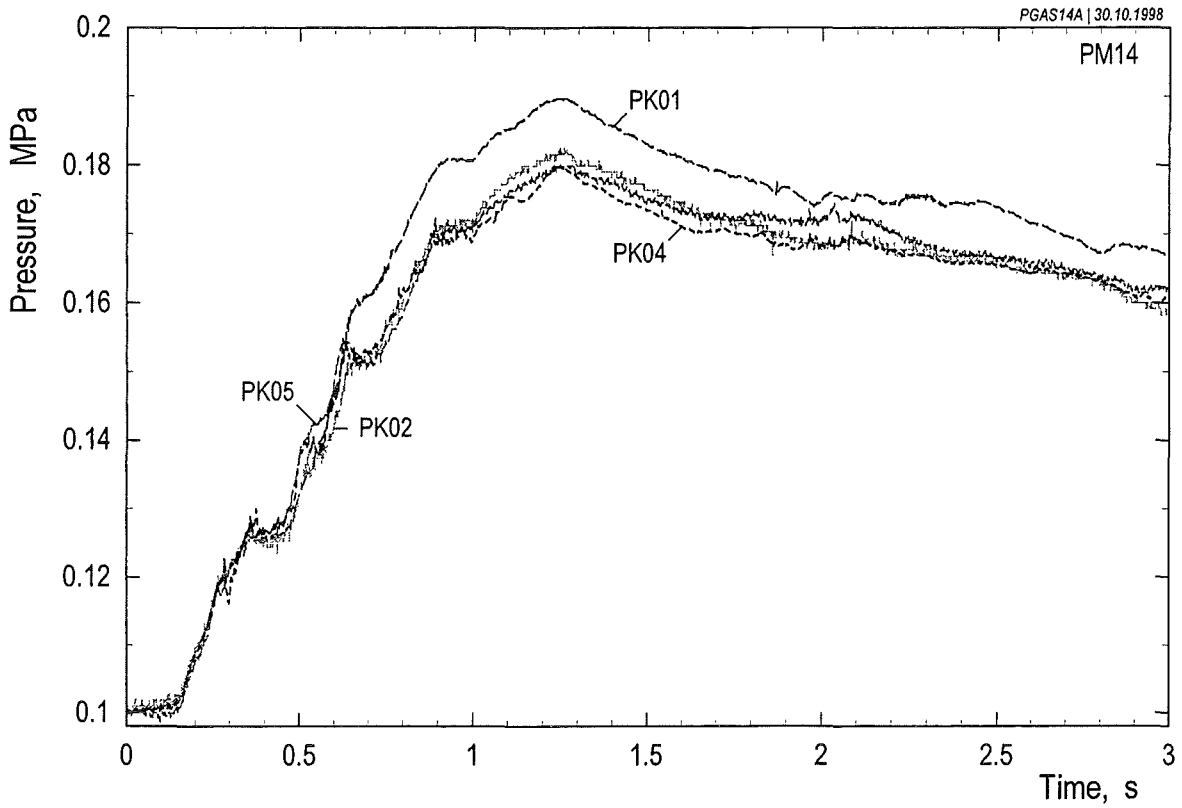

(a) Time = 0 ... 3 s

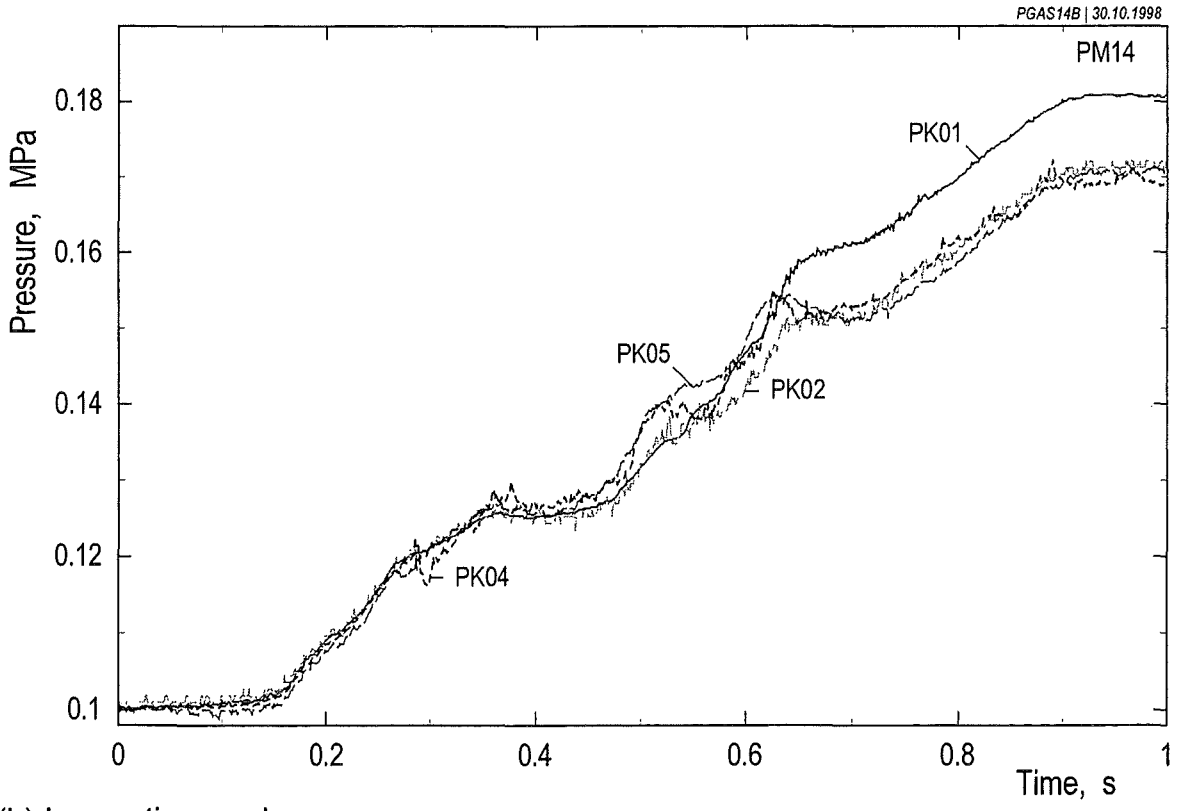

(b) Larger time scale

Fig. 4.6 Pressure data obtained from the freeboard volume and from the annular compartment.

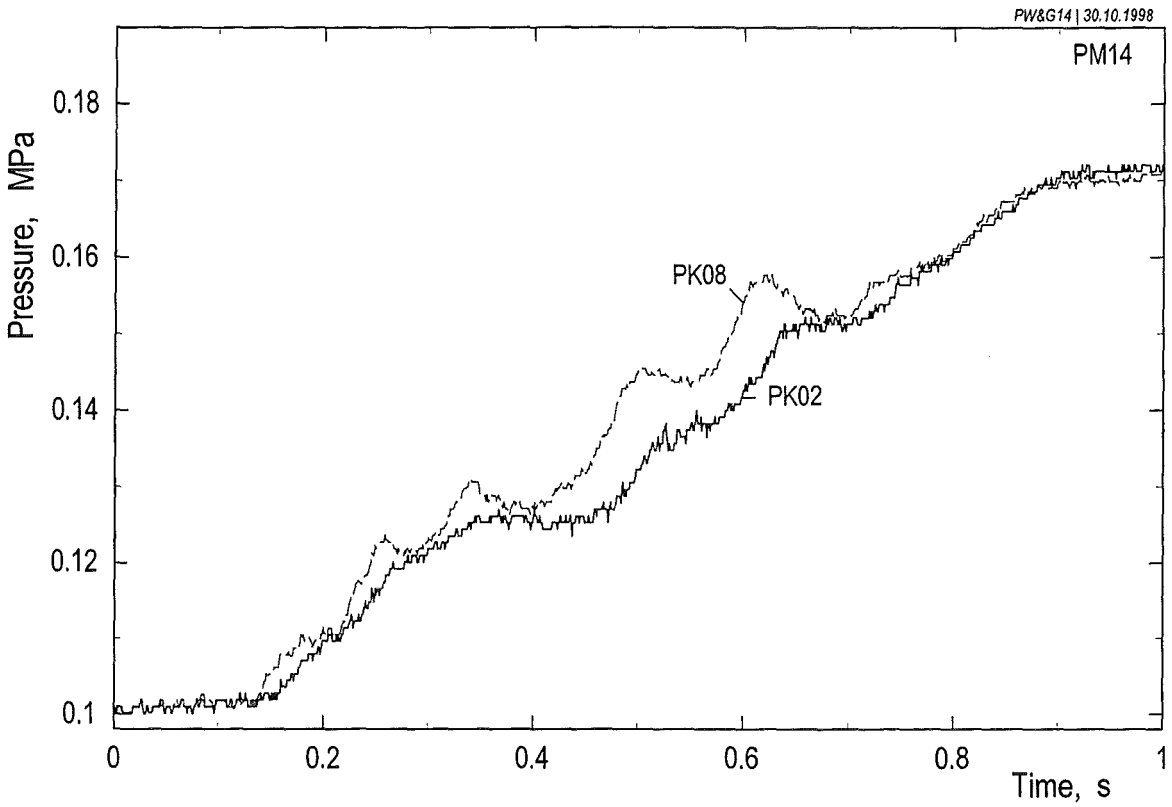

Fig. 4.7 Comparison of pressure data obtained in the water (PK08) and in the annular gas space (PK02).

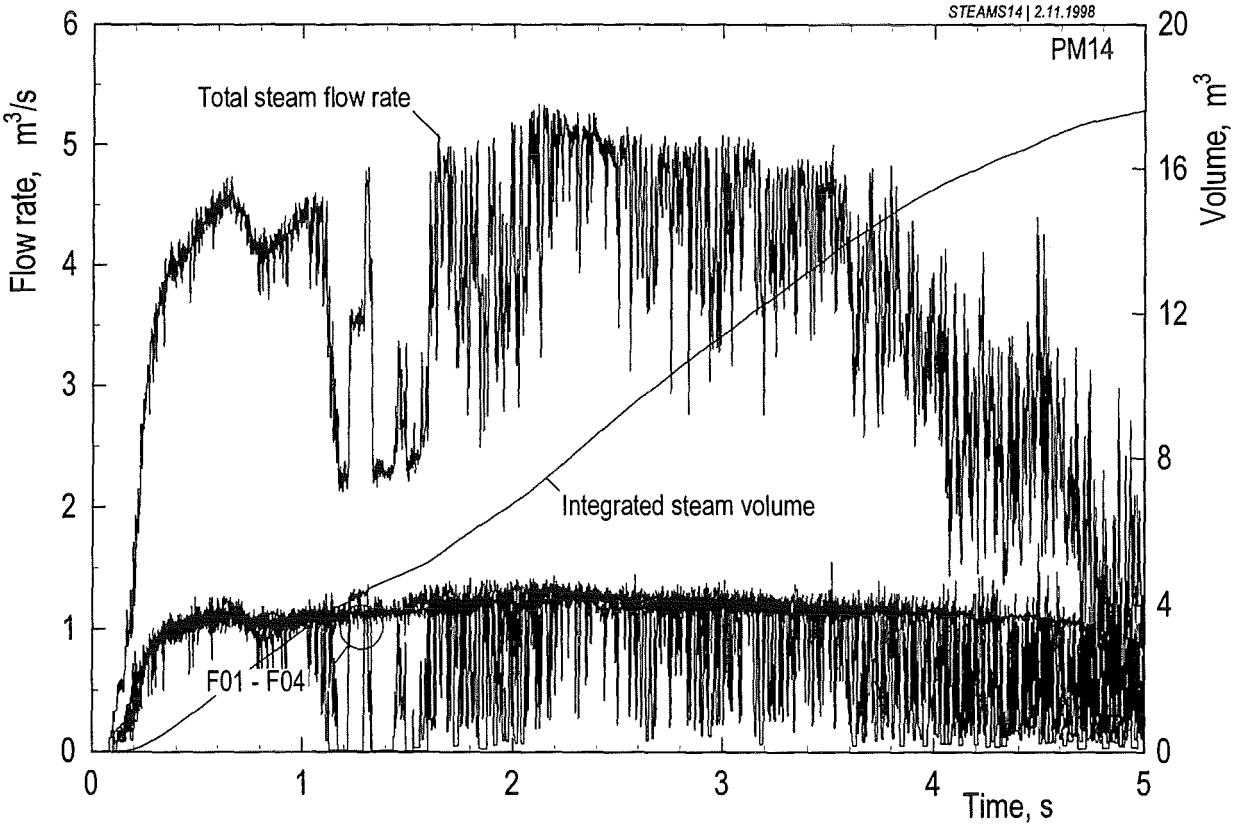

Fig. 4.8 Steam flow rates and steam volume integrated over time.

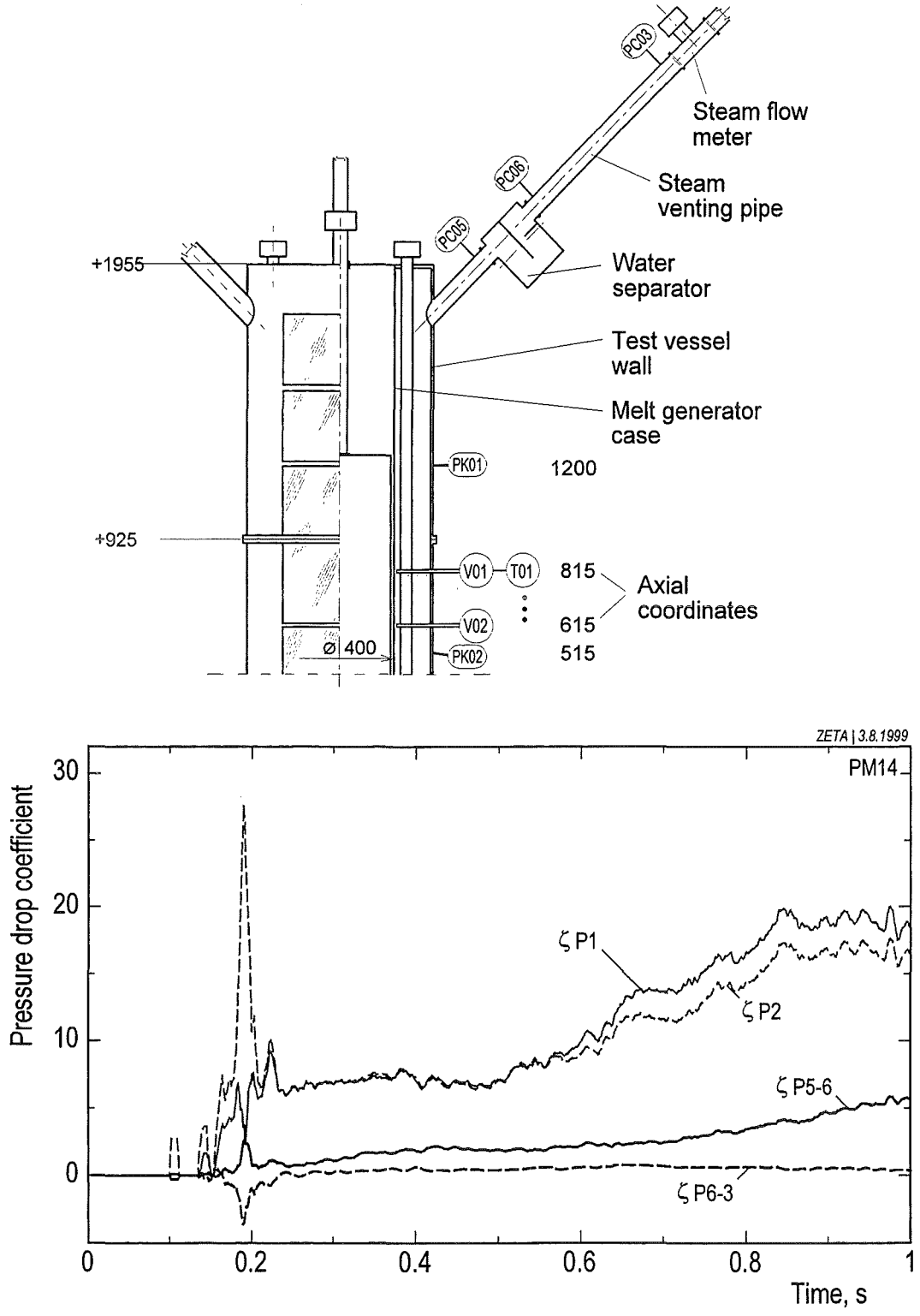

Fig. 4.9 Loss coefficients across several sub-sections of the steam flow path including venting pipe No 3. Locations of the transducers are given in the upper part. Reference pressure for the ζ_{P1} and ζ_{P2} coefficients was the ambient pressure.

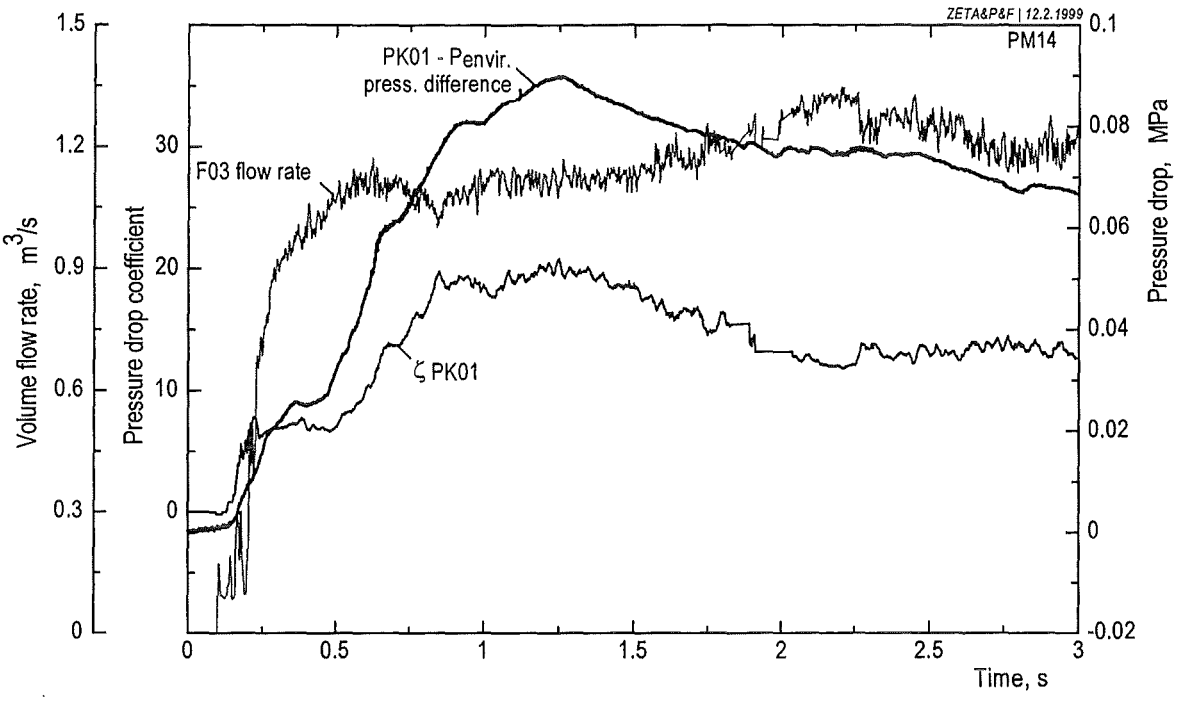

Fig. 4.10 ζ_{PK01} loss coefficient calculated on basis of the PK01 pressure data and the steam flow rate ($P_{envir.}$ = environment pressure; F03 data faults around 1.8 s have been eliminated).

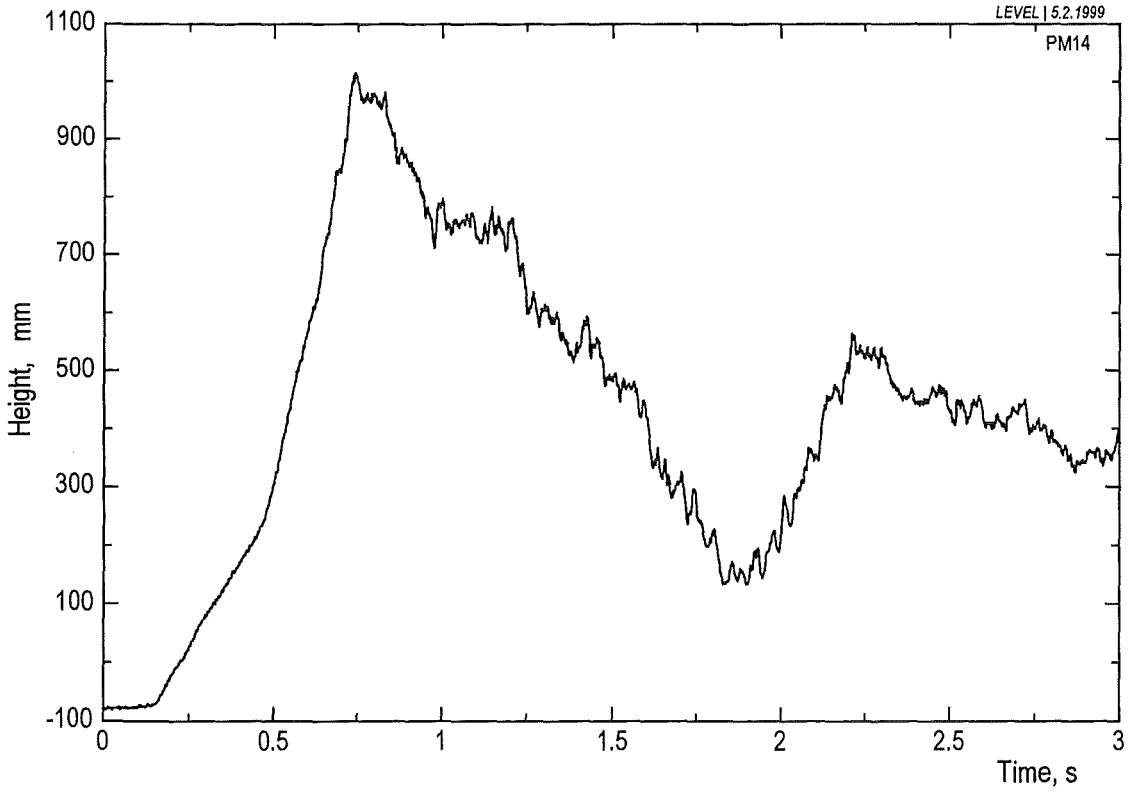

Fig. 4.11 Average of the four water level measurements

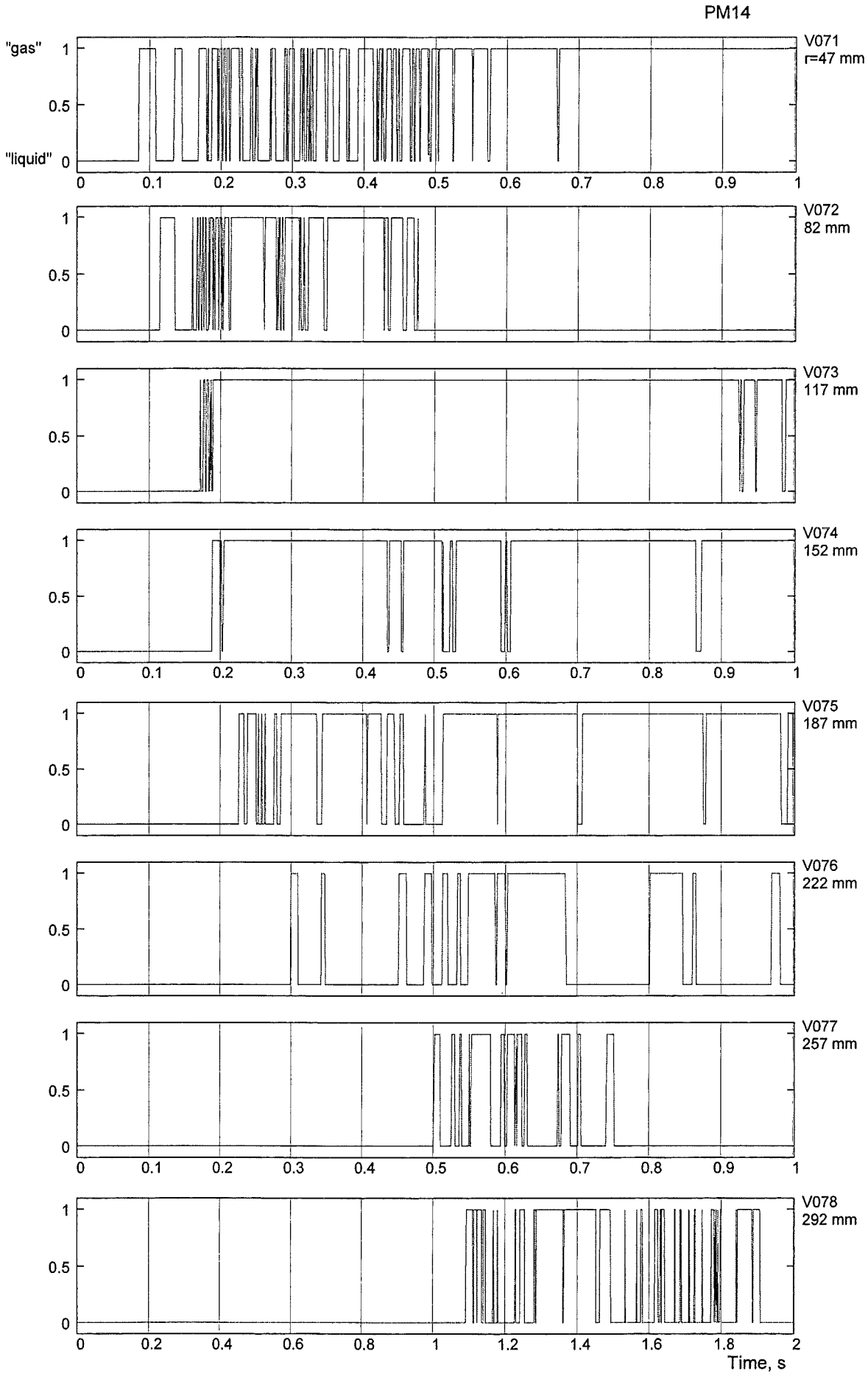

Fig. 4.12 (a) Void signals from the V07 lance (67 mm below the init. water level)

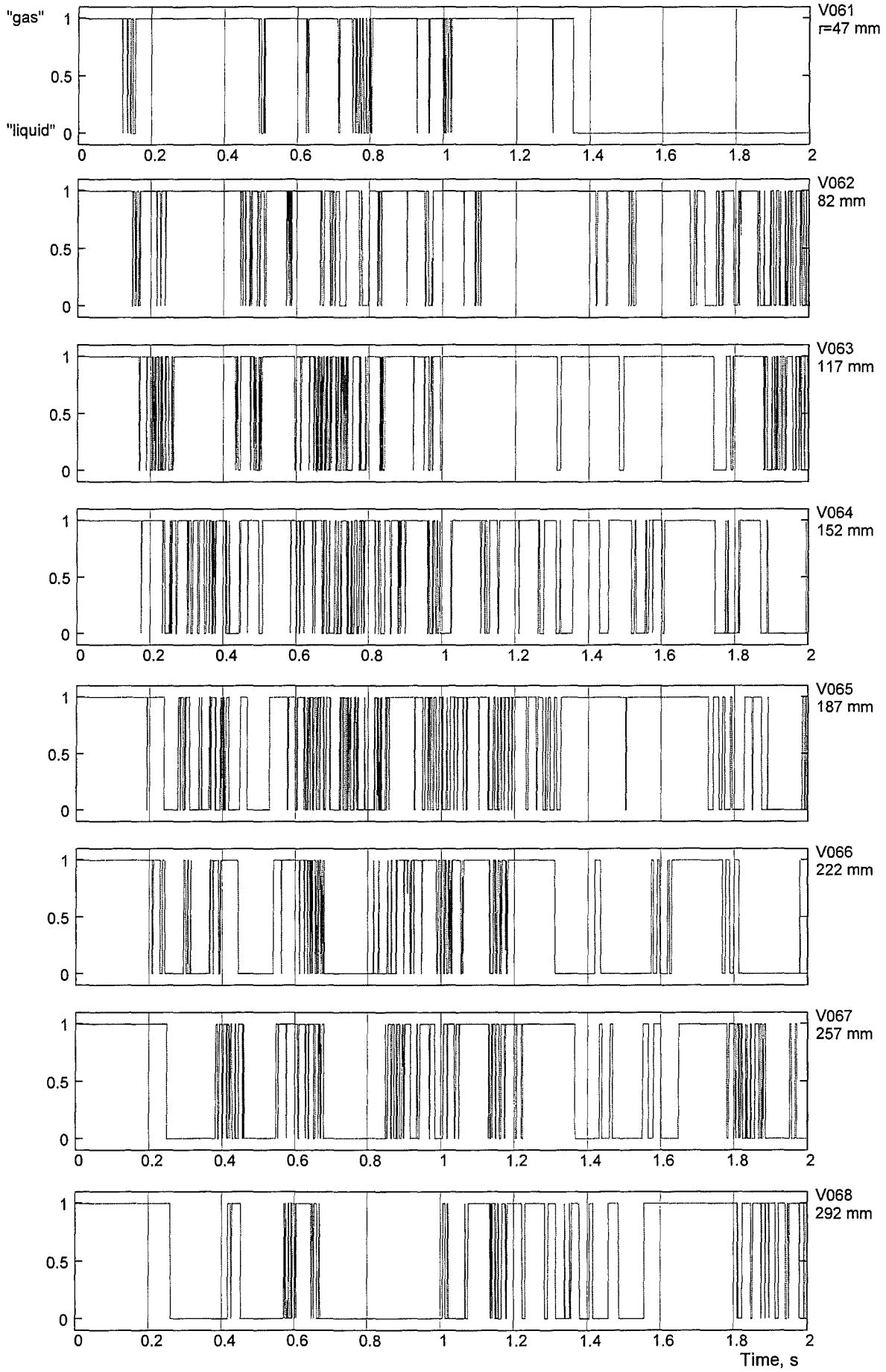

Fig. 4.12 (b) Void signals from the V06 lance (97 mm above the init. water level).

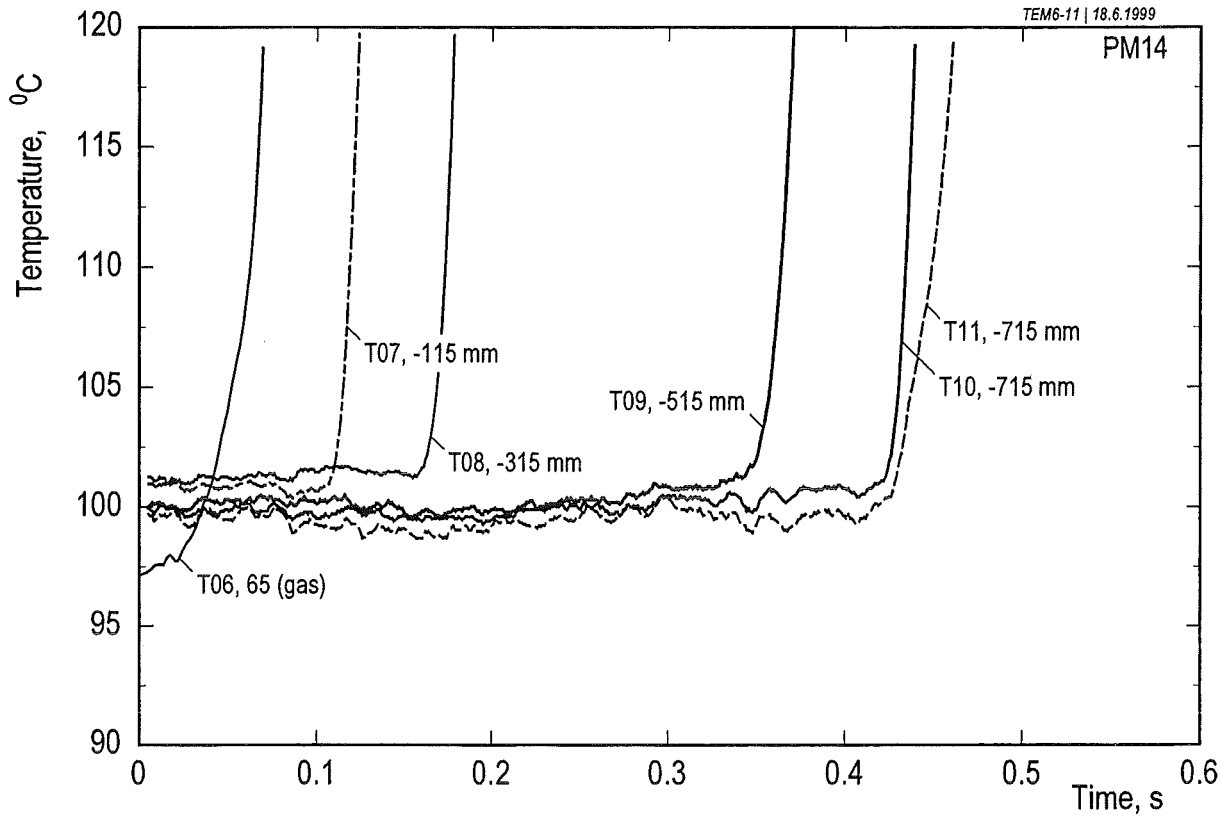

(a) upper part of the water pool

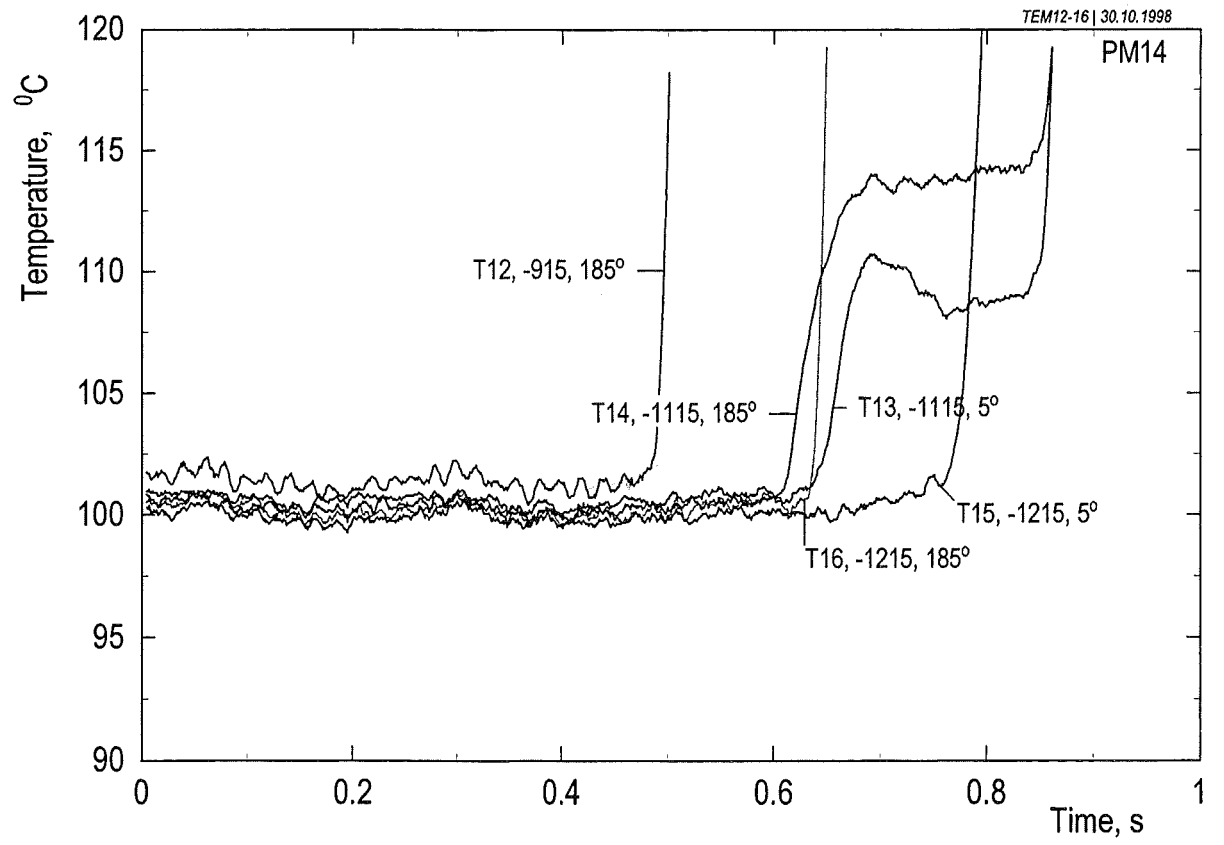

(b) lower part of the water pool

Fig. 4.13 Temperatures measured in the water pool (T07 - T16). The T06 data also shown (a) are obtained a short distance above the initial water level.

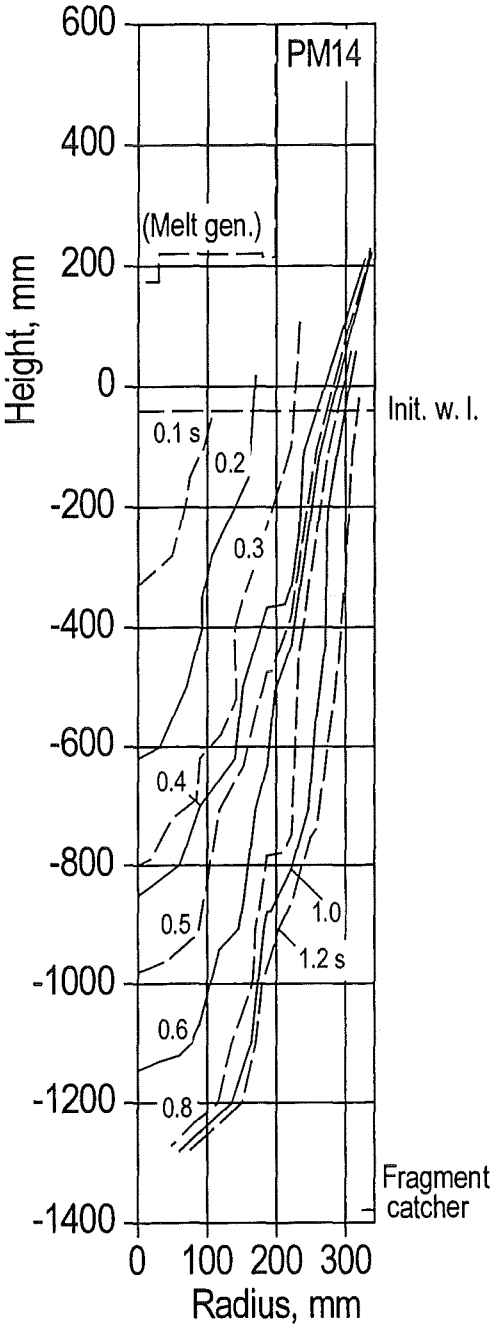

Fig. 4.14 Progression of the interaction zone into the water with the time as a parameter

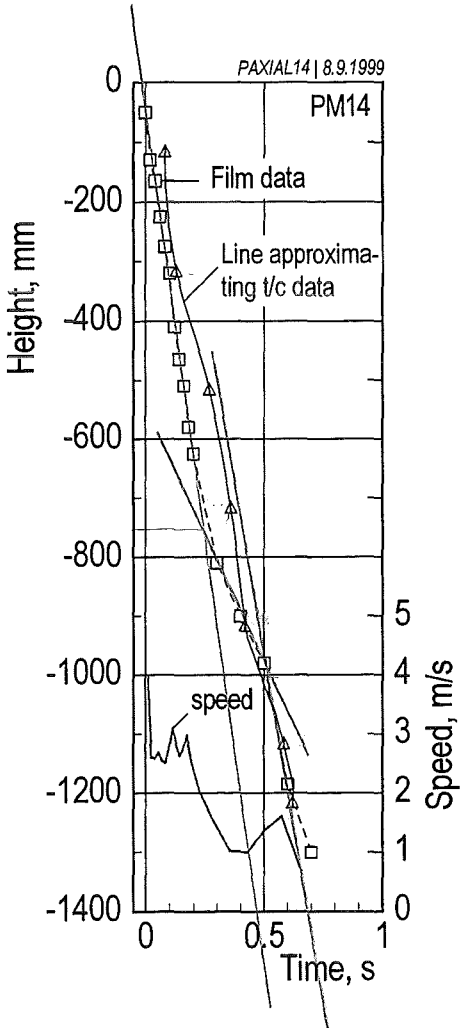

Fig. 4.15 Progression of the interaction zone in the centre of the pool. The speed is derived from film data.

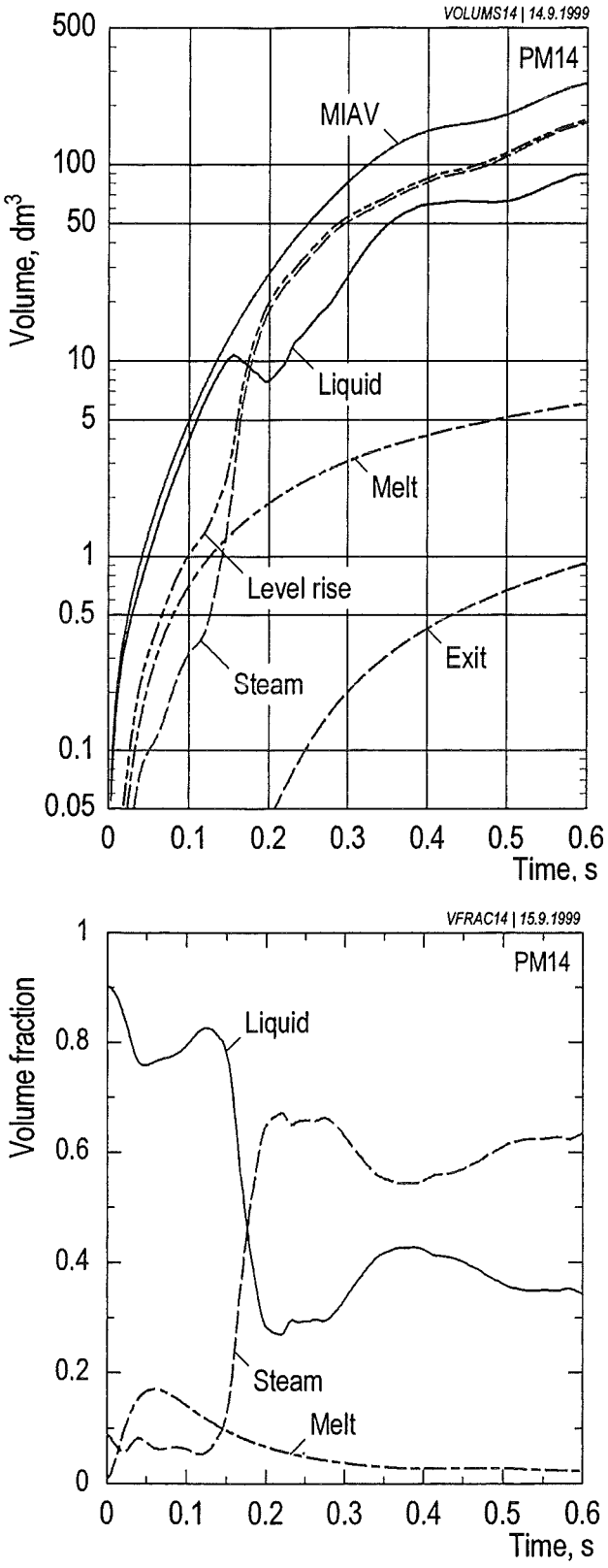

Fig. 4.16 Volumes resulting from the interaction (MIAV=multiphase interaction volume; Exit= volume of the evaporated part of water; volume due to level increase) and partial volumes of the interaction zone (steam, liquid, and melt) are shown on top, average volume fractions of the components inside the interaction zone below.

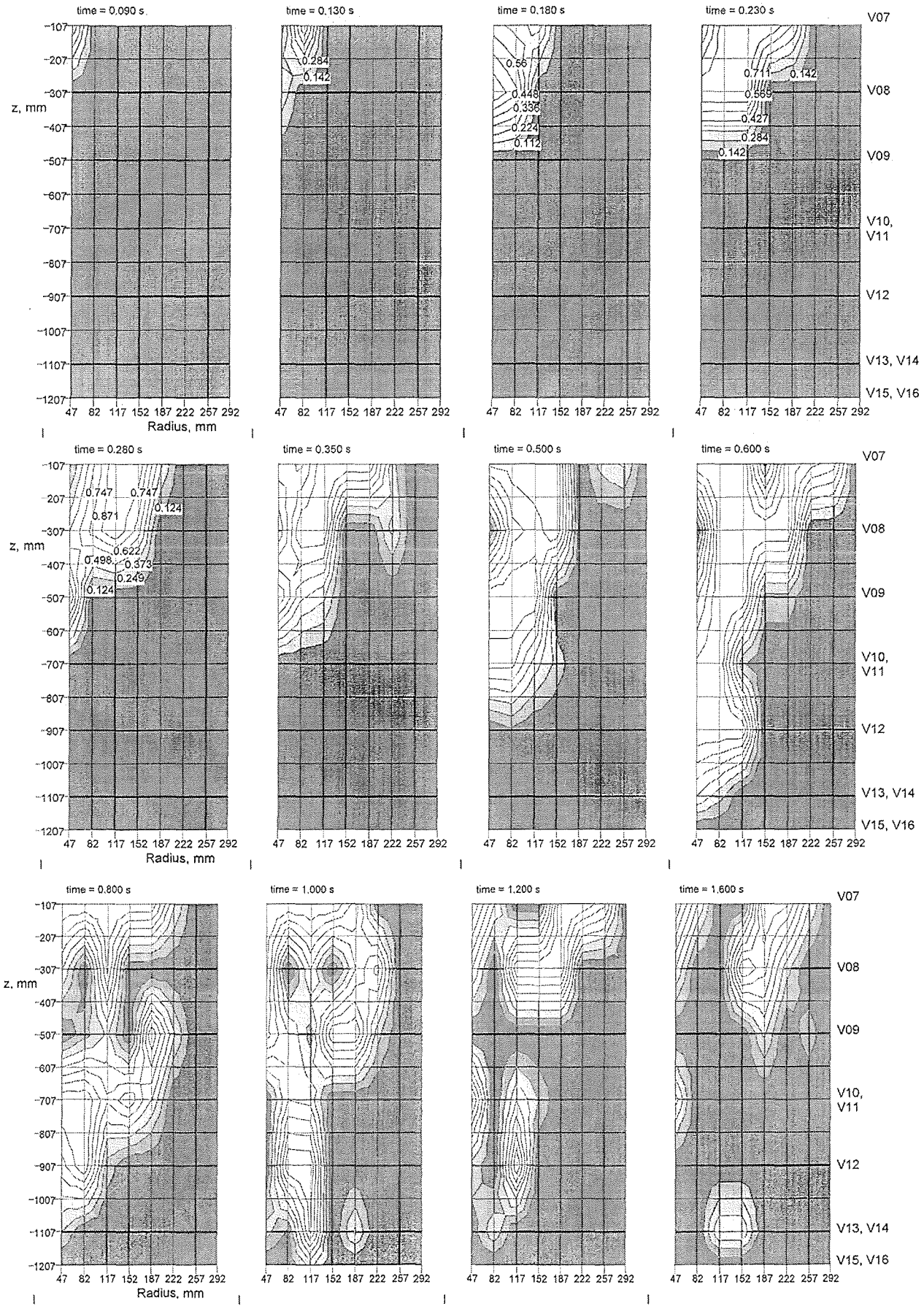

Fig. 4.17 Distribution of steam and water in the water pool in PM14 at various times (white area =100% steam; dark =100% water). Distance between fraction lines: ≈ 0.125

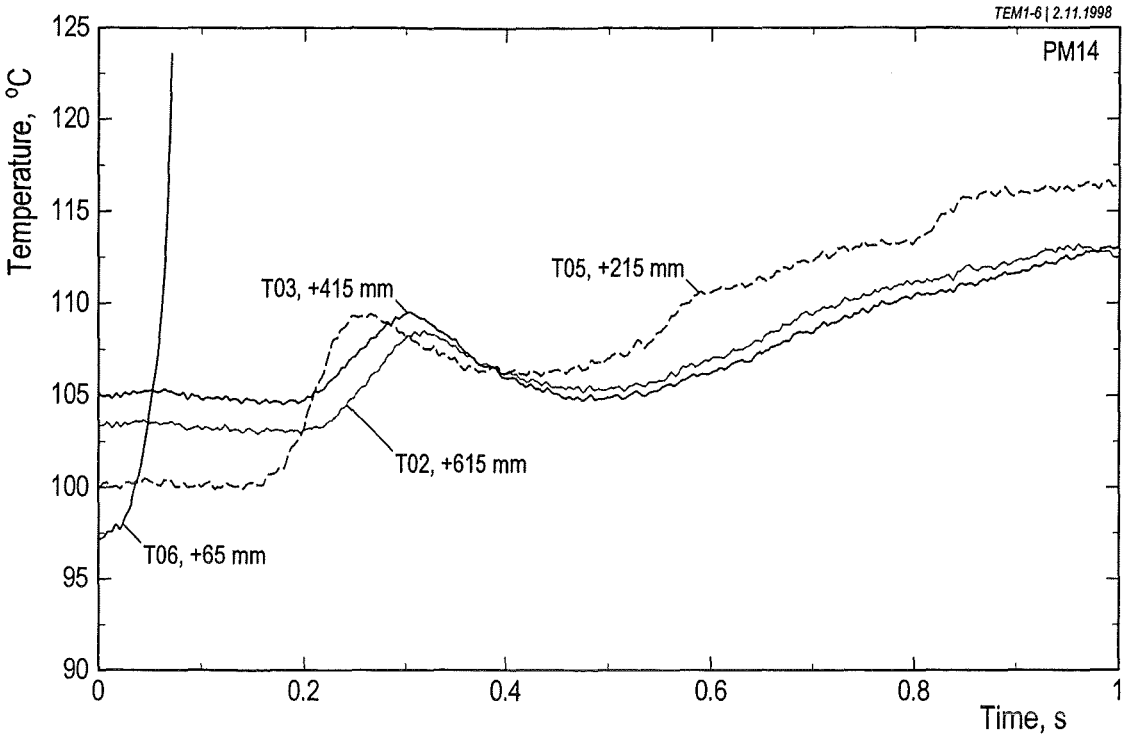

Fig. 4.18 Temperatures measured in the freeboard volume (T06) and in the annular gas compartment (T02 – T05).

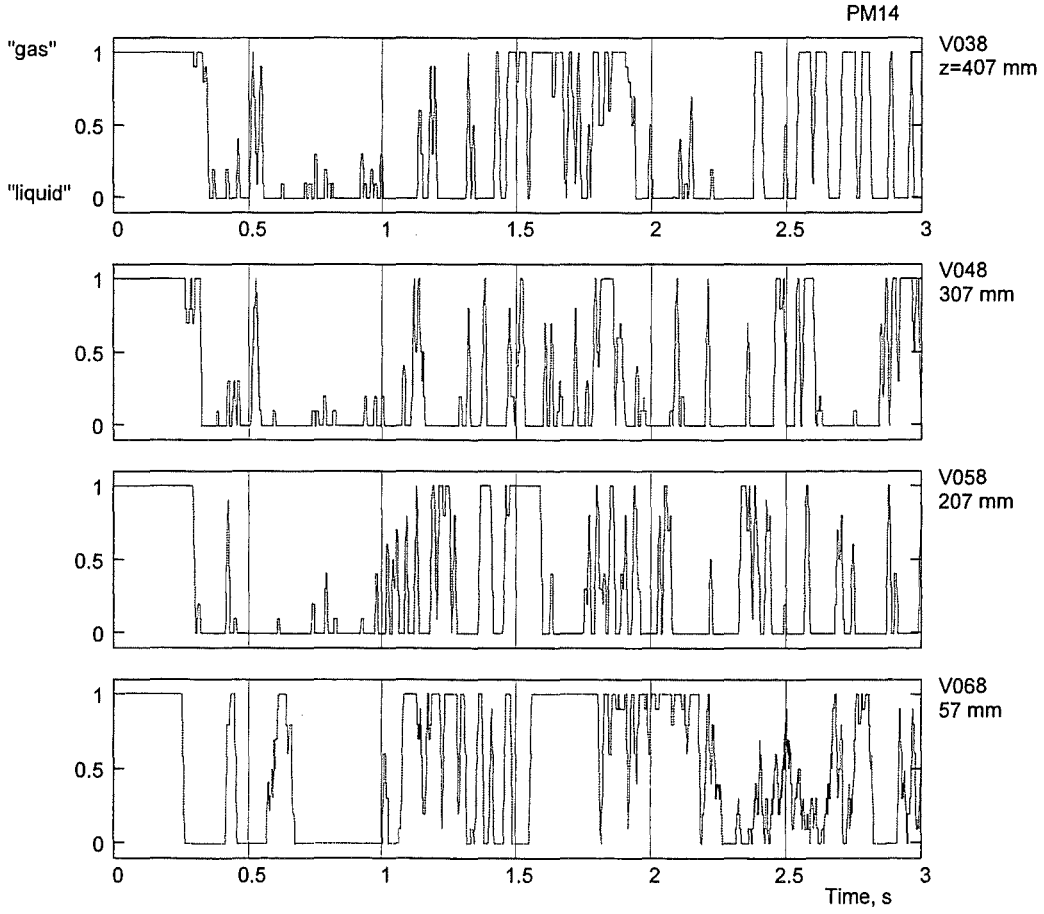

Fig. 4.19 Void signals obtained from the freeboard volume (V06) and the annular gas compartment at various heights. Smoothed signals (cf. Fig. 2.6) have been chosen to get a better time resolution. The measuring tips were close to the test vessel wall.

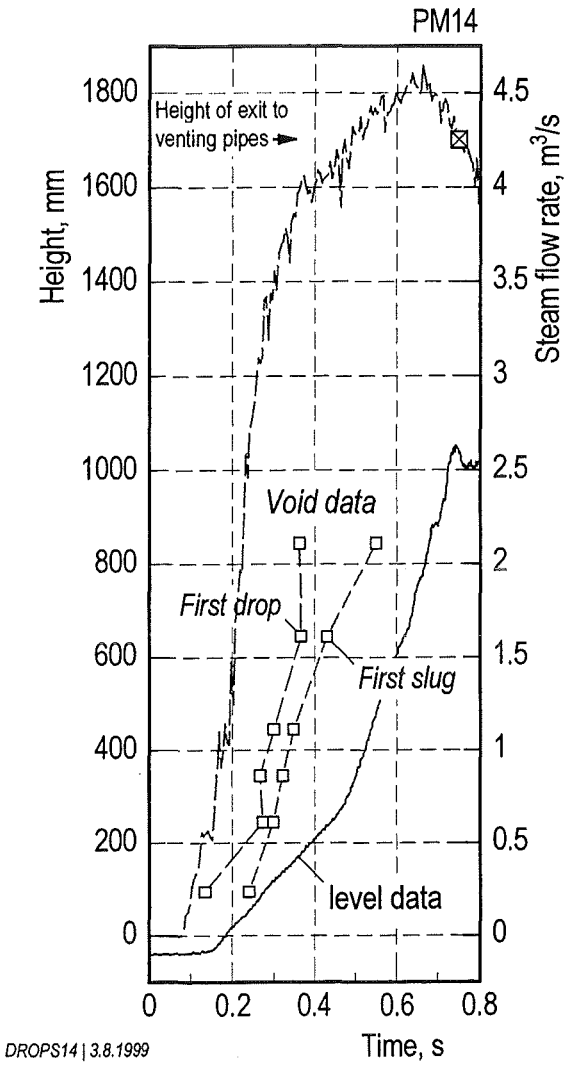

Fig. 4.20 Penetration of water into the annular gas compartment versus time compared with the water level rise. The steam flow rate is also shown.

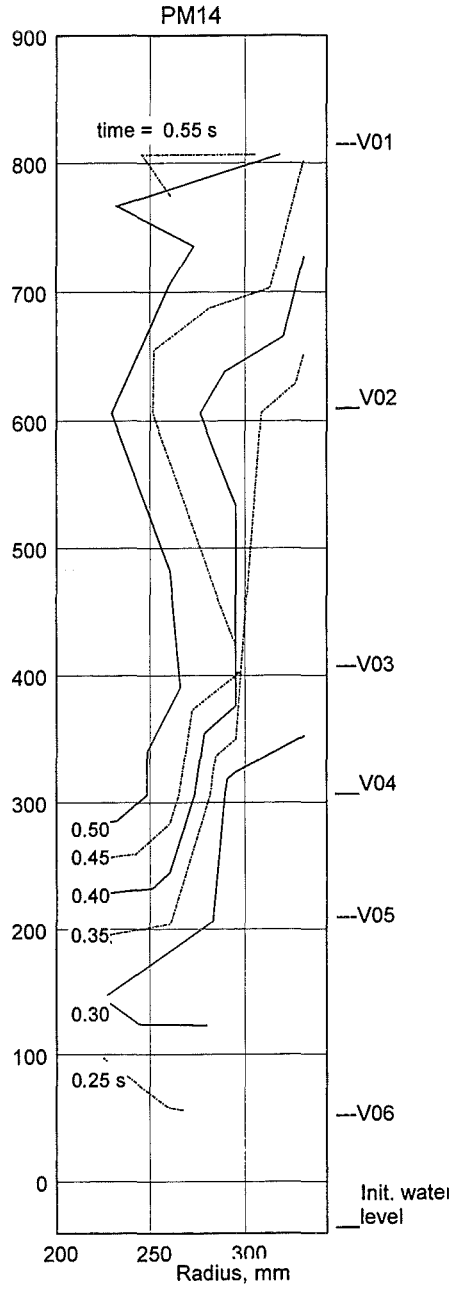

Fig. 4.21 Progression of the water front (drops and slugs) into the annular gas space shown with the time as a parameter.

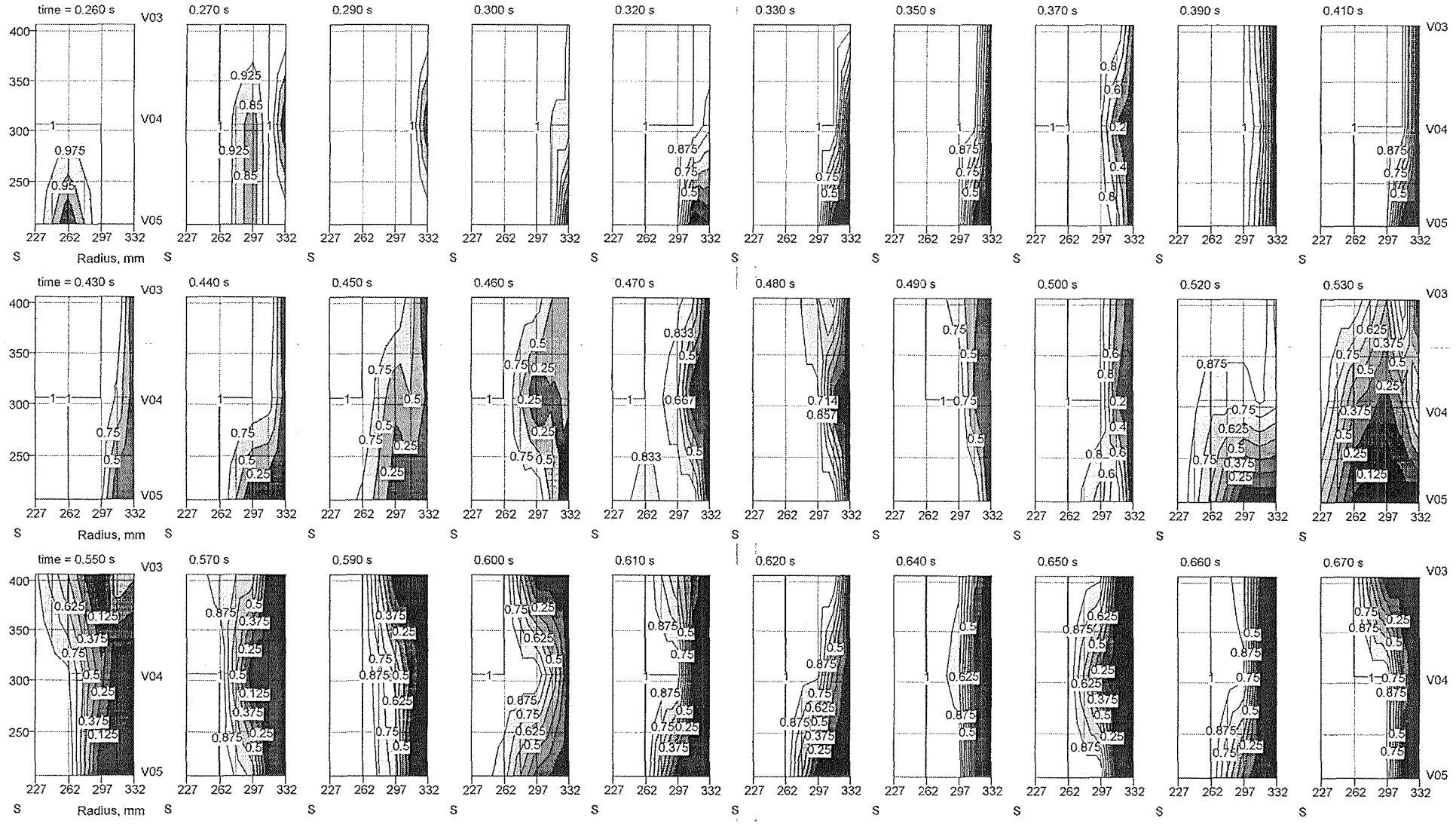

Fig. 4.22 PM14. Distribution of steam (gas) and water across the annular gas compartment between 207 and 407 mm height gained from void data. Time between the pictures is 0.01 s, in some cases 0.02 s. Void fraction lines: 1 = 100% steam; 0 = 100% water.

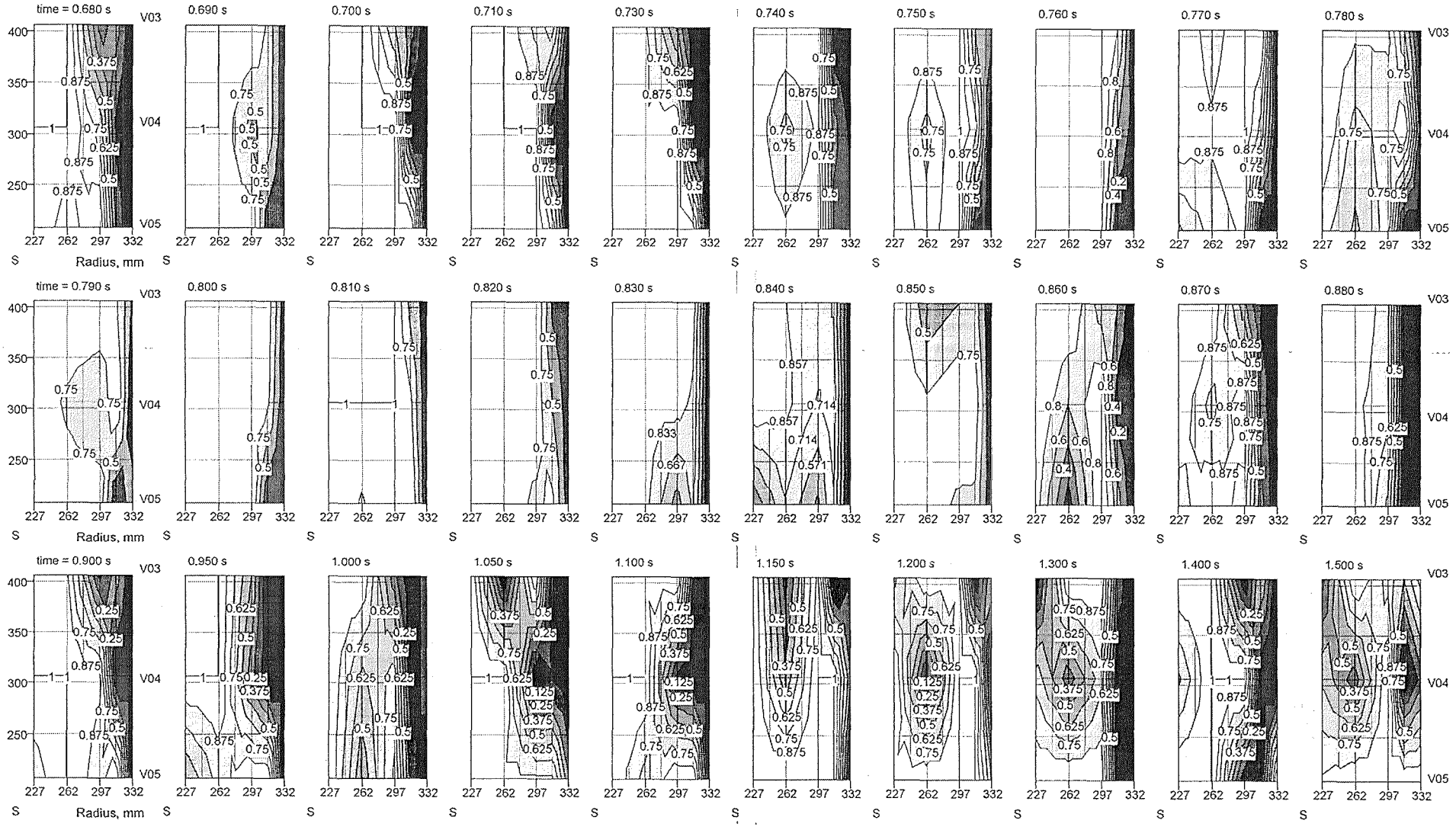

Fig. 4.22 (continued) PM14. Time between the pictures is 0.01 s; it is larger in the lowermost row. Void fraction lines: 1 = 100% steam; 0 = 100% water.

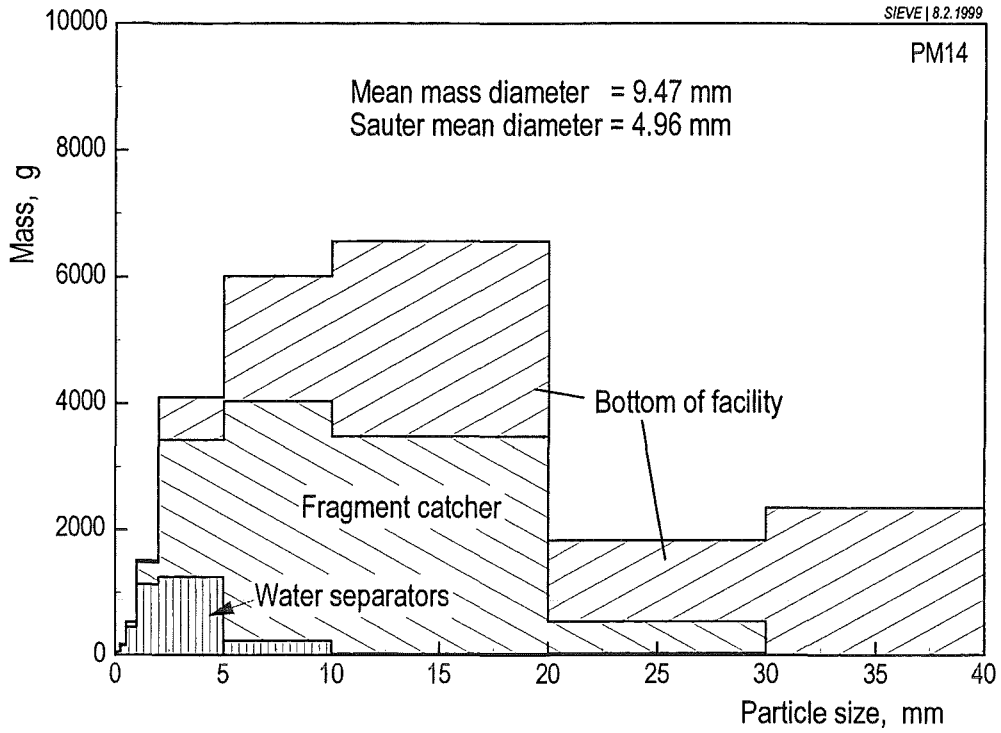

Fig. 4.23 Post-test particle size distribution of the melt fragments

5 RESULTS OF PM 12

5.1 General course of the experiment

Figure 5.1 gives a sequence of pictures obtained from video filming. The melt release started as single droplets. The very first droplet appeared at the nozzle end at time –0.054 s. The first few droplets moved at a speed of 3.57 m/s; they were followed by a shower of droplets. The following melt release was more substantial. A rather compact cylindrical stream of melt was formed.

The melt penetration and interaction with water caused only gradual initial increases in the water level and in the pressure. Considerable increases occurred only after 0.4 s when boiling became more intense. At that time, the melt had already penetrated 600 mm into the water and about 30% of the intended melt mass had been released.

The leading edge of the melt did not always move straight downwards. Instead, the leading edge tended to move laterally twice during the first time (see pictures in Fig. 5.1 at 0.1 and 0.3 s). The non-symmetrical progression lasted till about 0.6 s. Presumably, this behaviour is evidence of asymmetric forces acting during melt fragmentation.

One gets the impression from the films that the melt stream had been completely fragmented long before the melt reached the fragment catcher at 1.25 s. About at the same time, the pressure difference across the nozzle tube indicated that the melt release was terminated. As mentioned, it was in this test that an amount of melt larger than intended was released into the water (see also Section 5.2). The fragments gathered at the bottom gave rise to extended gross boiling. Melt fragments were seen to be swept over the rim of the fragment catcher; they sank down to the bottom of the test vessel. As soon as the melt release was terminated, the pressure in the interaction zone remained constant.

5.2 Pressure and level measurements

Estimation of the melt release function from pressure data The time history of the GP12 pressure trace, given in Fig. 5.2 together with the PK10 data, is interpreted as follows: The evolution of the GP12 pressure was determined, like in the other two tests, by a pressure (ramp) loaded at time = -2 s and by the following increase due to increase in the gas temperature lasting till time = 0. The somewhat steeper increase

afterwards, which was due to closure of the gas storage line, was overcompensated, from time 0.25 s on, by the loss of melt volume. The pressure went through a relative minimum until, at 0.9 s, pressure equalization was indicated. The steep increase in the GP12 pressure afterwards was caused by pressure compensation through the nozzle tube which had become empty. Pressure compensation ends at time 1.25 s; this time is taken as the end of melt release.

Results of the calculated mass release are shown in Fig. 5.3. The calculation started with a higher initial melt surface than in the other two tests (the crucible had been inadvertently overfilled with thermite powder in PM12). The calculation was stopped at 0.93 s. At that time, the integrated melt flow had reached a mass of 22 kg, about 3 kg of melt were still to be released. The melt surface was two centimetres above the upper end of the nozzle tube.

We presume that around that time (0.93 s), the iron cavity had been filled and the surplus 3 kg of melt composed of iron and alumina started to enter the nozzle tube. Post-test examination showed that the rim of the iron cavity had been molten off during the test. Obviously, this event allowed additional mass of iron to flow out of the cavity into the nozzle tube and to be released into the water. The total mass of melt released from the melt generator amounts to 29 kg (see Table 2.2). We conclude from the time history of the GP12 and PK10 pressure traces (Fig. 5.2) that the surplus melt mass was released between time 0.93 s and time 2.5 s and, from there, the course of events during the initial period of the test was not affected.

Pressures below the initial water level The signals of the four pressure transducers shown in Fig. 5.4 show rather uniform behaviour. Almost no pressure rise is seen up to the time 0.3 s, a small one occurred during the next 0.1 s. The main pressure rise, typical of all tests, took place in oscillatory manner after the time 0.4 s. The maximum pressure, 0.16 MPa, was reached at 1.2 s.

Pressures in the gas space are illustrated in Fig. 5.5. The time histories of the PK01 and PK02 pressures, which are very close together, show similar behaviour as the PK07 pressure obtained in the water pool. In contrast to that, the PK04 trace shows an overshooting amplitude and several spikes from the time 0.53 s on. Presumably, the PK04 transducer was heated by a melt particle nearby. The differential pressure between PK07 and PK01 drawn at the bottom of Fig. 5.5 can be regarded as an approximate measure for the steam flow losses between the top of the interac-

tion zone and the exit to the venting pipes. The maximum pressure measured in the gas space, 0.16 MPa, agrees with that in the water pool.

Change of the water level Up to 0.55 s, the four level measurements (Fig. 5.6) are close together. Thereafter, the traces start to diverge, where the L01 and L04 data taken near the rear glass windows (see Fig. 2.1) show somewhat larger values compared to the L02 and L03 data measured near the front windows. The maximum heights reached at about one second differ by about 15%.

5.3 Development of the interaction zone in the water

Data base: void and temperature measurements In support of the dicussion, two selected void signal sets and the temperature signals are presented in Figs. 5.7a and 5.7b and in Fig. 5.8, respectively. The remarks, made on these measurements at the beginning of Section 3.3, should also be considered here.

5.3.1 Progression of the steam/liquid interface

Figure 5.9 illustrates the axial and radial progression of the interaction zone into the water evaluated from void data as well as from film pictures. The contours of the steam/liquid boundary lines show that in PM12, like in the other two tests, the melt penetration into the water produced a relatively narrow channel composed of melt, steam, and water.

Figure 5.10 gives the axial progression of interaction along the vessel axis evaluated from thermocouple data as well as from film pictures. A remarkable result in this figure is that the delay of the t/c data compared to the film data is especially large (around 0.2 s) between 0.2 and 0.5 s. This result can be explained by observations made in the films mentioned above. These show that the expansion proceeded in such a way that its centre-line temporally deviated markedly from the vessel axis. From about 0.5 s on, the delay in the the t/c data was reduced and took on values (0.1 s) that are in the same order of magnitude as in the other tests. The speed of penetration in PM12 (lower part of Fig. 5.10) was comparatively small.

The finding that the rate of penetration slowed down around 0.9 s may support the presumption, already made in Section 5.1, that the melt stream was fragmented to a large extent from that time on.

Additional conclusions are drawn on basis of void and temperature measurements in PM12: (1) the initial rise of the water went along with concentric surface waves (see

the V06 signals in Fig. 5.7); (2) steam was the dominating phase in the region near the pool centre (see the V061 - V064 signals); (3) large liquid fractions over time appeared in the region close to the vessel wall (V067 – V068 signals); i.e. it was this region where the liquid water preferrably moved up.

5.3.2 Volumes and average volume fractions resulting from the interaction

Volumes formed as a consequence of the interaction and the derived average volume fractions are shown in Fig. 5.11. The results in PM12 show the same behaviour as in the other two tests: low steam fraction and large liquid fraction due to the scattering form of initial melt release in the beginning; development of both fractions in opposite directions afterwards. The steep increase in the steam fraction at 0.43 s is accompanied by just such ones in the water level (upper diagram) and in the pressure (Fig. 5.5). As already stated, the increases are indications of a change taking place in the violence of evaporation. This change is clearly visible in the film pictures (Fig. 5.1), namely between those of 0.4 s and 0.5 s.

5.3.3 Local distributions of steam and water in the water pool

A series of graphs (Fig. 5.12) gives the distribution of steam and water in the interaction zone for various times. The upper row of the graphs, especially numbers two and three (0.23 and 0.35 s), may indicate the effect of a shower of wide-spread melt drops penetrating into the water in the initial phase. Later, from 0.50 s to 1.54 s, the progression of the interaction in the radial direction is visible; the pictures show coherent regions containing mostly steam. This result supports the above result of a large average steam fraction. After about 1.54 s, the distributions of steam and water in the zone observed vary in a wide range.

5.3.4 Jet fragmentation

We deduced from characteristics in the void and temperature data that the jet breakup length was $895 < L < 1095$ mm (L being the distance from the initial water surface). This result is in good agreement with observations made in the films. These give the impression that the melt stream, upstream of the leading edge, remained compact down to a water depth of 1100 mm all the time. From time 0.88 s on, the melt seems to be completely fragmented.

5.4 Progression of the steam-water mixture into the annular gas space

Temperature data Figure 5.13 shows the time histories of the temperatures in the gas space. The T06 thermocouple, located close to the vessel axis at r=25 mm, was destroyed by melt very early. The other thermocouples mounted in the annulus at a short distance from the melt generator housing were not affected. The T05 thermocouple, showing an extreme temperature of 124 °C, could have been influenced by radiation from a melt particle in the neighborhood. The traces of the T04 - T01 thermocouple showed a distinct halt in their rises, lasting from 0.55 s to 0.7 s. This halt corresponds to the halt seen in the PK01 and PK02 pressure measurements (Fig. 5.5) at the same time.

Void data Void signals drawn in Fig. 5.14 illustrate the conditions encountered near the vessel wall. The picture shows that "liquid" conditions lasting longer than about 0.1 s occurred only at the lowest measuring level (57 mm) whereas rather short average residence times of the liquid were mostly measured at larger heights. It is concluded from this result that liquid was passing the measuring probes as drops while the contact times are assumed to depend on the drop size as well as on the velocity of the drop/steam mixture.

Characteristics of the void data have been used to show the axial progression of the liquid in the annular compartment (Fig. 5.15). The difference in time of the "drop" line and the water level gives the quantity of lead of the water particles relative to the rise of the water surface. Extrapolation of the "drop" and "slug" lines may give an approximate time at which first water drops entered the steam venting pipes.

The advance of the water drop front with the height is given in Fig. 5.16: A remarkable result is that the progress of the water particles around the melt generator edge (r/z coordinates = 200/220 mm) was relatively slow up to 0.50 s. After that time, the front moved fast in axial direction with a very fast component in the zone near the vessel wall.

Similar conclusions can be drawn from the two series of graphs given in Figs. 5.17a and b where local distributions of steam and water in the annular gap at various times are shown. The "movement" of liquid drops and/or liquid clusters in axial and radial directions is evident in several groups of pictures.

5.5 Post test investigation

5.5.1 Water mass balance

A water loss of 287 litres was calculated from the water level decrease during the test amounting to 770 mm. On the other hand, a volume of 49 litres of water could have been evaporated by 29 kg of melt, 85 litres were found in the water separators. The difference, 153 litres of liquid water, must have been transported as droplets by the steam out of the test facility. The larger loss of water found in PM12 compared to that of other tests is due to the larger melt mass released in this test.

5.5.2 Gas analysis

The pressure in the sample bottles amounted to 0.025 to 0.030 MPa at the time of analysis, three hours after the test. The low pressure can be explained by condensation of steam in the meantime. In the mass spectrometer analysis, air was found as the only component. Hydrogen was not found within the accuracy of the analysis.

5.5.3 Melt mass balance and sieve analysis

As mentioned, a fragment mass of 29 kg containing a relatively large fraction of iron was found after the test (see Table 5.1). Investigations undertaken in this matter revealed that about 44.6 instead of 40 to 41 kg of thermite powder had been filled into the crucible. This means that the reaction provided extra masses of about 2 kg of iron and 2 kg of alumina. The extra mass of iron could not be retained in the iron cavity. As a consequence, the overflowing iron eroded the edges of the cavity and more than the two extra kilograms of iron was released.

The post-text examination gives the following results:

- a total mass of 28.98 kg was recovered as fragments,
- 15.3 kg of iron remained in the generator,
- a mass of 1.1 kg of alumina was deposited in the melt trap mounted in the gas line that connected the melt generator and the gas reservoir (see Fig. 2.1).

Summing up the three fractions gives 45.4 kg. Additionally, about 4 kg of the ceramic liner had been molten off. If this mass is added to the mass of thermite powder filled in, we get a mass of 48.6 kg. The difference in mass, 48.6 kg – 45.4 kg = 3.2 kg, is the mass that could not properly be collected. This was the material

- that froze at colder surfaces, e.g. the glass windows and the surface of the melt generator housing,

- that was transported by steam through the venting pipes and deposited, as a fine dust, throughout the test container,
- that remained as suspended fine particles in the water.

The fragments collected from the water separator, the fragment catcher, and the vessel bottom were weighed and sieved, each portion separately. In another pass of examination, the fragments that contained iron inclusions were separated by use of a strong magnet. Detailed results are given in Table 5.1.

5.5.4 Chemical analysis

The chemical analysis was made taking randomly samples from the fragments collected at the water separators, the fragment catcher and the basis of the test vessel. The results of the analysis are given in Table 5.2.

The fractions of the magnetic (iron) and nonmagnetic (oxide) material were scaled according to the ratio of the masses found at the various locations. The values in the

Table 5.1 PM12; sieve analysis of fragments broken down in the sites of recovery

Location	Quantity		Magnetic fraction	Non- magnetic fraction	Total
Water separators	Mass	g	2252.8	1210.2	3463.0
	Mass mean diam.	mm	4.42	2.89	3.89
	Sauter mean diam.	mm	1.59	1.32	
	Total surface	m^2	2.308	1.891	4.199
Fragment catcher	Mass	g	14866.7	3750.7	18617.4
	Mass mean diam.	mm	11.78	10.54	11.53
	Sauter mean diam.	mm	7.16	6.42	
	Total surface	m^2	3.354	1.205	4.559
Basis of test vessel	Mass	g	5501.8	1399.6	6901.4
	Mass mean diam.	mm	10.28	14.0	12.99
	Sauter mean diam.	mm	6.9	8.05	
	Total surface	m^2	1.055	0.359	1.414
Total	Mass	g	22621.3	6360.5	28981.8
	Mass mean diam.	mm	10.68	9.85	10.5
	Sauter mean diam.	mm	5.49	3.00	
	Total surface	m^2	6.717	3.455	10.172

"total/averaged" line were calculated taking into consideration the mass ratio of the material analysed to the material found.

Table 5.2 Test PM12, chemical analysis. The results are broken down in the sites of recovery

Location	Material collected g	Material analysed g	Metal (iron) %	Oxides (total) %	Al_2O_3 %	Fe_2O_3 %	MgO %	Other Oxides %
Water separators	3463	1397	12.00	88.00	83.10	11.50	2.20	3.20
Fragment catcher	18617	6753	10.80	89.20	88.00	8.80	0.15	3.05
Bottom of test vessel	6901	1551	11.80	88.20	86.90	10.30	0.12	2.68
Total / average	28981	9701	11.10	88.90	87.10	9.40	0.44	3.06

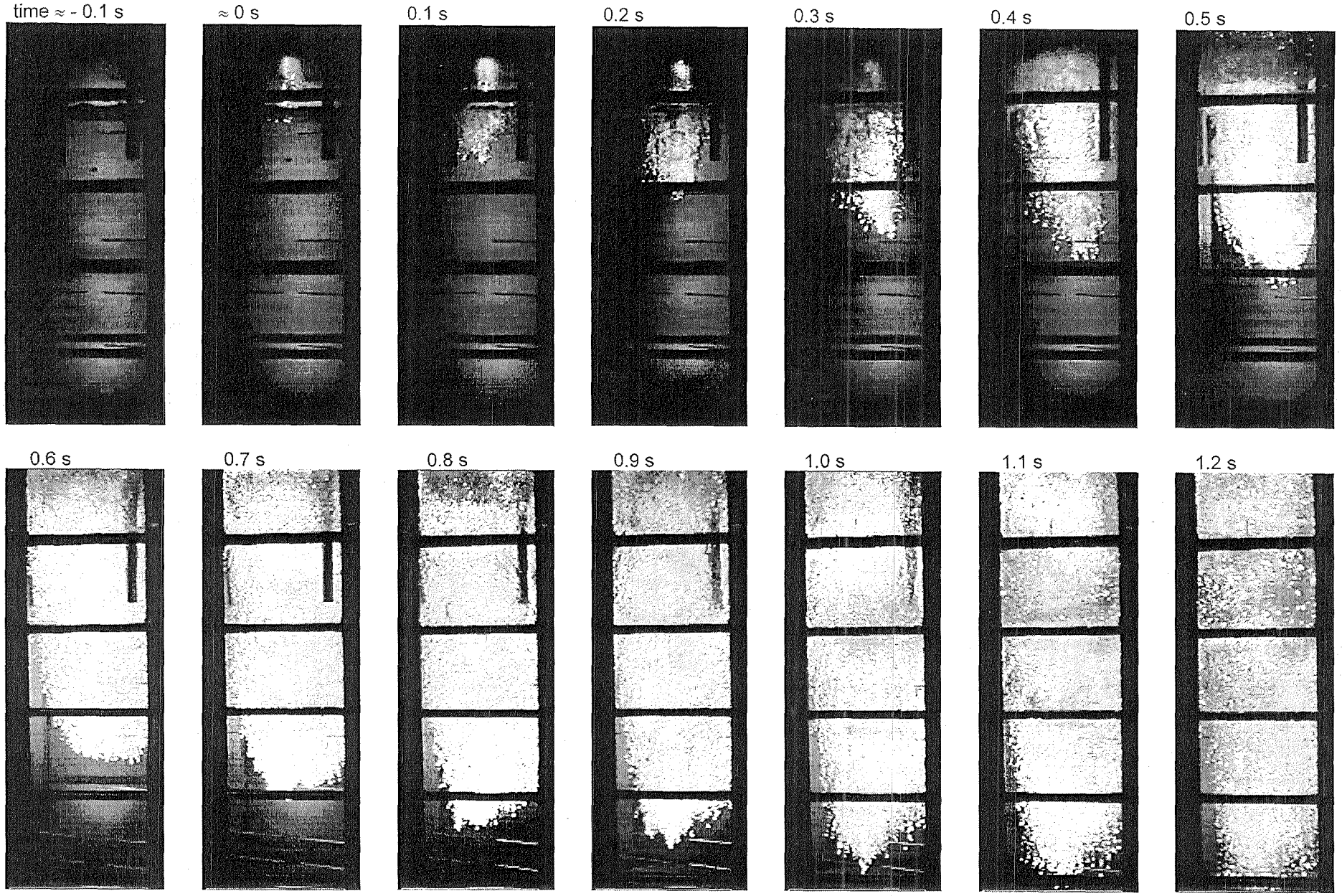

Fig. 5.1 Development of the interaction zone in PM12 shown by pictures of the video film.

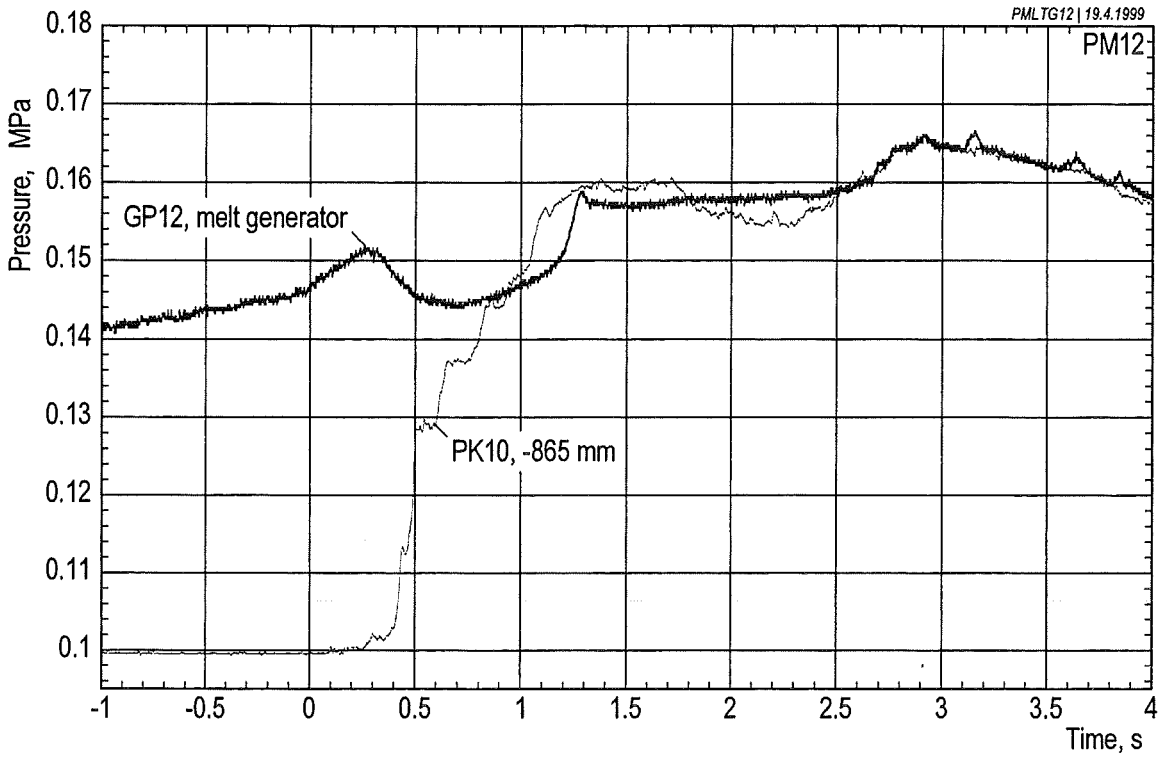

Fig. 5.2: Pressures inside and outside of the melt generator.

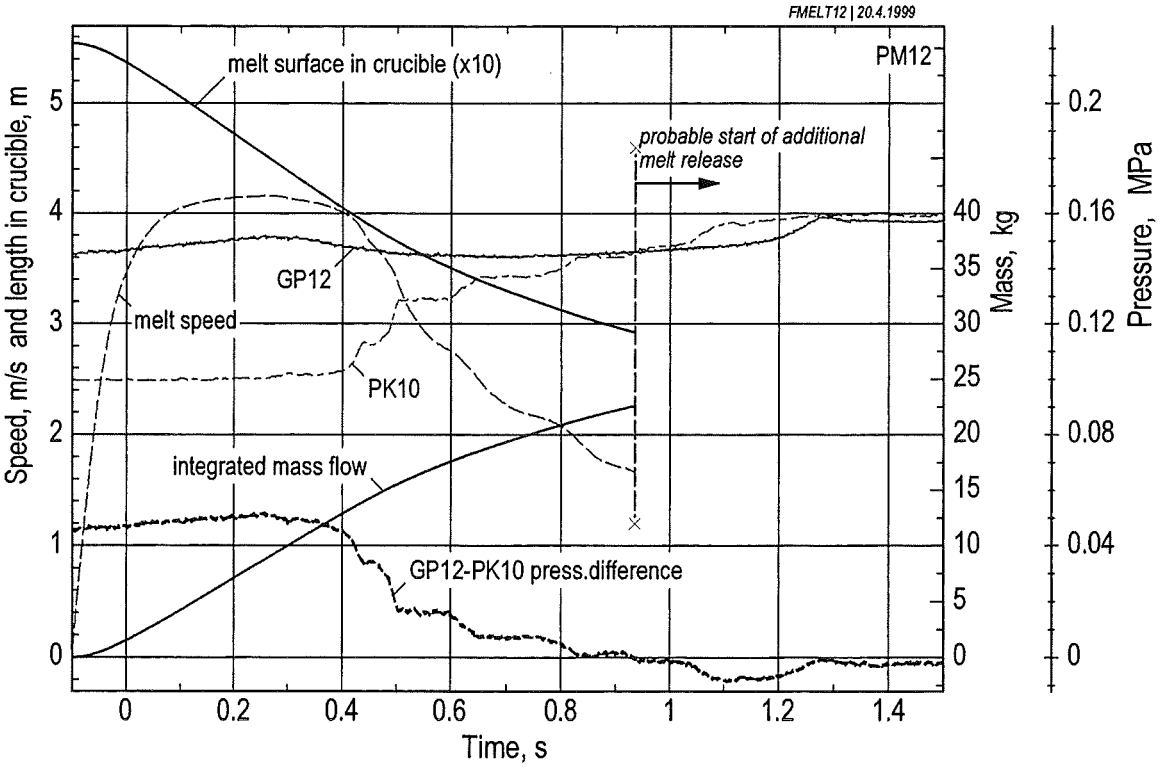

Fig. 5.3: Melt flow rate calculated on basis of the pressure difference.

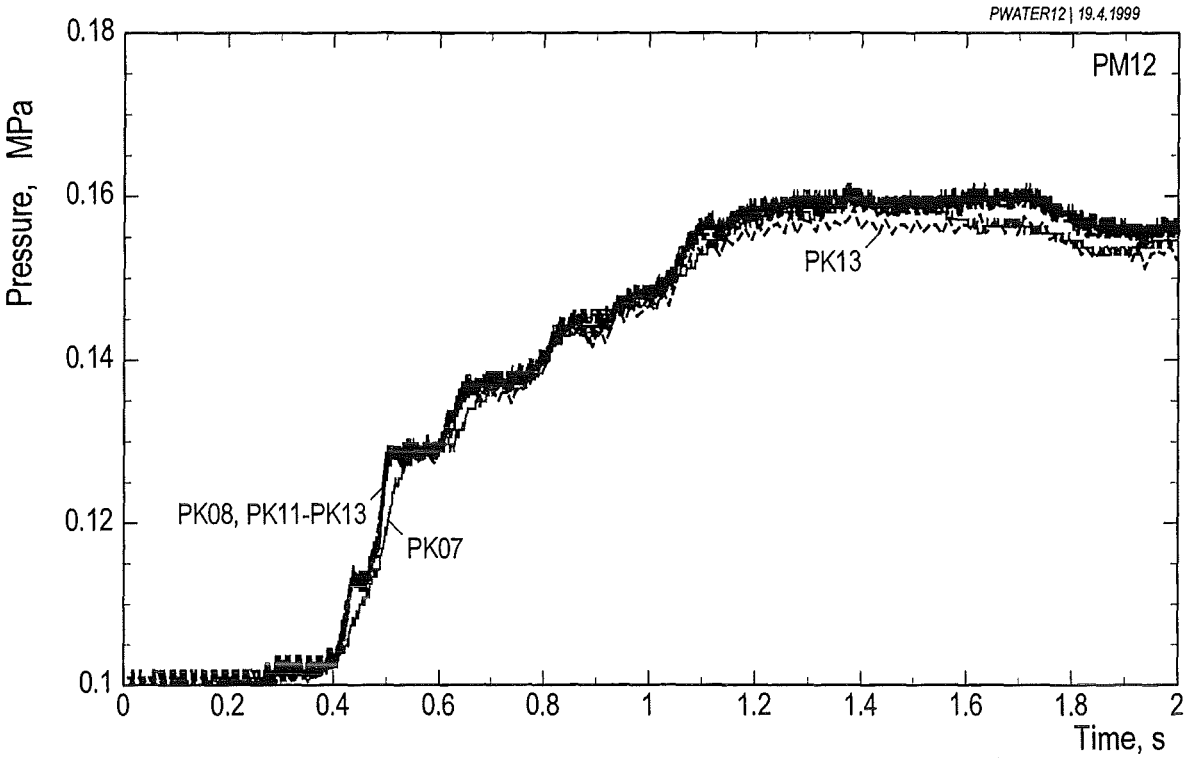

Fig.5.4. Pressure data obtained from transducers located in the water pool.

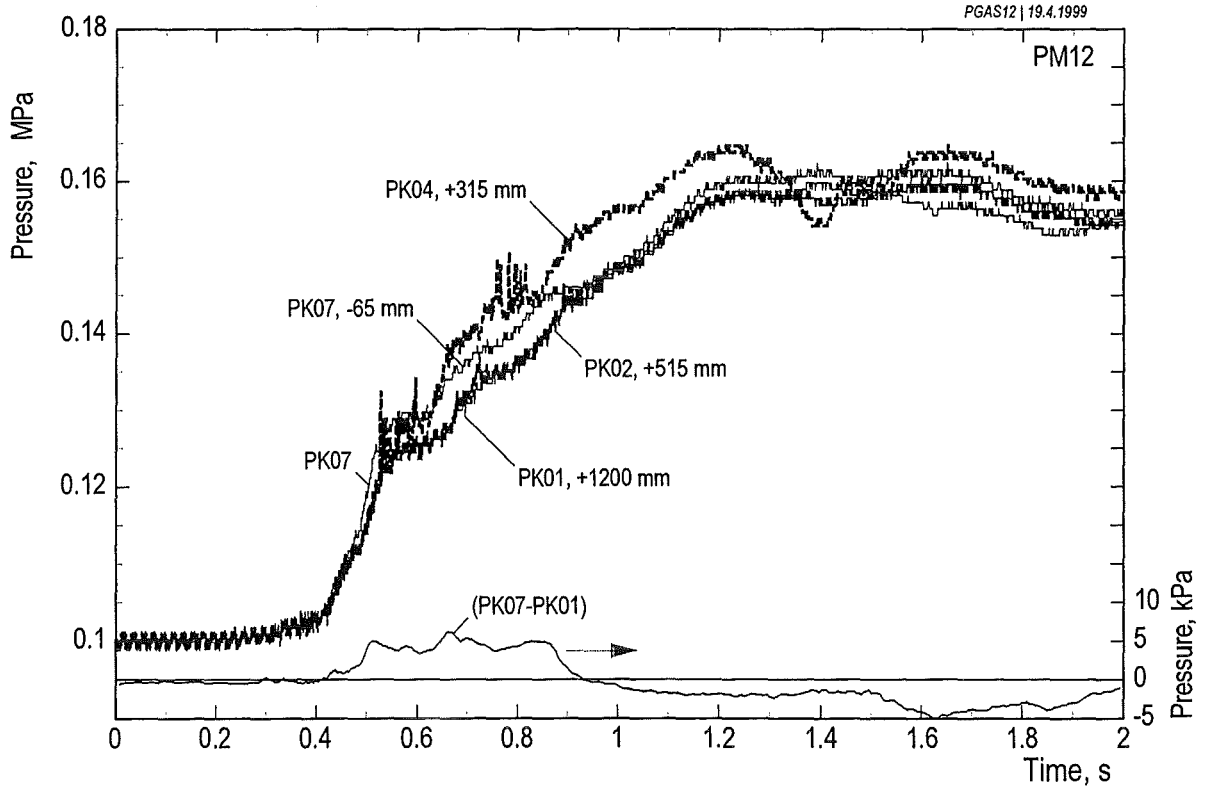

Fig. 5.5. Pressure data obtained from transducers located in the gas compartment (PK01-PK04) and a short distance (45 mm) below the initial water level (PK07), respectively.

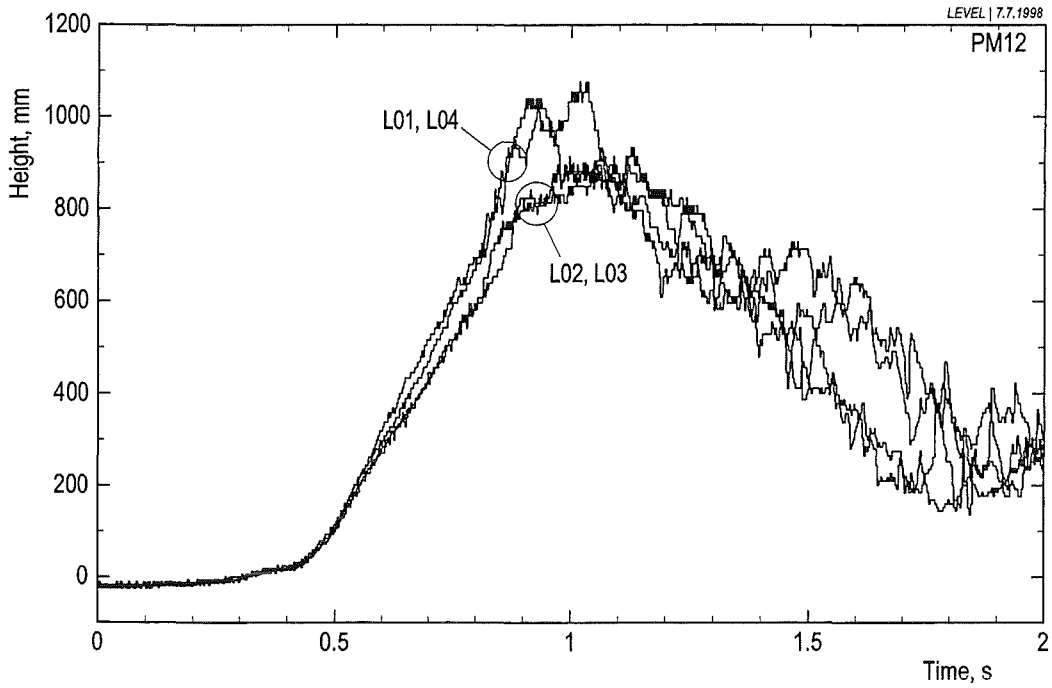

Fig. 5.6: Water level measurement.

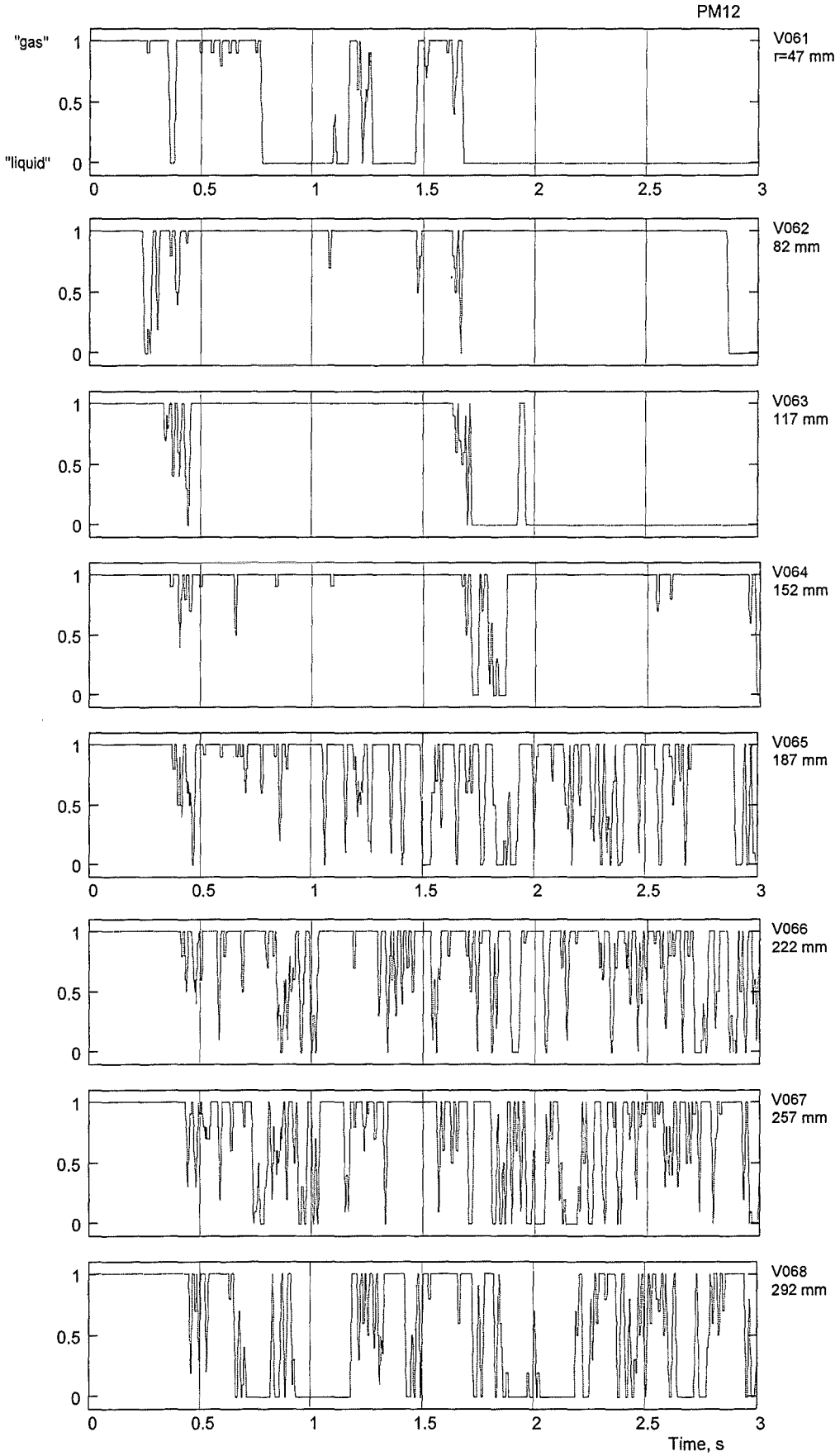

Fig. 5.7 (a): Void signals of the V06 measuring lance. Smoothed signals (cf. Fig. 2.6) have been chosen to obtain a better time resolution. The measuring tips of the void probes were located 77 mm above the water surface.

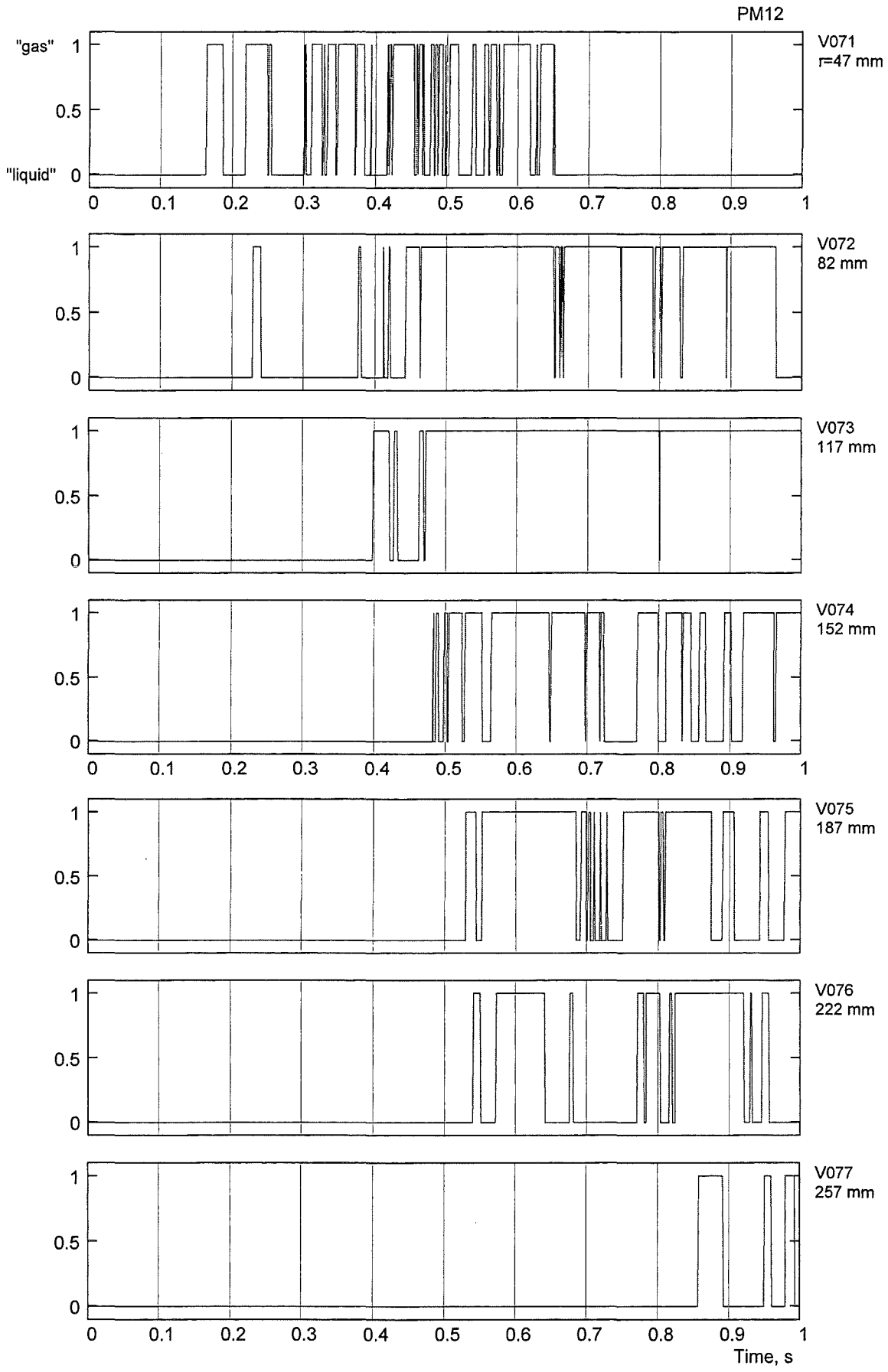

Fig. 5.7 (b) Full signals of the V07 measuring lance. The measuring tips of the void probes were located 87 mm below the water surface.

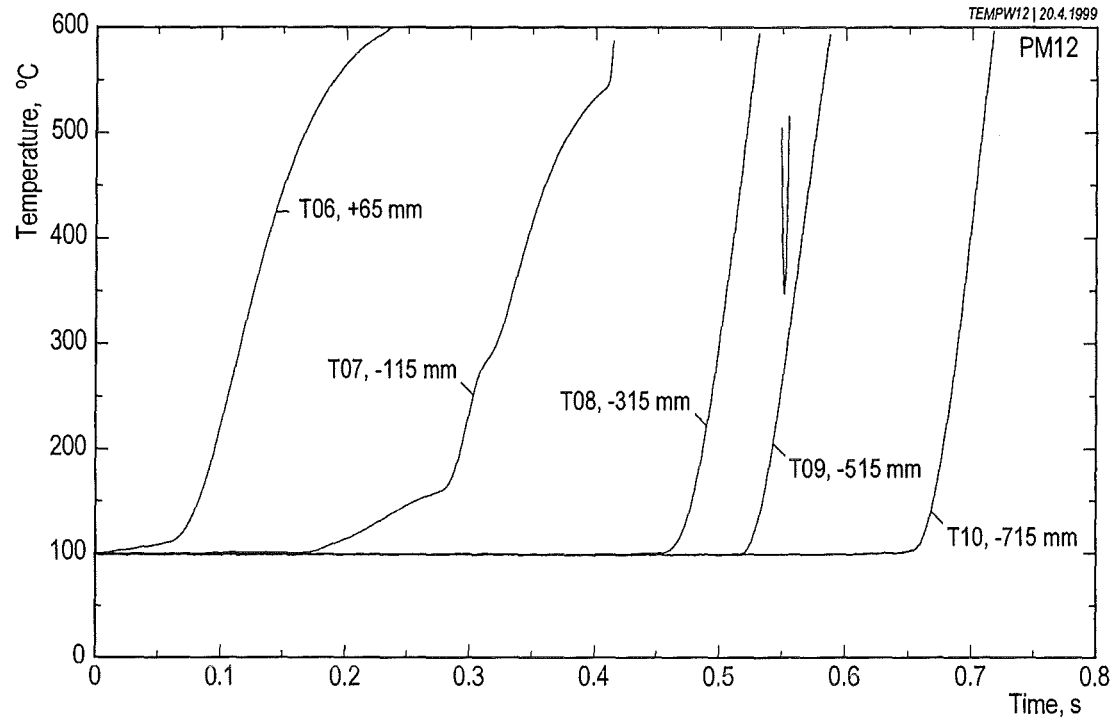

(a) upper part of the water pool

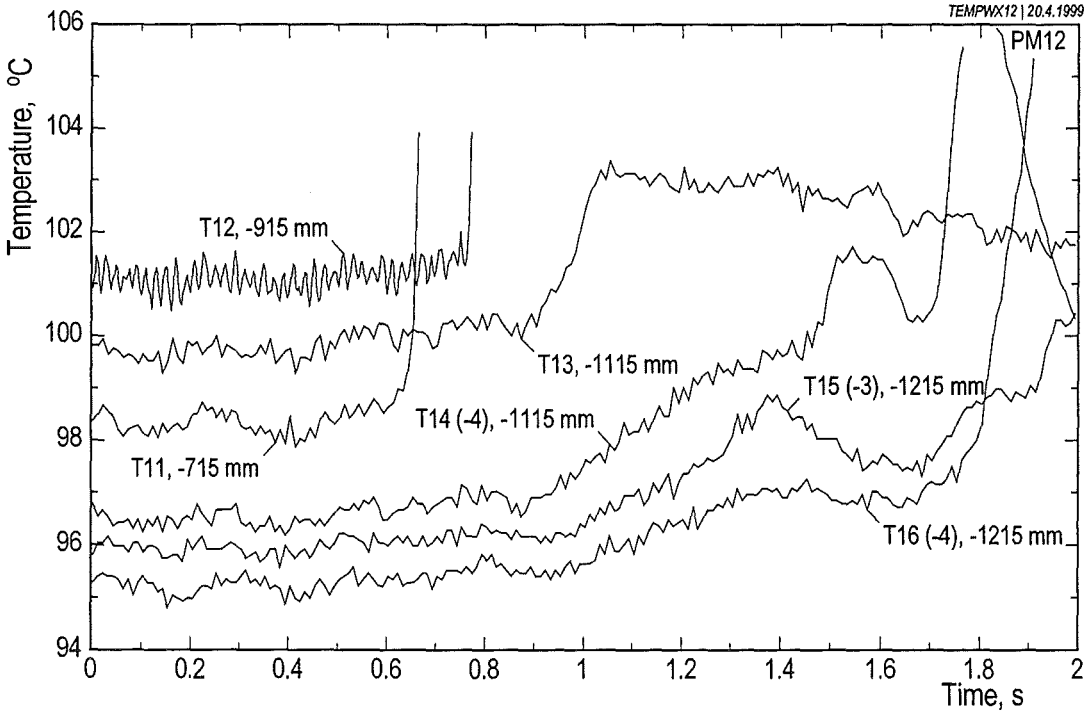

(b) lower part of the water pool

Fig. 5.8: Temperatures measured in the water pool (T07 – T16). T06 signal was measured 77 mm above the initial water level.

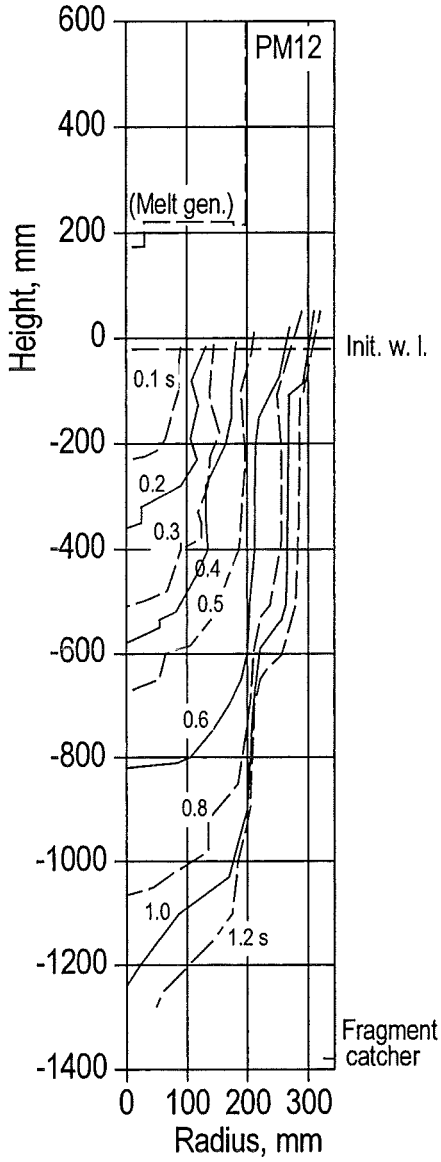

Fig. 5.9 Progression of the interaction zone into the water with the time as a parameter.

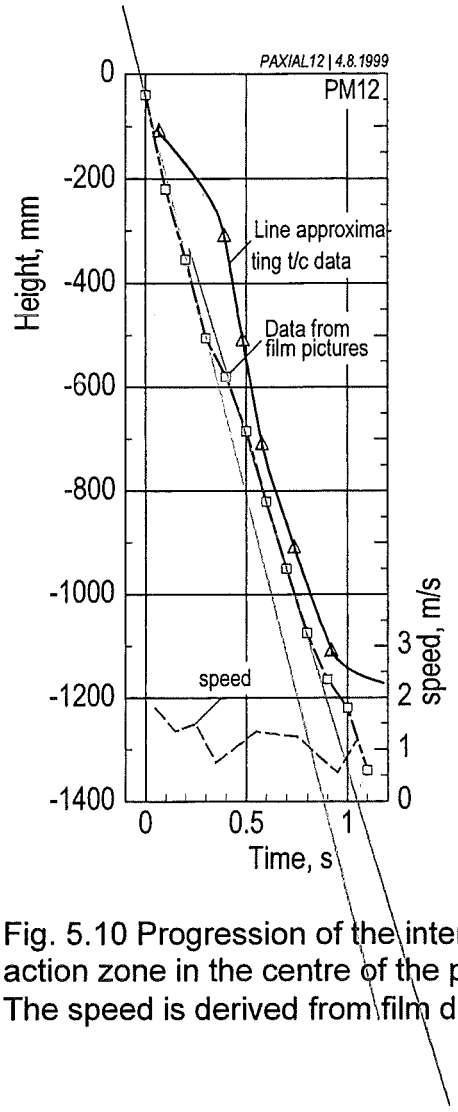

Fig. 5.10 Progression of the interaction zone in the centre of the pool. The speed is derived from film data.

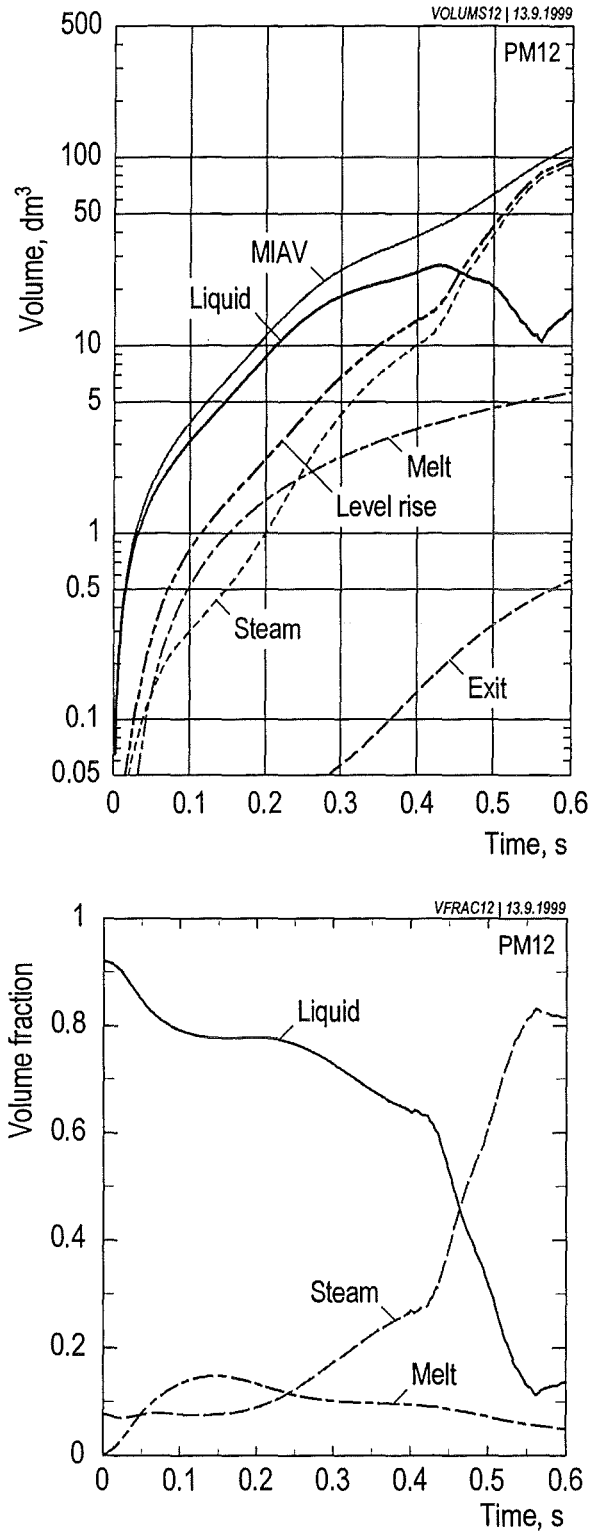

Fig. 5.11 Volumes resulting from the interaction (MIAV=multiphase interaction volume; Exit= volume of the evaporated part of water; volume due to level increase) and partial volumes of the interaction zone (steam, liquid, and melt) are shown on top, average volume fractions of the three components inside the interaction zone at the bottom.

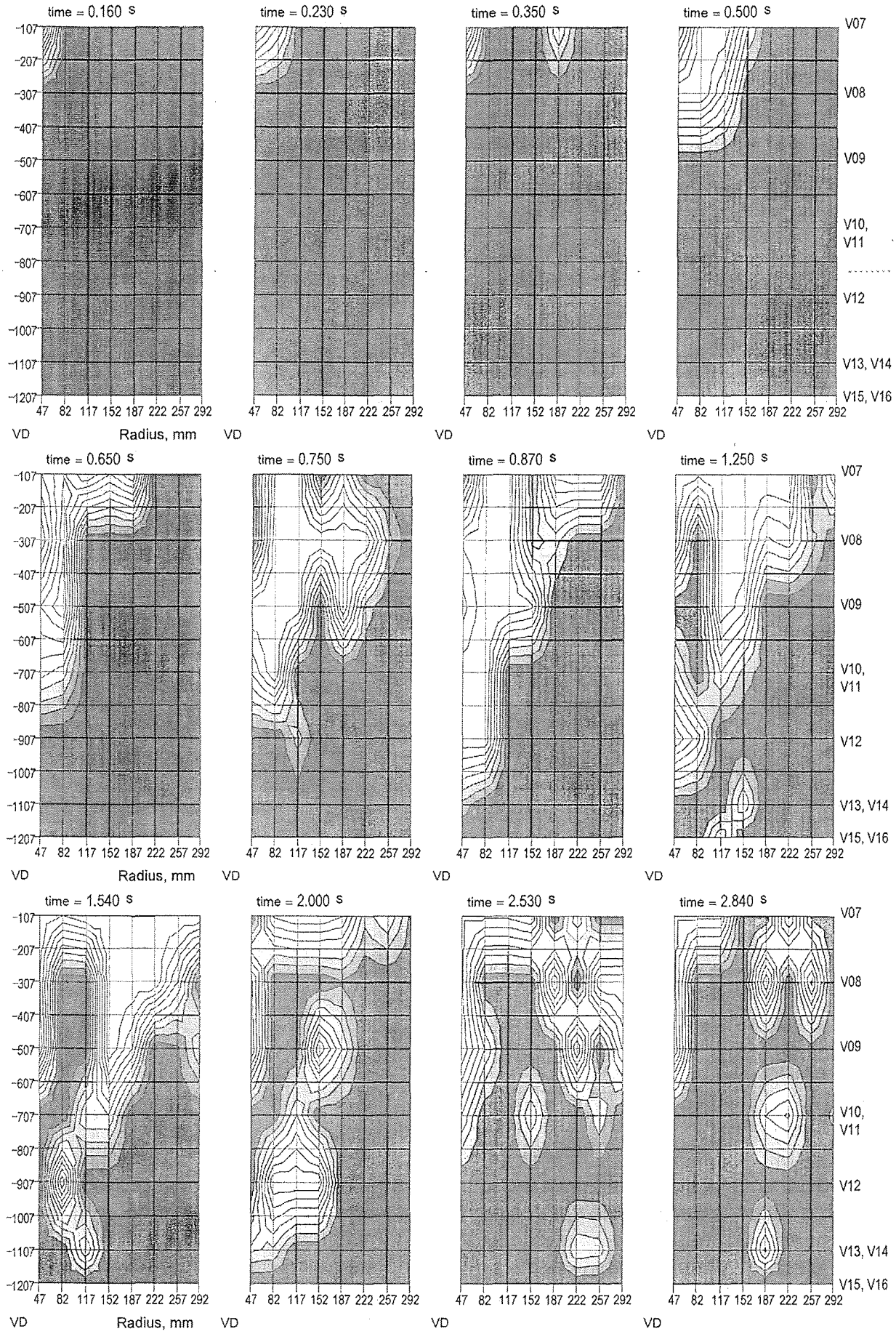

Fig. 5.12 Distribution of steam and water in the pool in PM12 at various times (white area=100% steam; dark =100% water). Distance between fraction lines: 0.125

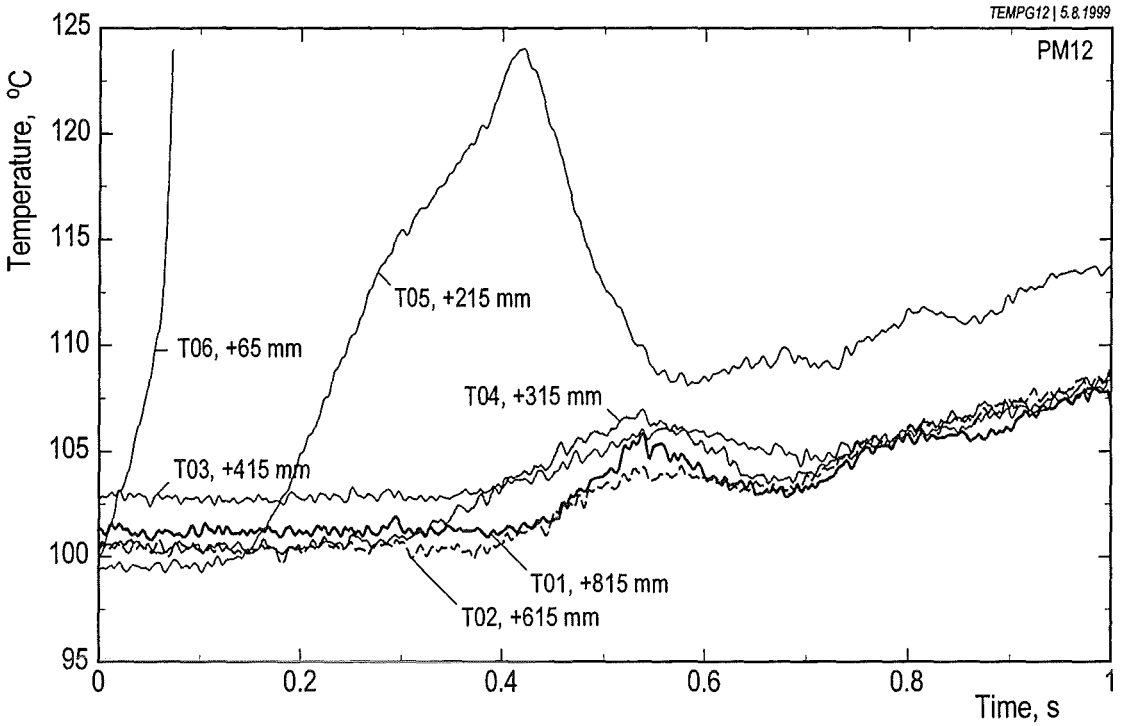

Fig. 5.13 Temperatures measured in the freeboard volume (T06) and in the annular gas compartment.

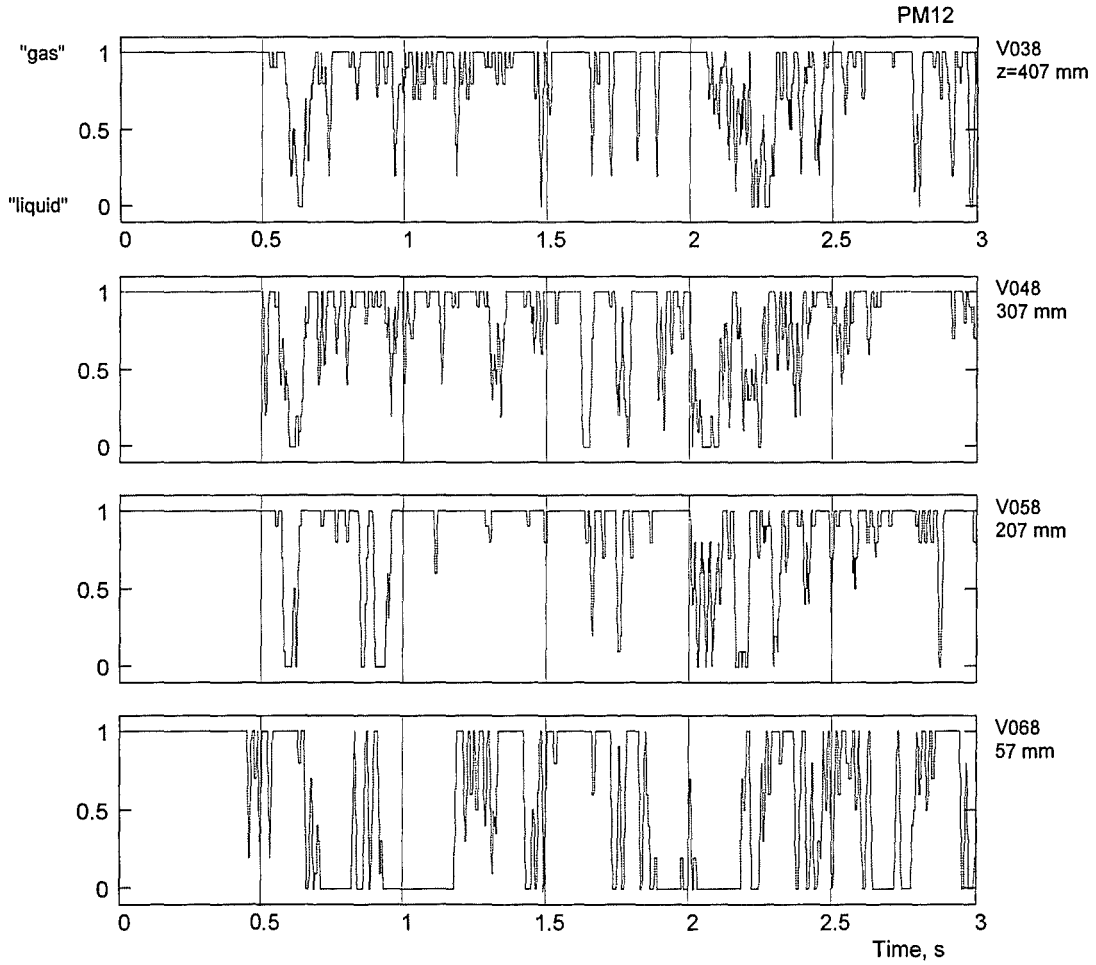

Fig. 5.14 Void signals from the freeboard volume (V06) and the annular gas compartment at various heights. The measuring tips were close to the test vessel wall. The signals were treated like those shown in Fig. 2.6.

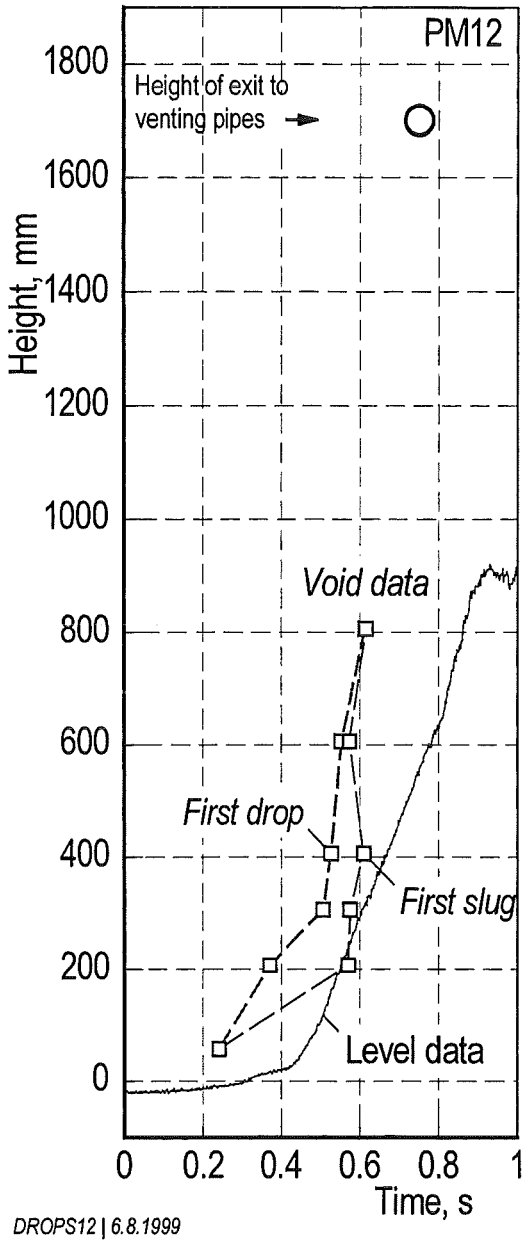

Fig. 5.15 Penetration of water into the annular gas compartment versus time compared with the water level rise.

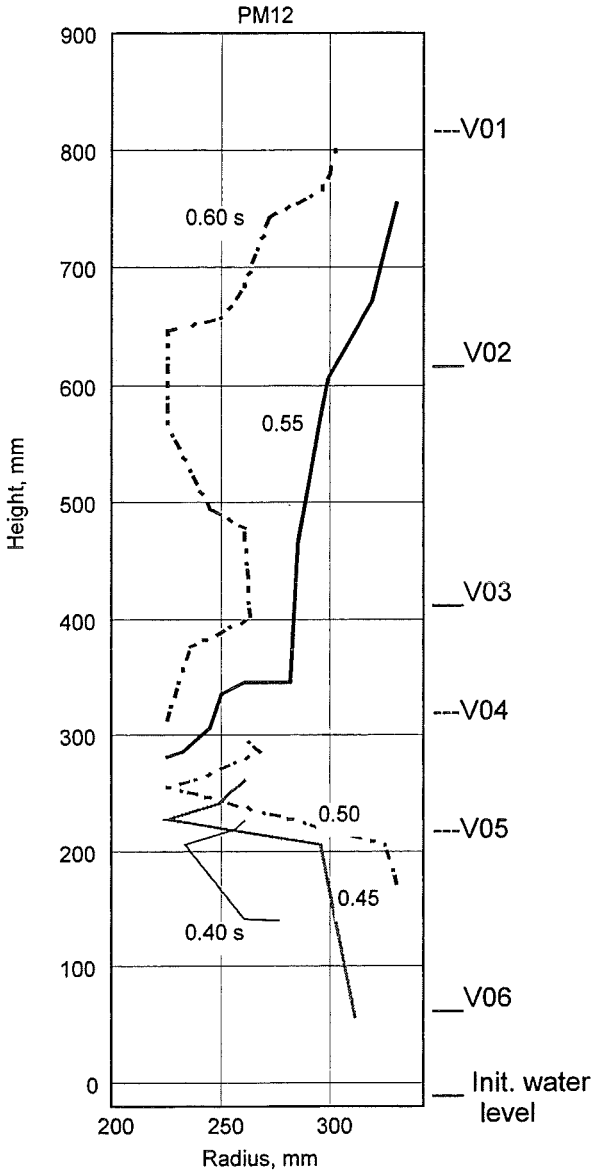

Fig. 5.16 Progression of the water front (drops and slugs) into the annular gas space shown with the time as a parameter.

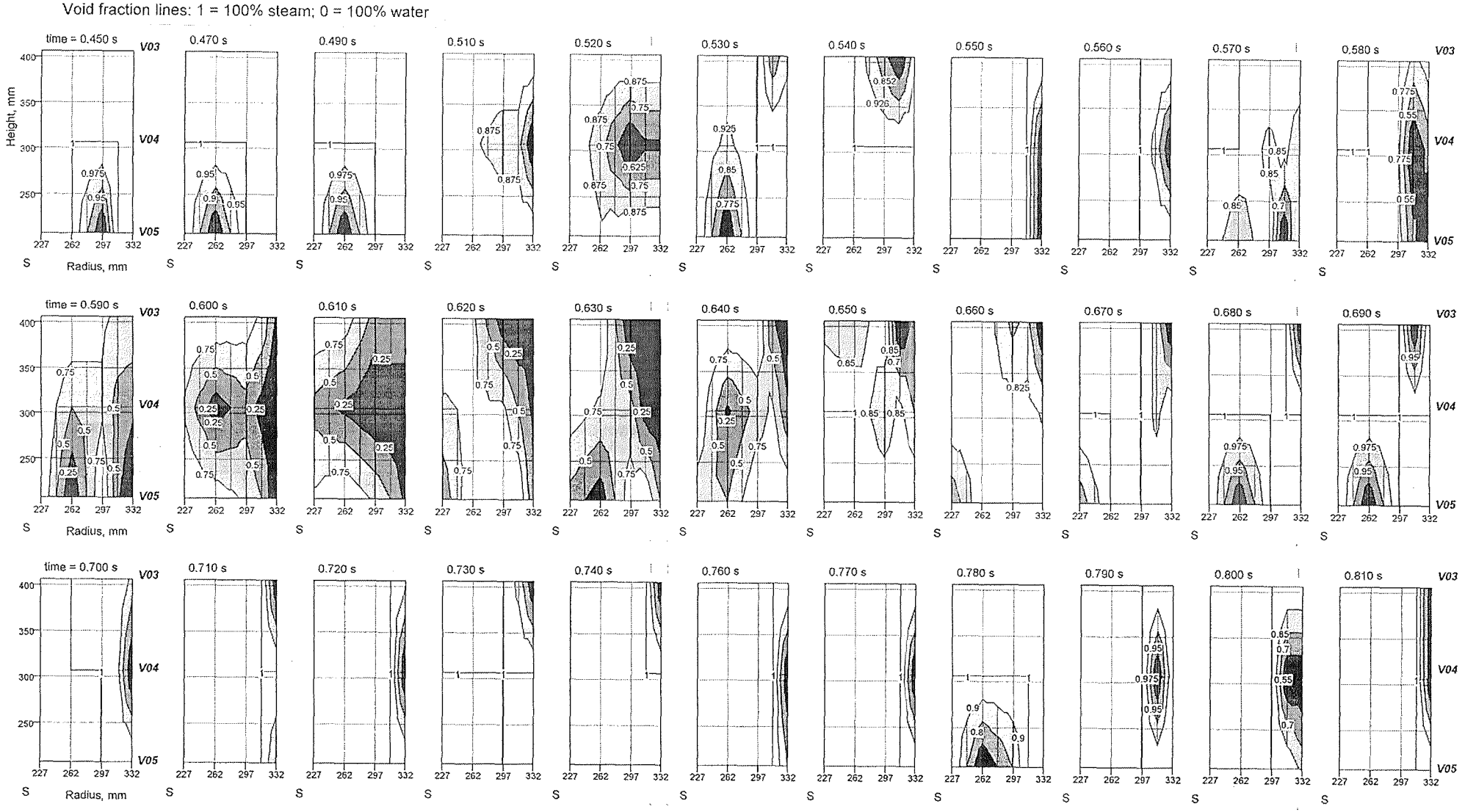

Fig. 5.17 (a): Distribution of steam and water across the annular gas compartment between 207 and 407 mm height. General time step between pictures:0.01 s. For the missing times, e.g. 0.480 s, no water was measured.

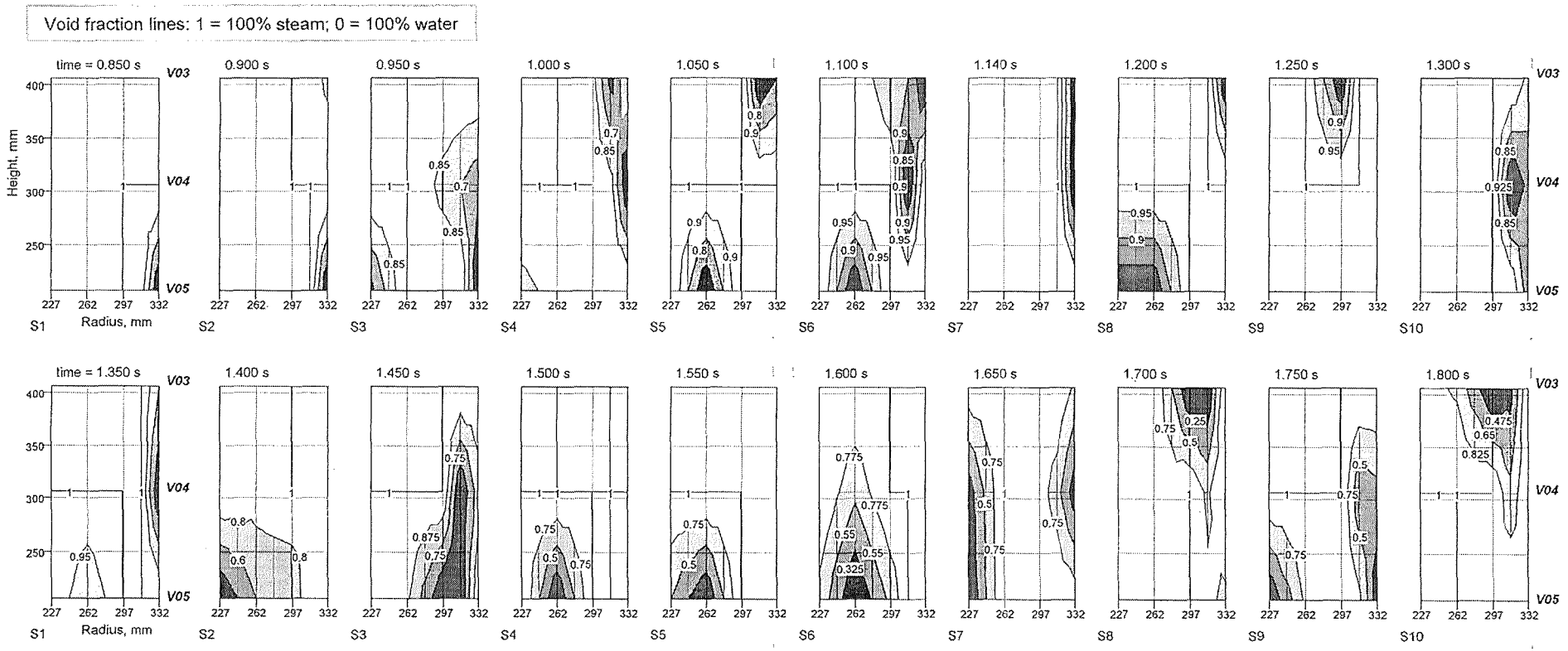

Fig. 5.17(b) Distribution of steam and water across the annular gas compartment between 207 and 407 mm height (continued). General time step between pictures: 0.05 s.

6 COMPARISON OF THE RESULTS

To begin with a preliminary remark on the findings so far: Differences as stated before in the results of the three tests obviously came from uncertainties in the preparation of the test and/or were due to fortuity in the starting procedure. Therefore, special attention is paid to these items in this chapter in which the most significant results are compared.

6.1 Pressures

The conditions at the start of melt release (i.e. around zero time) in each test were very much determined by the time history of the pressure in the melt generator documented by the GP12 traces in Fig. 6.1. The comparison shows that melt release in test PM14 began with the largest pressure because: (1) the initial GP12 pressure level was slightly increased at the time (≈ -2 s) when the pressure ramp was set; the increase was possibly due to the predeeding reaction of the adhesive material mentioned, (2) the following increase, due to heating up of the crucible atmosphere, was larger than in the other two tests. Obviously, the larger pressure difference (see boottom of Fig. 6.1) led to a larger speed of the ejected melt as shown by the calculation (Fig. 6.2) and to an earlier rise in the pressure due to interaction than in the other tests (see PK11 traces). The following decrease in the pressure difference, due to melt release, occurred earlier in PM14, too, so that from about 0.4 s on, in all tests, an almost congruent decline of the pressure difference took place. It was also in PM14 where the maximum pressure was measured in the interaction zone. After the end of melt release, the difference in the PK11 pressures was very reduced.

The pressures measured in the gas space and in the water pool, given in Figs. 6.3 and 6.4, respectively, were similar in behaviour as regards the measurements in the same test as well as in the three tests. The differences between the tests, which are in fact not significant, can be assigned to the different conditions at the start of melt release as mentioned.

6.2 Steam flow

The onset of significant steam flow (Fig. 6.5) occurred in PM13 and PM14 at the same time, while the initial increase was less steep in PM13. An explanation for this can be found in the slightly different starting conditions of melt release mentioned above. The first steam flow maxima were reached in both tests at about the same

time. After a period of almost constant flow rate, irregular break down in the signals occurred in both tests from times 1.1 to 1.3 s on. The flow disturbances (caused by water drops carried with the steam), whose pattern was similar, comprised only two of the four venting lines in both tests.

6.3 Rise of water level

Comparison of the water level measurements is made in Fig. 6.6. It was in PM14 where the first significant level rise as well as the largest increase occurred.

6.4 Development of the interaction zone

The different driving pressures established at the start of melt release (which increased from PM12 to PM14, see Table 2.2) led to different rates of melt penetration into the water, in axial as well as in radial direction. This result can be taken from the boundary lines shown in Fig. 6.7. The penetration rates resulted in growth rates of the essential volume, i.e. the volume of the interaction zone, which increased from PM12 to PM14 (Fig. 6.8).

The film pictures show, on closer examination, that the progression of the interaction zone in axial direction occasionally occurred with small temporary offsets to the vessel axis. Obviously, these resulted in small delays in the local detection of steam by the void probes.

Another important result is that the average volume fractions (Fig. 6.9, bottom) behave rather similar in all tests. The liquid fractions, which started from large initial levels, decreased gradually and approached values around 50 ±10 % after 0.4 – 0.5 s. The time histories of the steam fractions, which started from low levels, showed steep individual increases which can be correlated to sudden increases in boiling intensity. The times when these increases started differ from test to test (0.15, 0.27, and 0.43 s in PM14, PM13, and PM12, respectively). The times seem to be the shorter the larger the initial penetration speed was. Coherent areas of large steam fractions were identified in each test by the evaluation of void probes after these times.

6.5 Sieve analysis

Comparison of the sieve analyses (Fig. 6.5) shows that the particle size distribution was similar in all tests.

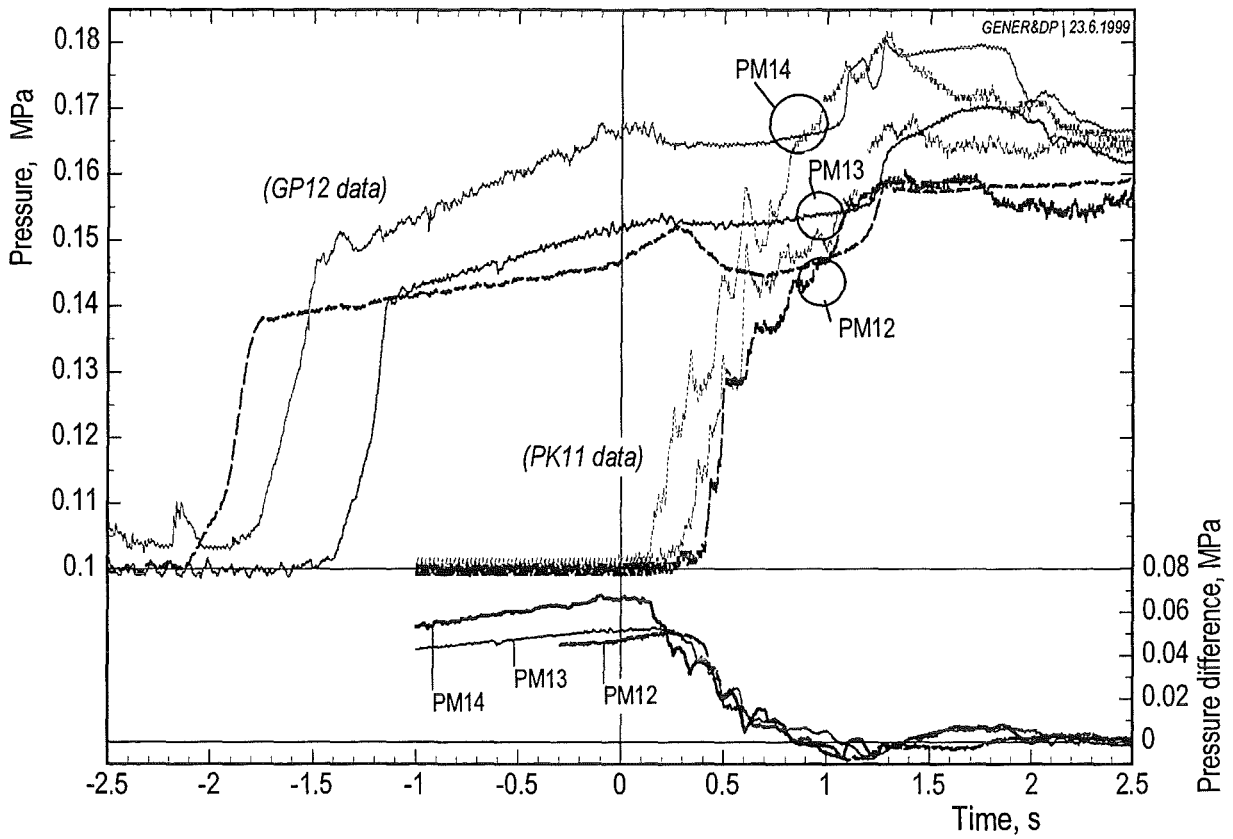

Fig. 6.1 Pressures determining the melt release: GP12 (melt gen.), PK11 (water pool at –1065 mm), and the pressure difference across the nozzle tube.

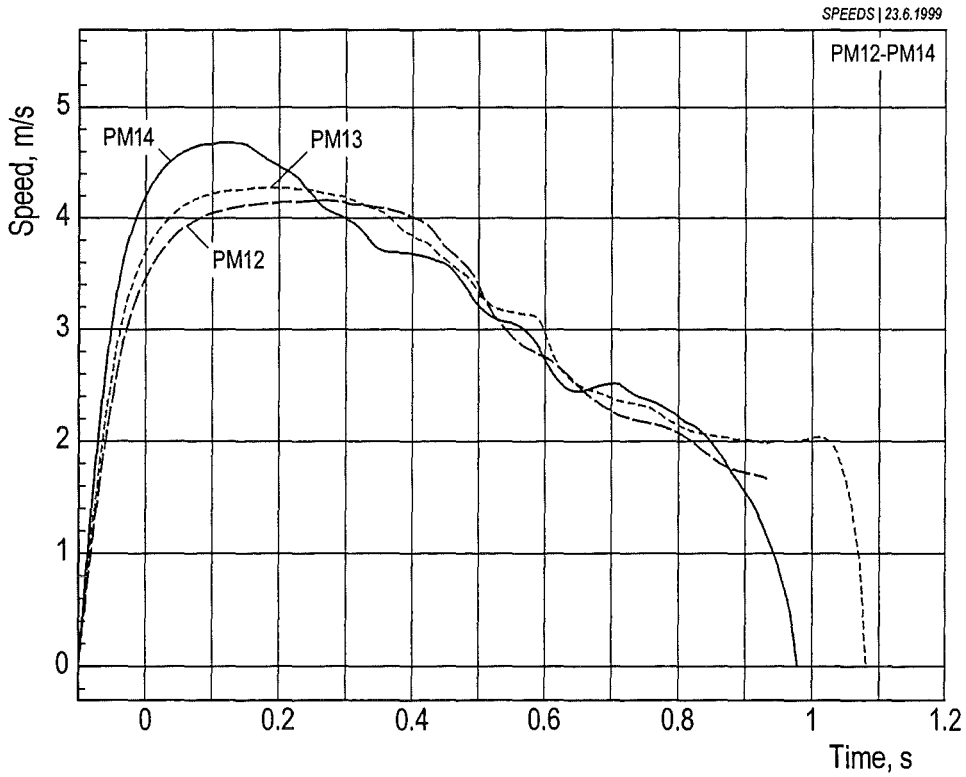

Fig. 6.2 Speeds calculated for the melt flow in the nozzle pipe

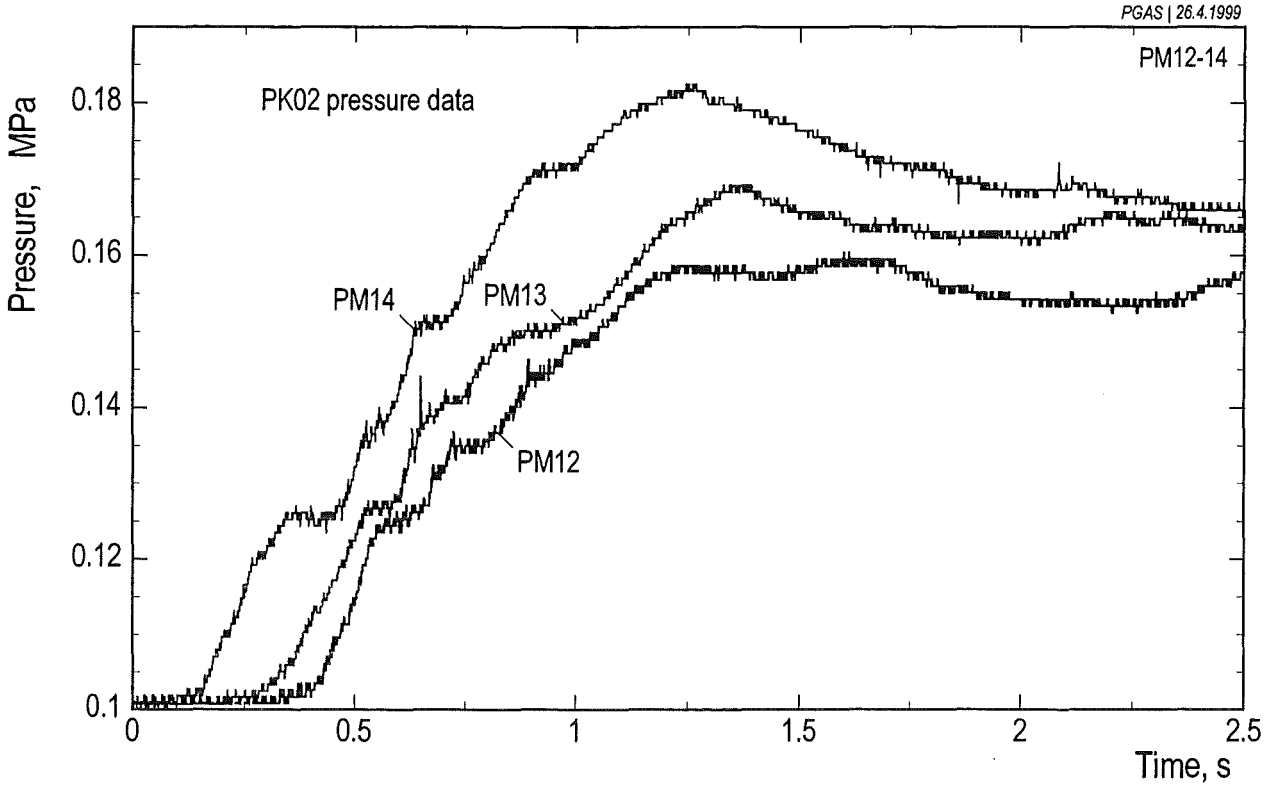

Fig. 6.3 Pressure data obtained in the gas space at 515 mm height.

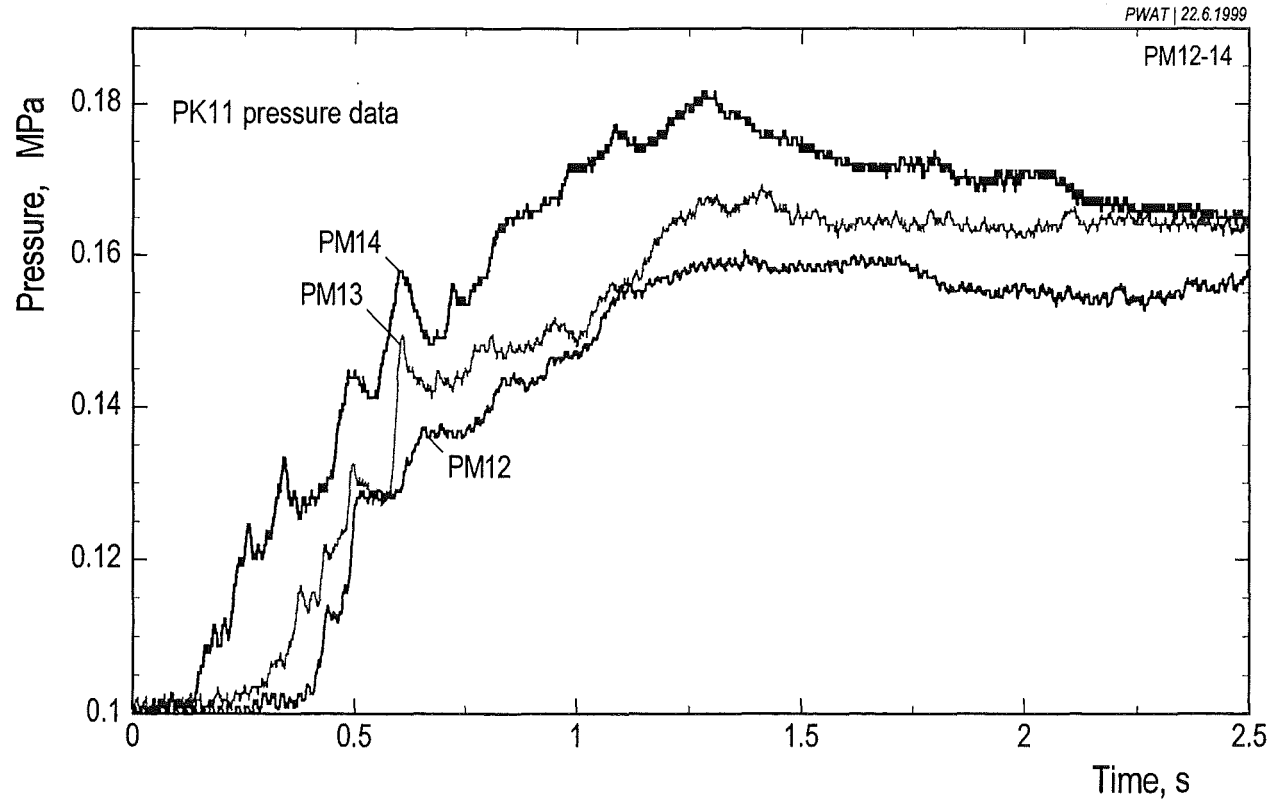

Fig. 6.4 Pressure data obtained in the water at -1065 mm height.

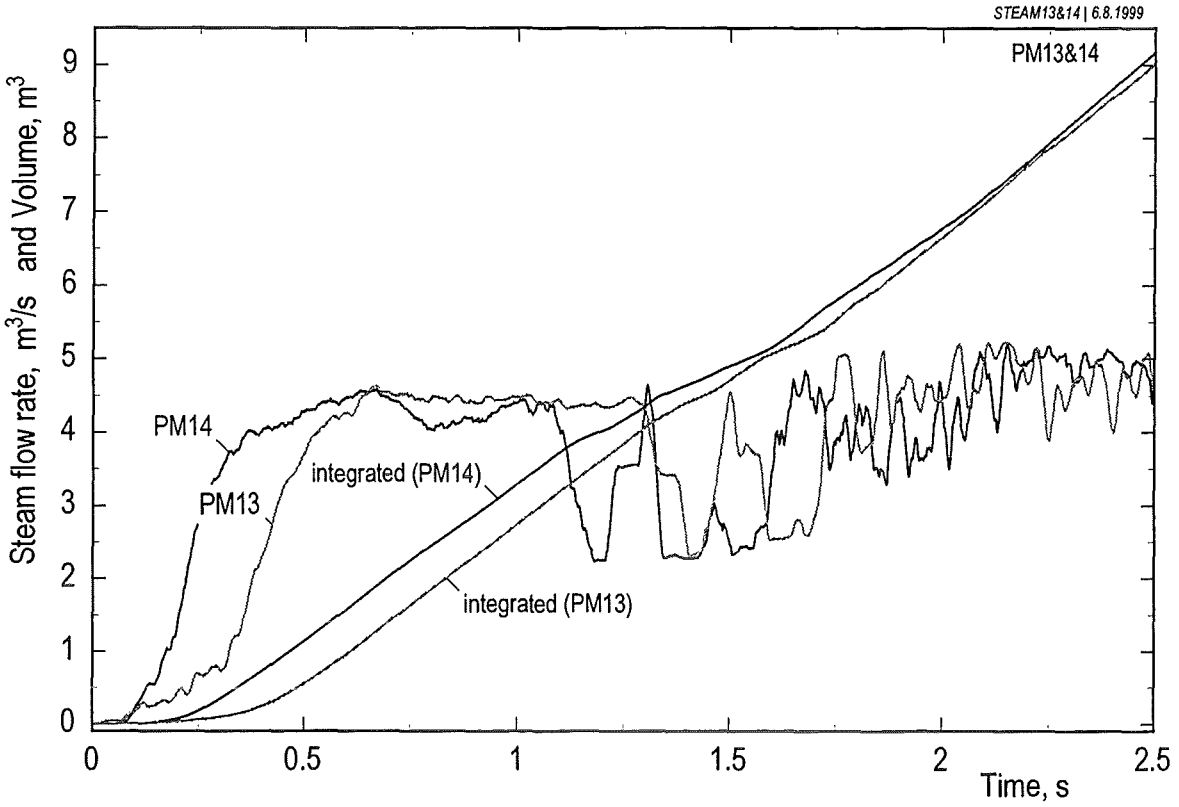

Fig. 6.5 Steam flow rates and the time integrated steam volume.

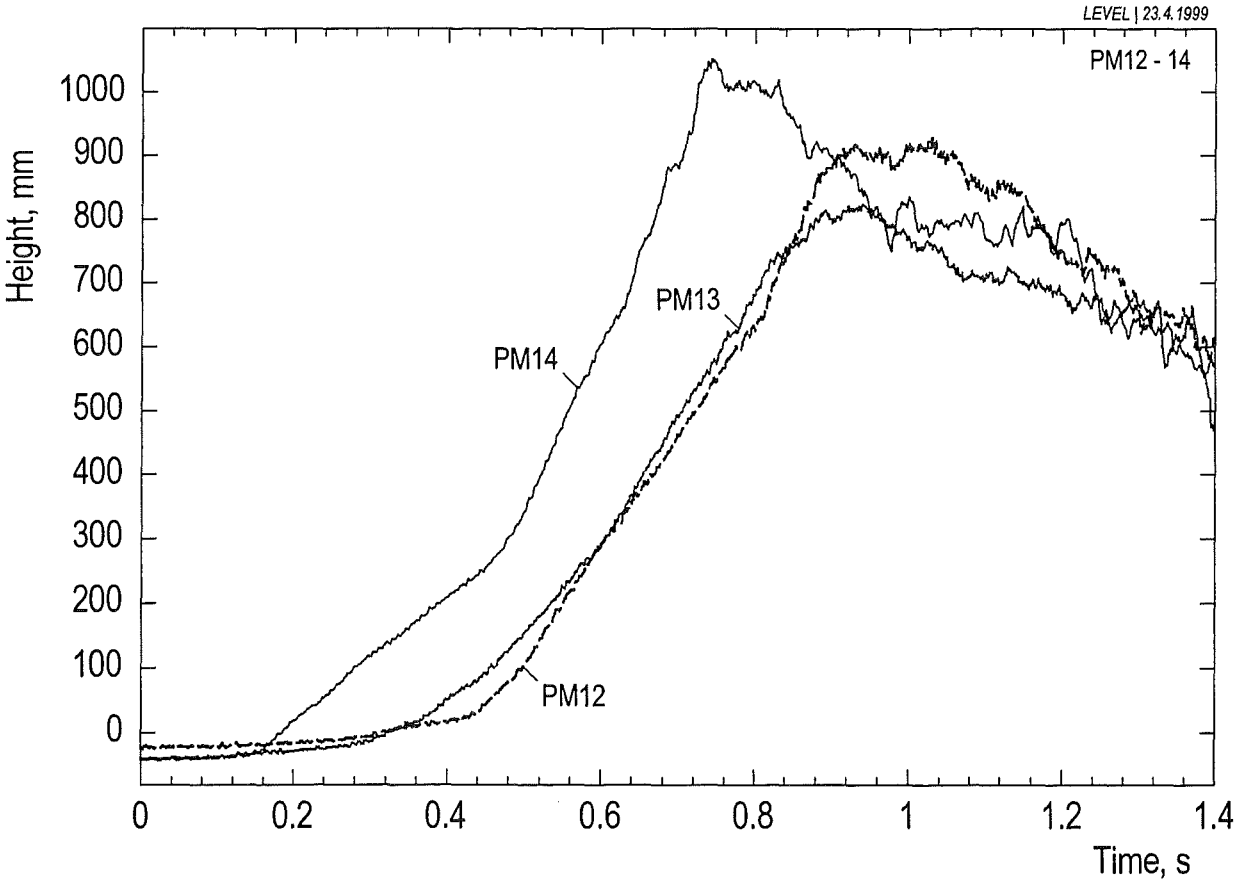

Fig. 6.6 Water level measurements; the data have been shifted so that the curves start at the respective initial water levels

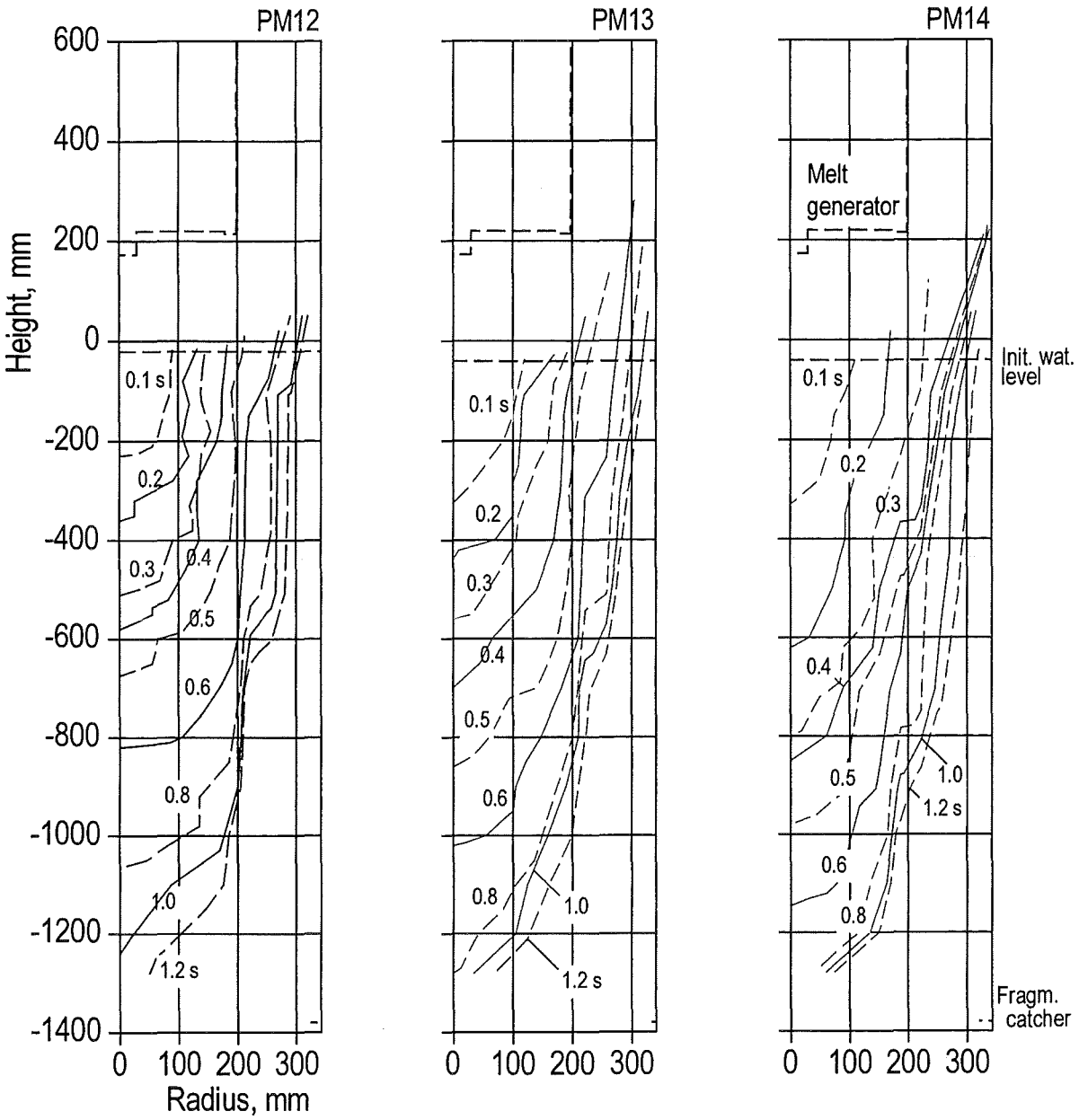

Fig. 6.7 Progression of the interaction zone into the water with the time as a parameter.

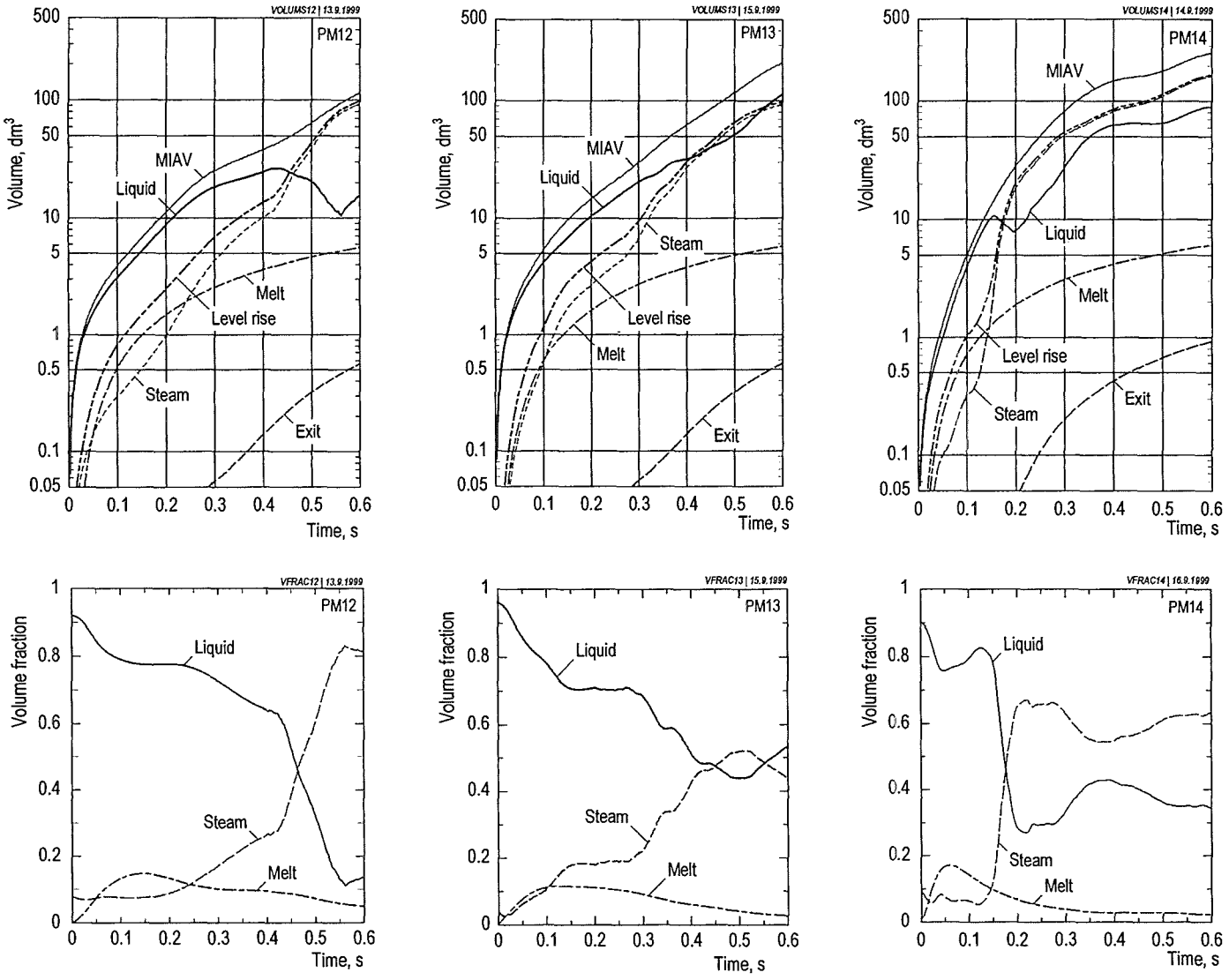

Fig. 6.8. Volumes resulting from the interaction and average volume fractions inside the interaction zone

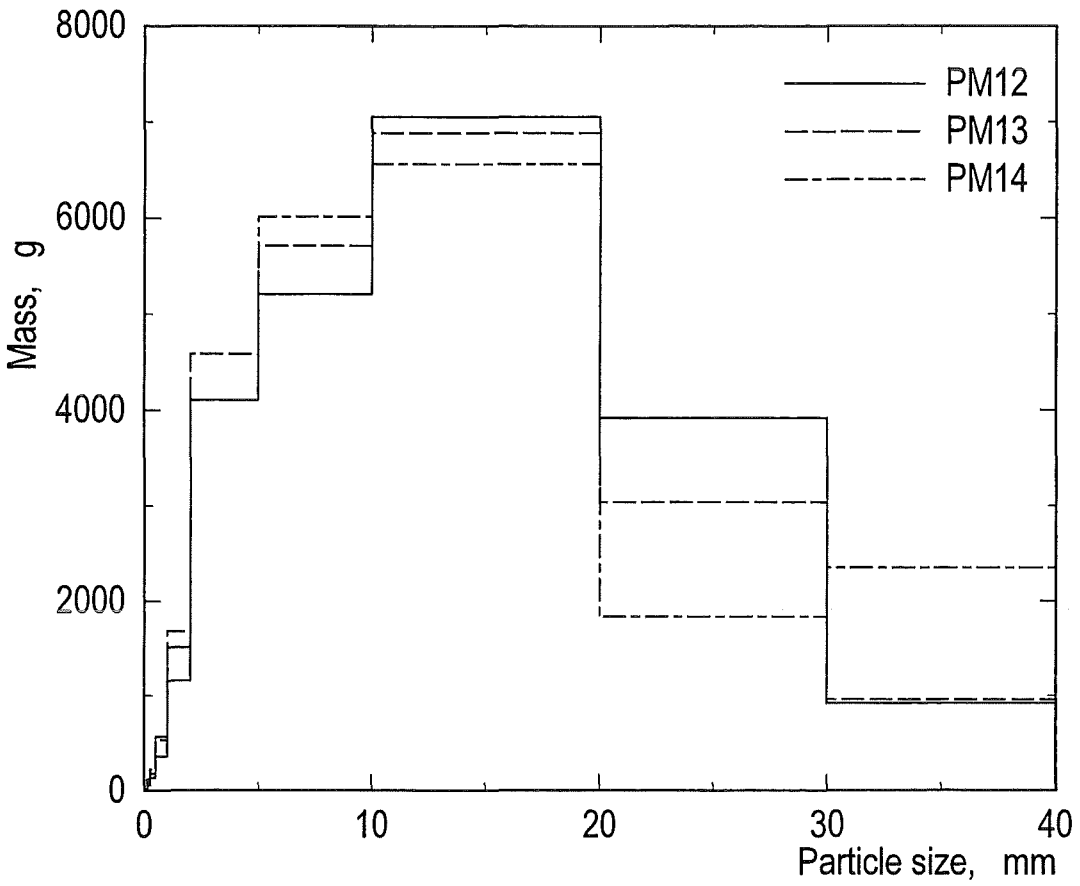

Fig. 6.9 Post-test particle size distribution of the melt fragments

7 SUMMARY AND CONCLUSIONS

Three experiments have been performed with similar starting conditions to prove the reproducibility of the PREMIX test series. The test conditions were also chosen to facilitate the comparison with results of the FARO/FAT tests performed with molten corium and water at JRC Ispra. The important results are briefly summarized:

- The general course of the three tests was rather similar. Fragmentation of the melt and steam production occurred in such a way that the bulk of water was prevented from close contact with the melt. Evidence of this condition is given by the average steam fraction inside the interaction zone which took on values around 50 ±10 % (and more) after a few to several tenths of seconds. No indication of conditions was found under which a steam explosion can be expected.
- The most relevant measurements, pressure and steam generation, show similar rates of increase, the maxima differ by less than 10 %.
- Peculiar differences were observed in the pressure evolution after the first melt/water contact when a significant pressure rise started. The pressure evolution strongly depended on the mode of melt release, particularly on the initial speed of melt.
- The melt fragments found after the test compare well as regards the size distribution. Only in one case (PM12) the melt mass released was larger than intended.

The deviations found in the test results can generally be attributed to uncertainties in preparing and controlling the melt supply as well as to fortuity occurring during the starting procedure. E.g., the gas valve actuation, which included preset delay times, was mainly triggered by switches in the melt detector signals. The times of those triggers depended on the speed of thermite reaction. Moreover, the initial jet formation was influenced by the mode of membrane melt-through.

The large melt mass released in PM12 (29 kg compared to 23.2 and 23.8 kg in the other tests), is ascribed to uncertainties in the test preparation. We believe, on basis of data examination, that the course of events in this test was concerned by the surplus melt mass only in the later period of time.

The peculiar difference in the results, i.e. the delay in time between the first contact of melt with water and the start of marked pressure increase in the interaction zone, was found to be due to the height of the GP12 driving pressure established at the time when melt release started. The actual GP12 pressure was, in turn, determined by the conditions given by the time history of gas valve operation. The different driving pressures resulted in different speeds of melt release.

Despite of the differences outlined which (1) were found to be in an acceptable range, (2) can be assigned to the respective conditions at the start of melt release, one can summarize that the results are conclusive. We conclude from this that the PREMIX experiments are reproducible.

The measurements provide a data base that can be used for the validation of multiphase computer codes (MC3D, MATTINA, IVA).

8 LITERATURE

/1/ D. Magallon, G. Berthoud, W. Schütz, N. Kolev, A. Alemberti, R. Seghal, M. Bürger, G. Colombo, B. Turland, S. Zero, Characterisation of processes which govern quenching of molten corium in water including steam explosions, FISA 97– EU Research on Severe Accidents: Mid-Term Review Symp. on Shared-Cost and Concerted Actions in Reactor Safety, Luxembourg, November 17-19, 1997, Luxembourg: Office for Official Publ. of the European Communties, 1998, S. 93-102

/2/ F. Huber, A. Kaiser, M. Steinbrück, H. Will, PREMIX - Documentation of the results of experiments PM01 to PM06, FZKA 5756, March 1996

/3/ W. Schütz, F. Huber, A. Kaiser, H. Will, PREMIX, an experimental approach to investigate the mixing behaviour of a hot melt being poured into water, Proc. of the Internat. Topical Meeting on Advanced Reactors Safety, Orlando, June 1-5, 1997 Vol. 2, S. 887-94, La Grange Park, I11.: American Nuclear Soc., 1997

/4/ A. Kaiser, W. Schütz, H. Will, Melt Water Interaction Tests (PREMIX Tests PM10 and PM11), Proc. of the OECD/CSNI Specialist Meeting on Fuel-Coolant Interactions (FCI), Tokai-Mura, Japan, May 19-21, 1997, JAERI-Conf. 97-011 (Part II) (January 98), S. 646-57

Acknowledgement

The authors thank all colleagues who helped performing the experiments and evaluating the data and who made precalculations.

This work has been performed in the framework of "Projekt Nucleare Sicherheit" of the Forschungszentrum Karlsruhe GmbH". It is partly funded by the European Community (under contract FI4S-CT96-0037), SIEMENS, and a consortium of German electricity utilities.

Miscellaneous:

Tapes of video and high-speed camera recordings are available on request. Additionally, the event sequences obtained by video recording given in the report can be provided as AVI files on a CD or transmitted by e-mail.

Appendix A

Calculation of the melt release rate using pressure measurements

The one-dimensional numerical model is based on the following momentum equation that describes the flow of melt in a pipe:

$$dv=dt/h* (g*h - 0.5*(v+0.5*dv)*(v+0.5*dv)*zk + dp(t)/rho), \quad (A1)$$

or, in the difference form,

$$\Delta v=\Delta t/h*(g*h - 0.5*(v+0.5*\Delta v)*(v+0.5*\Delta v)*zk + dp(t)/rho), \quad (A2)$$

where

v and Δv	are the velocity and the change in velocity, respectively,
t and Δt	are the time variable and the time step (=0.001 s), respectively,
g and h	are the gravity constant and the actual geodetic height of the melt,
dp	is the time history of the pressure difference acting on the melt,
rho	is the density, and
zk	is a composed friction number: $zk = 1+\varsigma+\lambda*l_{noz}/d_{noz}$.

In the discretization (Fig. A1), the lower end of the nozzle tube is taken as the origin of the axial coordinate. The difference of the pressures measured inside and outside of the melt generator, GP12 and PK10, are taken as input. The most significant output data are the melt mass flow rate and the duration of melt release.

In the calculation, constant loss coefficients, constant flow cross section, constant viscosity and temperature, and homogeneous flow of melt are assumed. The density ($2800\ kg/m^3$) was set to 80% of the theoretical density attributed to the fragment material found after the test. As for the flow cross section, a small average crust thickness of 1.5 millimeters is considered that reduces the nozzle internal diameter. The loss coefficients were chosen to be $\varsigma=0.6$ at the entrance to nozzle tube and $\lambda=0.22$ within the tube.

Beräknat 2790

The loss coefficients (which are in fact somewhat larger than those generally used for single-phase flow in a smooth pipe) together with the density and the reduced nozzle diameter resulted in melt release times that agree with those derived from the pressure readings. It should be noted that corresponding sets of parameters gave good results also for other PREMIX melt generator designs.

The calculation is started at the time when the steel membrane in the nozzle melts. The initial height of the melt in the crucible is calculated from the total mass of fragments found after the test. The flow of melt starts from the state of rest.

The fraction of melt mass that passes the initial location of the membrane during Δt is given by

$$\Delta me(t_i) = 0.5*(v_{i-1} + v_i) * \Delta t*rho*A_{noz}\,, \qquad (A3)$$

where A_{noz} is the nozzle cross section. The mass fractions are integrated to give the total mass:

$$me(t_i) = me(t_{i-1}) + \Delta me(t_i). \qquad (A4)$$

The melt surface is considered to move evenly at any time. The funnel cross section is given as a function of the axial coordinate. The calculation is stopped when the mass ejected is equal to the initial melt mass, m0.

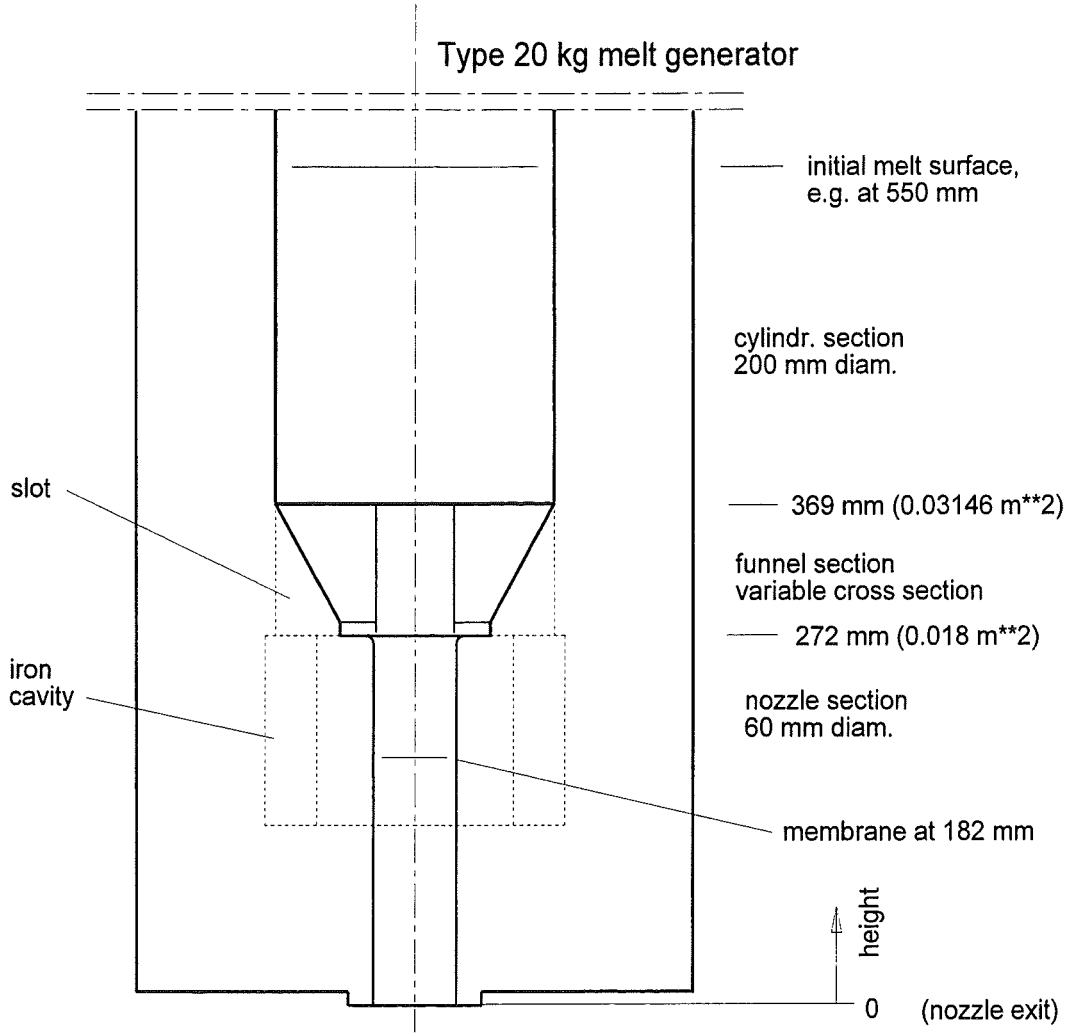

Fig. A1 Internal dimensions of the melt generator used in the PM12 – PM14 PREMIX tests, schematically.

APPENDIX B

Estimation of the volumes and masses involved in the thermal interaction

The volume of the interaction zone can be regarded as composed of three partial volumes:

$$V_I = V_{\ell,I} + V_{v,I} + V_{m,I}\,. \tag{B1}$$

The partial volumes refer, in the above sequence, to liquid, vapour (i.e. more common expression for steam), and melt. The volume of the interaction zone, V_I, can be obtained from the measurements. The $V_{v,I}$ and $V_{m,I}$ partial volumes can be estimated from the measurements and thereby the $V_{\ell,I}$ partial volume of the liquid. This is described in the following.

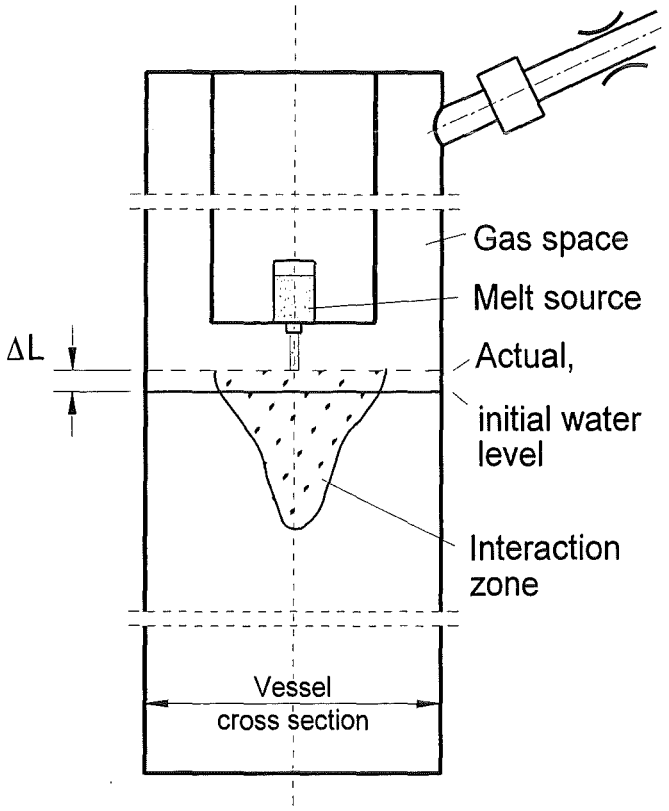

Fig. B1 Conditions around the interaction zone, schematically.

The *partial volume of the vapour,* $V_{v,I}$, is calculated from a mass balance considering the masses involved in the interaction. The control room of the balance comprises the pool water volume, the melt provided by the melt generator, and the steam within the gas space. This space covers the whole gaseous compartment above the initial water surface up to the location of the flow meters. The sum of the masses prior to the test is:

$$\sum m = m_\ell^0 + m_{v,G}^0 + m_m\,, \tag{B2}$$

where the superscript 0 means the condition for t=0. Application of the relation $m = V \cdot \rho$ to eq. (B1) results in

$$\sum m = V_\ell^0 \cdot \rho_\ell + V_{v,G}^0 \cdot \rho_v + V_m \cdot \rho_m\,. \tag{B2a}$$

For times t > 0, part of the water evaporates. Both the masses of the liquid and the steam become functions of time and the mass balance provides the relation:

$$\sum m = m_\ell + m_{\ell,I} + m_{v,I} + m_{v,G} + m_{v,exit} + m_m \qquad \text{(B3)}$$

The meaning of the summands is:

- m_ℓ is the mass of the water outside of the interaction zone;
- $m_{\ell,I}$ and $m_{v,I}$ are the masses of the water and the steam, respectively, inside the interaction zone;
- $m_{v,G}$ is the mass of steam in the gas space. It diminishes with time due to the growth of the interaction zone;
- $m_{v,exit}$ is the integrated steam mass whose volume flow rate is measured at the venting tubes.

The volume of m_ℓ in eq. (B3) is calculated as initial water volume plus water level increase times vessel cross section minus interaction volume (compare Fig. B1):

$$V_{\ell,pool} = V_\ell^0 + \Delta L \cdot A_V - V_I . \qquad \text{(B4)}$$

Introducing densities in eq. (B3) and considering eq. (B4) one obtains:

$$\sum m = (V_\ell^0 + \Delta L \cdot A_V - V_I)\cdot \rho_\ell + V_{\ell,I}\cdot \rho_\ell + V_{v,I}\cdot \rho_v + V_{v,G}\cdot \overline{\rho}_v + V_{v,exit}\cdot \rho_v + V_m \cdot \rho_m \qquad \text{(B3a)}$$

Eqs. (B2a) and (B3a) are equated while also considering eq. (B1) and taking into account that $\rho_v / \rho_\ell << 1$. One obtains, after a few conversions, an equation for the partial volume of the vapour:

$$V_{v,I} = \Delta L \cdot A_V - V_{m,I} + V_{v,exit}\cdot \frac{\rho_v}{\rho_\ell} + \left[V_{v,G}\cdot \frac{\overline{\rho}_v}{\rho_\ell} - V_{v,G}^0 \cdot \frac{\rho_v}{\rho_\ell} \right] \qquad \text{(B5)}$$

The two terms summarized in brackets constitute the change in steam volume in the gas room. The difference is very small and, therefore, eq. (B5) is reduced to the following equation:

$$V_{v,I} = \Delta L \cdot A_V - V_{m,I} + V_{v,exit}\cdot \rho_v / \rho_\ell , \qquad \text{(B5a)}$$

The (total) melt volume, V_m, disappears during the above conversions. Instead, the *partial volume of the melt*, $V_{m,I}$, comes into consideration in eq. (B5a). Since the melt flow rate can not be measured in the experiments, the melt volume flow entering the interaction zone is estimated on basis of the flow rate predicted by a simple numeri-

cal model (see section 2.6.2). In an approximation, the calculated mass flow function was shifted in time to account for the travelling time of the melt front through the initial falling height to the water level. The shifted function is drawn in Fig. B2.

Using the melt flow function, the $V_{v,l}$ partial volume of the vapour could now be calculated from eq. (B5a) and thereby also the $V_{\ell,l}$ partial volume of the liquid water from eq. (B1). The three essential functions that determine the calculation are shown in Fig. B3 in a larger time scale.

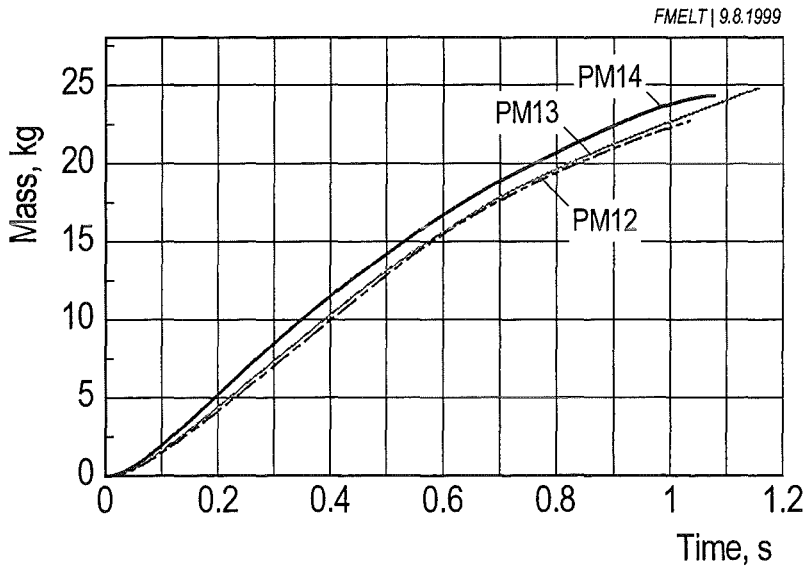

Fig. B2 Integrated functions of the volume flow rate. entering the interaction zone.

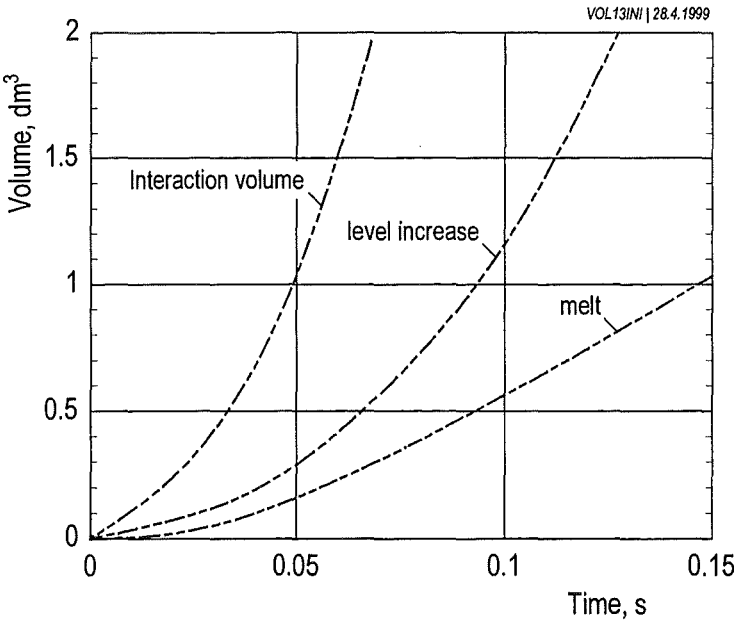

Fig. B3 The three major functions that determine the calculation of the volume fractions shown in a larger time scale (here: PM13).